Technische Universität München
TUM School of Natural Sciences

Vortex Matter Transport Phenomena of the Intertype Superconductor Niobium

Xaver Simon Brems

Vollständiger Abdruck der von der TUM School of Natural Sciences der Technischen Universität München zur Erlangung eines

Doktors der Naturwissenschaften (Dr. rer. nat.)

genehmigten Dissertation.

Vorsitz: Prof. Dr. Michael Knap

Prüfende der Dissertation:

1. Priv.-Doz. Dr. Sebastian Mühlbauer
2. Prof. Dr. Winfried Petry

Die Dissertation wurde am 05.11.2024 bei der Technischen Universität München eingereicht und durch die TUM School of Natural Sciences am 03.12.2024 angenommen.

Abstract

Superconductors are materials that, below a critical temperature and critical field, exhibit zero electrical resistance and perfect diamagnetism, meaning they expel magnetic fields through the Meissner effect. For fields above the critical field, superconductivity either breaks down, which is true for type-I superconductors, or, in the case of type-II superconductors, the material enters a new phase, called mixed state. In the mixed state, superconductivity persists, but the magnetic field enters the material in quantized units, called flux lines or vortices. These flux lines are topological entities each carrying a magnetic flux quantum given as $\Phi_0 = h/2e$, which is screened by circulating supercurrents. Superconducting vortices are found in a plethora of different vortex matter states, but the regular vortex lattice (VL) is the most well known.

The elemental superconductor niobium (Nb) exhibits an unusual vortex matter state called the intermediate mixed state (IMS). In the IMS flux-free Meissner state domains are interspersed with mixed state domains filled with a regular VL. This vortex matter state is found in materials on the verge between the standard type-I/type-II classification and are often referred to as intertype superconductors. In contrast to the fully repulsive vortex interactions of type-II superconductors, intertype superconductors exhibit a non-monotonous vortex interaction resulting in the vortex clustering and the formation of the IMS in Nb. In previous works, the IMS was studied as a function of field and temperature, but so far little attention has been given to the influence of a transport current on the IMS domain structure.

Here, a systematic study of the influence of a transport current on the IMS domain structure is presented building on recent results of a current-induced pattern formation in the IMS. Using a combination of lab-based characterization tools and small-angle neutron scattering (SANS) we study the vortex matter in the intertype superconductor Nb as a function of magnetic field, temperature and current. This work has three major contributions. (i) A modified Porod analysis was developed to extend the accessible length scales of a standard SANS setup from 1 μm up to 40 μm in the case of long extended structures aligned along the beam direction. This allowed the tracking of the micrometer-sized domain repetition length over the entire field range of the IMS and extract the field-dependence of the mixed state domain size. (ii) A custom-built AC susceptibility and transport measurement system was implemented into a SANS cryomagnet allowing for an *in-situ* characterization during neutron experiments. The system was used to study the magnetic and electronic properties of the superconducting vortex matter. The field-dependence of the critical depinning current for vortex movement showed a subtle change in behavior at the field value extracted from SANS marking the transition to the IMS. This subtle feature could act as a new macroscopic signal to the detect the IMS in unknown samples. The combined analysis of the field-dependence of the mixed state domain size extracted from SANS and the critical depinning current suggests, that inside the IMS, the field dependence of vortex depinning is solely governed by the size of the mixed state domains. (iii) Finally, *in-situ* transport and SANS measurements confirmed the current-induced rearrangement to a stripe structure over a wide field range within the IMS. Furthermore, the current-induced changes in the SANS pattern indicates that the rearrangement occurred at currents well below the critical depinning current extracted from transport measurements. No such precursor were observed in the standard mixed

state pointing to a rearrangement mechanism closely linked to the intricate physics of the IMS.

Overall, our study underlines that the IMS represents a remarkable realization of a pattern-forming model system that can be tuned via temperature, field, and, as highlighted by this work, a transport current. Furthermore, the IMS under the influence of a transport current could act as a model system to study non-equilibrium phase transitions, where especially the influence of the non-monotonous vortex interaction remains unexplored.

Kurzzusammenfassung

Supraleiter sind Materialien, die unterhalb einer kritischen Temperatur und einem kritischen Magnetfeld keinen elektrischen Widerstand und perfekten Diamagnetismus zeigen, was bedeutet, dass sie Magnetfelder durch den Meissner-Effekt verdrängen. Bei Magnetfeldern oberhalb des kritischen Wertes bricht die Supraleitung entweder zusammen, wie dies bei Typ-I Supraleitern der Fall ist, oder, im Falle von Typ-II Supraleitern, wird ein neuer Zustand, der sogenannte Mischzustand, erreicht. Im Mischzustand bleibt die Supraleitung erhalten, jedoch dringt das Magnetfeld in quantisierten Einheiten, sogenannten Flusslinien oder Vortices, in das Material ein. Diese Flusslinien sind topologische Strukturen, die jede ein magnetisches Flussquantum $\Phi_0 = h/2e$ tragen, welches durch umlaufende Suprastrőme abgeschirmt wird. Supraleitende Vortices sind in einer Vielzahl an unterschiedlichen Zuständen (Vortex-Materie) zu finden, wobei das reguläre Vortex oder Flussliniengitter am bekanntesten ist.

Der Elementarsupraleiter Niob (Nb) zeigt einen ungewöhnlichen Vortex-Matter Zustand, der als gemischter Zwischenzustand (IMS) bezeichnet wird. Im IMS sind flussfreie Meissner-Domänen mit Domänen im Mischzustand, die ein regelmäßiges Vortex Gitter enthalten, durchsetzt. Dieser Vortex-Matter Zustand tritt in Materialien auf, die sich an der Grenze zwischen der Standardklassifikation der Typ-I/Typ-II-Supraleiter befinden, und wird häufig als Intertyp-Supraleiter bezeichnet. Im Gegensatz zu den vollständig abstoßenden Vortex Wechselwirkungen bei Typ-II-Supraleitern besitzen Intertyp-Supraleiter eine nicht-monotone Vortex Wechselwirkung, die zur Bildung von Vortex-Bündeln und zur Entstehung des IMS in Nb führt. In früheren Arbeiten wurde der IMS als Funktion von Feld und Temperatur untersucht, jedoch wurde bisher wenig Aufmerksamkeit auf den Einfluss eines Transportstroms auf die IMS-Domänenstruktur gelegt.

In dieser Arbeit wird eine systematische Studie des Einflusses eines Transportstroms auf die IMS-Domänenstruktur vorgestellt, die auf aktuellen Ergebnissen einer strominduzierten Musterbildung im IMS basiert. Mit einer Kombination aus laborgestützten Charakterisierungsmethoden und Kleinwinkelneutronenstreuung (SANS) untersuchen wir die Vortex-Materie im Intertyp-Supraleiter Nb als Funktion des Magnetfelds, der Temperatur und des Stroms. Diese Arbeit umfasst drei wesentliche Beiträge: (i) Eine modifizierte Porod-Analyse wurde entwickelt, um die zugänglichen Längenskalen eines Standard-SANS-Setups von 1 μm auf bis zu 40 μm im Falle langgestreckter Strukturen entlang der Strahlrichtung zu erweitern. Dadurch wurde das Verfolgen der Wiederholungslänge der IMS-Domänenstruktur im Mikrometerbereich über den gesamten IMS-Feldbereich ermöglicht. Zudem konnte die Feldabhängigkeit der Mischzustands-Domänen extrahiert werden. (ii) Ein maßgefertigtes AC-Suszeptibilitäts- und Transportsystem wurde in einen SANS-Kryomagneten integriert, um eine *in-situ*-Charakterisierung während Neutronenexperimenten zu ermöglichen. Dieses System wurde genutzt, um die magnetischen und elektronischen Eigenschaften der supraleitenden Vortex-Materie zu untersuchen. In der Nähe des Feldwerts, der den Übergang zum IMS markiert und mit SANS extrahiert wurde, zeigte die Feldabhängigkeit des kritischen Vortex-depinning-Stroms einen leichten Knick. Dieses Merkmal könnte als neues makroskopisches Signal zur Erkennung des IMS in unbekannten Proben dienen. Die kombinierte Analyse der Feldabhängigkeit der Mischzustands-Domänen des IMS aus SANS und des kritischen Vortex-depinning-Stroms deutet darauf hin, dass innerhalb des IMS die Feldabhängigkeit des Vortex-depinning-

Stroms ausschließlich durch die Geometrie der Mischzustands-Domänen bestimmt wird. (iii) Die *in-situ* Transport- und SANS-Messungen bestätigten die strominduzierte Umordnung zu einer Streifenstruktur über einen weiten Feldbereich innerhalb des IMS. Darüber hinaus deuten die strominduzierten Veränderungen im SANS-Muster darauf hin, dass die Umordnung bei Strömen weit unterhalb des kritischen Vortex-depinning-Stroms, der aus Transportmessungen extrahiert wurde, auftrat. Solche Vorläufer wurden im homogenen Mischzustand nicht beobachtet, was auf einen Umordnungsmechanismus hinweist, der eng mit der komplexen Physik des IMS verknüpft ist.

Insgesamt unterstreicht unsere Studie, dass der IMS ein bemerkenswertes Modellsystem für Musterbildung darstellt, das von Temperatur, Feld und, wie durch diese Arbeit hervorgehoben, einen Transportstrom bestimmt ist. Darüber hinaus könnte der IMS unter Einfluss eines Transportstroms als Modellsystem dienen, um Nichtgleichgewichts-Phasenübergänge zu untersuchen, bei denen insbesondere der Einfluss der nicht-monotonen Vortex Wechselwirkung noch unerforscht ist.

Contents

1 Introduction

Superconductivity, first discovered by Heike Kamerlingh Onnes in 1911 [1], is one of the most fascinating phenomena in condensed matter physics. Superconductors are materials that, below a critical temperature, exhibit zero electrical resistance and perfect diamagnetism, meaning they expel magnetic fields through the Meissner effect [2]. These remarkable properties make superconductors promising candidates for a range of technological applications, including energy-efficient power transmission, high-field magnets, and quantum computing. The theoretical understanding of superconductivity has evolved significantly over the decades, with major milestones including the Bardeen-Cooper-Schrieffer (BCS) theory [3], which explains the formation of Cooper pairs as the basis of superconducting behavior, and the Ginzburg-Landau theory [4], which provides a macroscopic description of superconductivity in terms of an order parameter. More recently, advances in understanding unconventional superconductors, such as high-temperature cuprates [5, 6], iron-based superconductors [7], and topological superconductors [8], have opened new avenues in condensed matter research, highlighting the diverse mechanisms through which superconductivity can emerge and broadening the potential applications of these materials. In most superconductors, the perfect diamagnetism of the Meissner state is only maintained up to a critical field. For higher values, the superconductor transitions into the mixed state, where the magnetic field penetrates the material in quantized units called flux lines. The magnetic field inside the flux lines is screened by circulating supercurrents, which is why they are named vortices. Depending on the mutual interaction between vor-

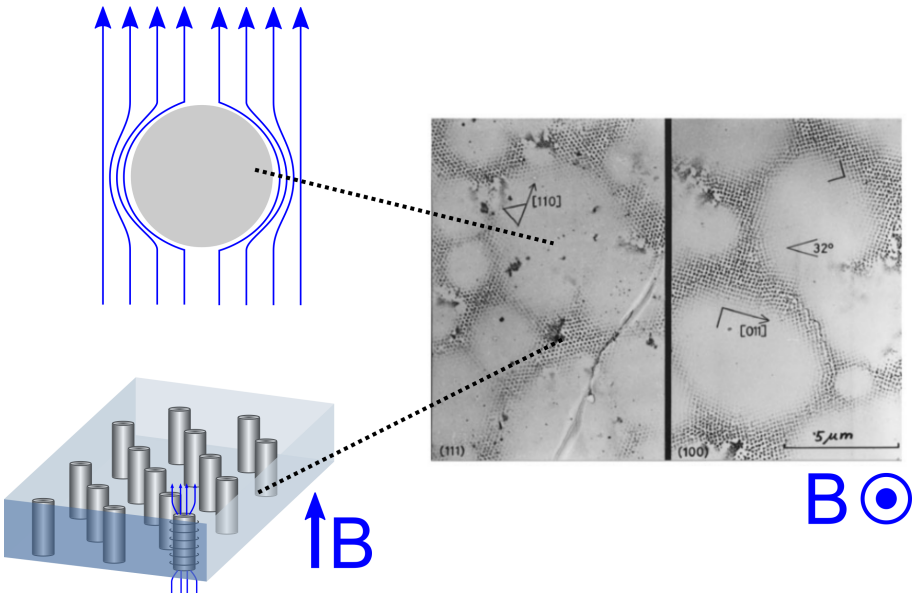

Figure 1.1: Schematic representation of the Meissner effect, the regular VL, and a Bitter decoration image of the intermediate mixed state in niobium. In the Bitter decoration image, ferromagnetic particles are evaporated on top of the superconducting sample and position themselves on top of the vortices. Each black dot is a vortex and marks the VL within the mixed state domains. The Meissner state domains, being free of flux, appear in light grey. The Bitter decoration image is reprinted with permission from [9]. Copyright (2011) Springer Nature.

tices and the influence of the superconducting material, vortices are found in a plethora of different vortex matter states ranging from a homogeneous vortex lattice (VL) to liquid behavior [10] (see section 2).

The intermediate mixed state (IMS), which is the main concern of this work, is a special vortex matter state. In the IMS, due to a rare, partially attractive vortex interaction, vortices are clustered together. As a result, mixed state domains filled with a regular VL are interspersed with flux-free Meissner state domains as observed in Bitter decoration images of niobium samples (see 1.1) While known for several decades, the IMS and vortex clustering in superconductors is still not understood and an ongoing research field [11, 12, 13, 14, 15, 16]. Especially the influence of a transport current on the IMS has not received much attention so far and is the main concern of this work.

Moving vortices: resistance is useless

A transport current applied to a vortex-carrying superconductor can lead to a depinning of vortices due to the current-induced Lorentz force. Moving vortices lead to a buildup of a voltage in the direction parallel to the applied current and, hence, the destruction of the zero-resistance state, rendering the superconductor useless for most technological applications. To recover the perfect conducting properties, the movement of vortices has to be prevented. In the canonical mixed state, where the vortices are commonly arranged in a homogeneous VL, this is a well-studied phenomenon [10]. In the IMS, the scenario is more intricate as the two-phase domain structure leads to an additional constraint for the transport current. According to Ampere's law, a current can only exist in areas with a non-vanishing curl of the magnetic field. As the IMS consists of mixed state domains and flux-free Meissner state domains (B=0), this means that a transport current in the IMS is constrained to the mixed state domains, the domain interfaces, and the sample's surfaces. As a result, the current distribution is highly heterogeneous over the sample. In this scenario, a bulk current is only expected to exist if the mixed state domains are percolating. Given this preliminary condition, the resulting highly heterogeneous current path induces a non-uniform Lorentz force and is expected to lead to a complex rearrangement process of the IMS domain structure.

Up until recently [17], the IMS as a function of current remained experimentally unexplored. Combined neutron scattering and transport measurements revealed that the IMS persists in the state of flux flow. The defining characteristic of the IMS – a field-independent mean intervortex distance – remained intact even when an external transport current was applied. Additionally, the vortex clusters elongated perpendicular to the direction of the applied current, forming a stable steady state. The external transport current eliminated the hysteretic behavior observed following different experimental measurement procedures. Complementary numerical simulations agreed well with the experimental results and provided a detailed picture of the rearrangement process that is closely linked to the intricate physics of the IMS. While our previous work represented a significant advancement in the study of the IMS under current, many questions, like the field dependence of the rearrangement mechanism and the field dependence of the IV characteristics of the IMS, remained unexplored.

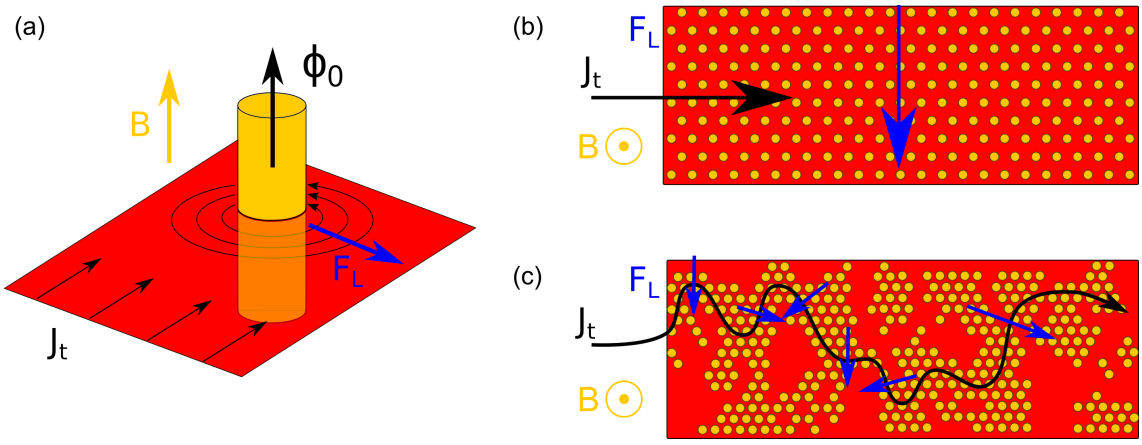

Figure 1.2: Schematic drawing of vortex depinning of the mixed state and the IMS. (a) A single vortex of flux Φ_0 interacts with the transport current I and can be depinned due to the Lorentz force F_L. (b) In the homogeneous mixed state, the Lorentz force acts homogeneously over the entire sample. (c) In the IMS, the domain structure constrains the current path and leads to a highly heterogeneous Lorentz force that can vary in strength and direction. Reproduced from [18].

Outline of this thesis

This work continues to investigate the properties of the intertype superconductor Nb as a function of applied magnetic field, temperature, and current using small-angle neutron scattering (SANS) in combination with laboratory-based characterization techniques. In the following, we present and summarize the main results of this work before we give an outline of this thesis.

As one of the main results we find that due to the highly aligned nature of the IMS domains along the field, a modified Porod analysis can be employed to extend the range of SANS from 1 micrometer up to 40 micrometers. This allows the tracking of the field dependence of the mixed state and Meissner state domain size over the entire field range of the IMS. In principle, the modified Porod analysis can be generalized to other systems with similar morphology. The IV-characteristics from lab-based characterization measurements of the IMS revealed a field dependence of the critical depinning current that shows a subtle change in the vicinity to the field B^* extracted from SANS, marking the transition to the IMS. A combined analysis of the field dependence of the mixed state domains from SANS and the field dependence of the critical depinning current suggests that inside the IMS the critical depinning current is governed by the spatial distribution of the domain structure. Finally, *in-situ* transport SANS measurements show that the IMS robustly rearranges over a wide range of fields into a stripe structure oriented parallel to the movement of vortices. The detailed analysis of combined transport and SANS measurements reveals that this rearrangement occurs for currents well below a finite flux flow voltage. This extends our previous results and points to an interesting reordering mechanism inside the IMS that is closely linked to the interplay of the pinning landscape with the domain structure governed by the intricate physics of the IMS.

This thesis is organized in the following way: In chapter 2, we give an overview of superconductivity and magnetic flux structures encountered in superconductors. We review the

major classes of superconducting materials before we shed light on the different magnetic behaviors of superconductors, with a focus on exotic vortex matter explained within the extended Ginzburg-Landau formalism and current-induced vortex matter states. Chapter 3 provides the reader with the basic working principles of the experimental methods employed within this thesis. We first deal with the lab-based characterization tools and their theoretical foundations for the study of the magnetic and electronic properties of superconductors. More specifically, magnetic susceptibility, transport measurements, and pinning theory are covered. We then focus on neutron scattering methods with a focus on scattering from large-scale magnetic structures within the IMS. We first review the basics of scattering methods before turning our attention to the experimental study of vortex matter within the IMS and the experimental setup of a small-angle neutron scattering instrument. The chapter concludes with an overview of the different samples used within this thesis. The following three chapters concern the experimental results of this thesis. Each of the chapters is organized in sections containing a detailed description of the experimental setup, the experimental results, the discussion, and a summary of the results. Chapter 4 and chapter 6 dealing with neutron scattering also contain a detailed section about the data analysis after summarizing the experimental setup. Chapter 4 presents our results from SANS studying the field dependence of the VL morphology and the IMS domain structure using the modified Porod analysis. Chapter 5 explores the magnetic and electronic properties of the IMS in Nb in temperature and current scans as a function of the field. Chapter 6 highlights the power of our combined transport measurement and SANS setup to study the current-induced rearrangement of vortex matter in the intertype superconductor Nb. Finally, we recap the results of this thesis in chapter 7, where we also shed light on future perspectives in the study of complex ordering phenomena, vortex fluid dynamics, and non-equilibrium phase transitions using superconducting vortex matter as a model system.

2 Superconductivity and Magnetic Flux Structures

This chapter provides the reader with the theoretical background on superconductivity and magnetic flux structures in superconductors. In section 2.1, we briefly overview the most influential superconducting material classes and their characteristics. In section 2.2, we focus on the magnetic behavior and plethora of different magnetic flux structures observed in superconductors covering the basic classification within the Ginzburg-Landau theory (section 2.2.1), before turning our attention to different vortex matter state (section 2.2.2) and vortex clustering and the intermediate mixed state (section 2.2.3). We conclude this chapter in section 2.3 dealing with the interaction of transport currents with vortices and summarizing the main results of previous vortex matter studies under the influence of a transport current.

2.1 Superconducting Material Classes

BCS superconductors are named after the Bardeen-Cooper-Schrieffer theory, formulated in 1957 by John Bardeen, Leon Cooper, and Robert Schrieffer [3]. This theory explains superconductivity in terms of Cooper pairs, where two electrons – typically fermions that repel each other – pair up through an indirect attraction mediated by the lattice vibrations, called phonons. The importance of phonons was first evidenced by the discovery of the isotope effect, showing that the transition temperatures in different isotopes of the same element are inversely proportional to the average mass number of the isotopes [19, 20]. The phonon-mediated electron pairing creates a state where resistance vanishes completely. The cooper pairs move coherently through the material without being scattered by impurities or defects, which eliminates electrical resistance. The BCS theory predicts low critical temperatures, generally below 30 K, making these materials traditional low-temperature superconductors. Lead, tin, and niobium are typical examples of BCS superconductors, and they are often used in applications such as superconducting magnets and superconducting radiofrequency cavities for particle accelerators.

High-temperature superconductors (HTS), first discovered by J.G. Bednorz and K.A. Müller in the mid-1980s [5], represented a revolutionary breakthrough in superconductivity. The discovery of superconductivity at temperatures above the boiling point of liquid nitrogen (77 K) challenged previous assumptions and opened the door to more practical and accessible applications [6, 21]. HTS materials have layered structures composed of copper-oxide planes, known as cuprates. Superconductivity is induced via carrier doping (electron or hole) of the antiferromagnetic insulating parent material [7]. Due to the anisotropic layered structure of HTS, the superconducting properties are also highly anisotropic, leading to an anisotropic VL if the field is applied at an angle θ from the c-axis [22]. The mechanism of superconductivity in HTS remains only partially understood, as the BCS theory fails to fully explain their behavior. Instead of a phonon-mediated mechanism behind the electron pairing, it is assumed that in these materials, the rich electronic and magnetic properties of the undoped parent material play a critical role in the glue that forms the cooper pairs. The most well-known HTS materials are Yttrium

Barium Copper Oxide (YBCO) and Bismuth Strontium Calcium Copper Oxide (BSCCO). Cuprates exhibit superconductivity at temperatures well above 77 K, making them highly desirable for energy transmission lines and magnet applications requiring minimal cooling.

Iron-based superconductors are a more recent discovery identified in 2006 [23]. They represent a novel category of superconductors with a promising potential of high critical temperatures [24]. The presence of superconductivity in iron-based materials, typically considered a magnetic element, was met with surprise in the community, as magnetism usually competes with superconductivity. Similar to high-temperature superconductors, the pairing mechanism in iron-based superconductors is believed to involve spin fluctuations rather than conventional phonon coupling [7]. These superconductors have a layered crystal structure, with iron and arsenic or iron and chalcogen atoms forming key components of their unit cells. The interplay between magnetism and superconductivity is a defining feature of these materials, and understanding this balance is a major area of current research. Examples of iron-based superconductors include Lanthanum Iron Arsenide (LaFeAsO) and Iron Selenide (FeSe). These materials can exhibit superconductivity at temperatures as high as 50 K, making them significant for understanding unconventional superconducting mechanisms.

Heavy fermion superconductors are a unique class of materials that exhibit unconventional superconductivity at very low temperatures, often below 1 K [25]. These materials are characterized by f-electron elements such as cerium, uranium, or ytterbium, which lead to strong electronic correlations. In heavy fermion superconductors, the effective electron masses are much larger than those in conventional metals, giving rise to the term *heavy fermion*. This phenomenon results from strong interactions between conduction electrons and localized magnetic moments. The superconductivity in these materials often involves magnetic fluctuations, which provide an alternative pairing mechanism distinct from phonon-mediated pairing. Notable examples include Cerium Copper Silicide ($CeCu_2Si_2$) [26, 27] and Uranium Platinum (UPt_3) [28, 29]. Studying these materials helps to understand the intricate relationship between magnetism and superconductivity, as both phenomena coexist within heavy fermion compounds.

Fullerene superconductors are a class of organic superconductors based on carbon molecules, such as C60, commonly known as buckyballs [30]. These superconductors are usually formed by doping C60 with alkali metals, which leads to the emergence of superconducting properties. In fullerene superconductors, the mechanism of superconductivity is believed to involve electron-phonon coupling. Alkali metal atoms, such as potassium or rubidium, donate electrons to the fullerene molecules, which leads to the formation of Cooper pairs. Fullerene superconductors exhibit moderate critical temperatures, typically in the range of 20-40 K. Potassium-doped C60 and Rubidium-doped C60 are common examples of fullerene superconductors. Their unique molecular structure and high symmetry have made them a topic of great interest for exploring how superconductivity can emerge in molecular systems.

High-pressure hydride superconductivity refers to the phenomenon where certain hydrogen-rich compounds, or hydrides, exhibit superconducting properties at relatively high temperatures when subjected to extreme pressures [31]. The high superconducting transition temperatures are linked to the electronic properties of hydrogen under extreme pressures.

In hydrides, the presence of other atoms induces a chemical pressure, significantly reducing the external pressures needed to induce strong atomic bonding and a dense electronic structure, allowing for superconductivity in hydrogen. The pairing mechanism in hydrides can be linked to the conventional phonon-mediated BCS cooper pairs. As BCS superconductivity is theoretically well understood, this allows us to directly compare experimental results with theoretical predictions, potentially leading to the realization of room-temperature superconductivity at ambient conditions [31]. The field gained prominence with the discovery that hydrogen sulfide could superconduct at temperatures as high as 203 K under pressures above 150 GPa [32]. Recent, unfortunately, fraudulent claims of ambient condition superconductivity in hydrogen hydrides[33, 34] led to increased attention to superconductivity in both the scientific community and the general population [35]. This increased attention and interest highlights the importance of scientific integrity and the potential influence an ambient condition superconductor could have on society.

Topological superconductors are among the most exotic classes of superconductors, distinguished by their topologically protected surface states [8]. These materials have nontrivial topological properties and give rise to Majorana fermions, quasiparticles that are their own antiparticles. This makes topological superconductors especially interesting for applications in quantum computing. Topological superconductors combine conventional superconductivity with topological order. They may be engineered by placing conventional superconductors in proximity to topological insulators or by doping materials with topological properties. The superconducting state in these materials supports Majorana zero modes at the edges or surfaces, which are predicted to be robust against local perturbations. Proximity-induced superconductivity in topological insulators such as Bismuth Selenide Bi2Se3 and Cu-doped Bi2Se3 are examples of topological superconductors. The prospect of fault-tolerant quantum computation renders them exciting topics in condensed matter physics today.

2.2 Magnetic Flux Structures in Superconductors

The vanishing electrical resistance for temperatures below the critical transition temperature T_c gives superconductors their name. However, their more fundamental property is connected to the magnetic response when placed in an external magnetic field. For low magnetic fields, superconductors are perfect diamagnets and expel an external magnetic field called the Meissner effect [2].

For increasing fields, in type-I superconductors, to which most elemental superconductors belong, the superconducting state breaks down after a certain threshold value, and the material transitions to the normal state. Type-II superconductors, which represent the majority of superconducting materials, allow for an additional state called the mixed state or Shubnikov state, where the magnetic field enters in the form of quantized flux lines. These long structures extended along the direction of the applied field usually exhibit a purely repulsive interaction. This often leads to the formation of a regular VL. For most cases, this binary approach based on the Ginzburg-Landau theory represents a useful categorization scheme for a wide temperature and field range. However, the flux structures in the IMS consisting of mixed state and Meissner state domains shown in the introduction in figure 1.1 are not compatible with the type-I/II dichotomy. In the following, we review

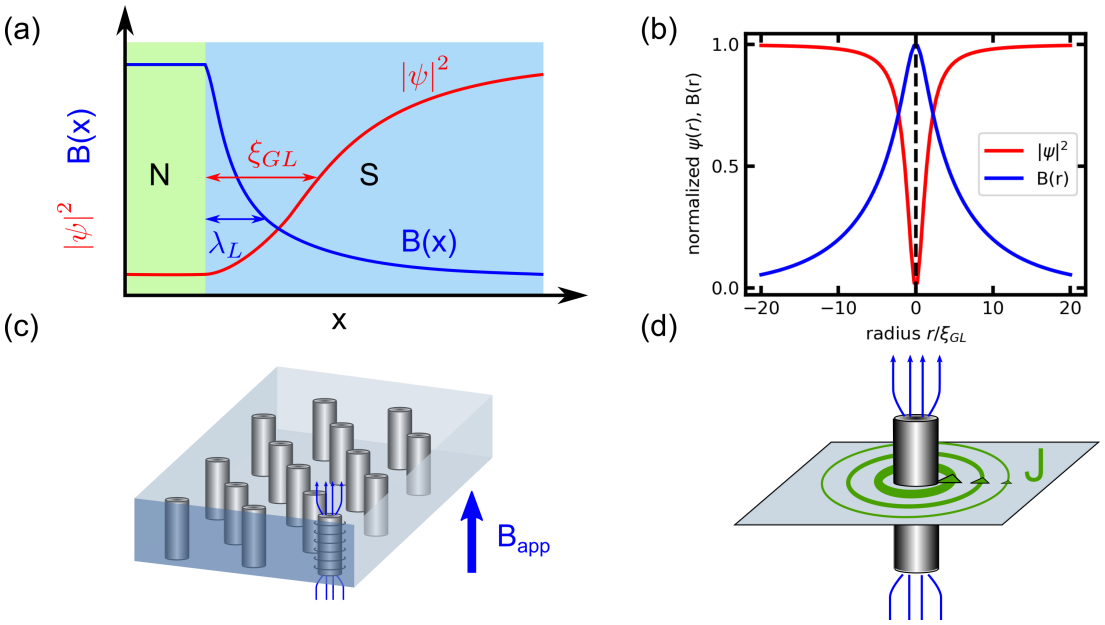

Figure 2.1: (a) Schematic depiction of a normal-superconducting interface. The magnetic field profile and the order parameter's absolute square are shown in blue and red, respectively. The London penetration depth λ_L and the GL coherence length ξ_{GL} are included in the same color code. (b) Cross-section of an isolated vortex's magnetic field and order parameter. (c) Schematic depiction of the VL. The screening currents and the direction of the magnetic flux are exemplary shown for a single vortex in the VL. (d) Schematic depiction of a single vortex, including the screening currents (green).

the basics of the categorization scheme within the Ginzburg-Landau theory and shed light on magnetic structures incompatible with the type-I/type-II dichotomy.

2.2.1 Ginzburg-Landau Theory

The distinction of superconductors into type-I or type-II superconductors within the Ginzburg-Landau theory is based on the energy contribution of a normalconducting-superconducting (NS) interface. The energy contribution of an NS interface is determined by the Ginzburg Landau parameter $\kappa = \frac{\lambda_L}{\xi_{GL}}$ given as the ratio of two length scales, the London penetration depth λ_L and the Ginzburg-Landau coherence length ξ_{GL}. These two length scales define an NS interface's magnetic and superconducting properties as schematically depicted in figure 2.1 (a).

λ_L describes the length scale on which the magnetic field B penetrates the superconductor. The penetration of B results in a gain in the energy of the superconductor due to the reduced magnetic field expulsion. Simultaneously, the NS interface leads to a loss in the condensation energy as the superconducting order parameter $|\psi|^2$ is suppressed on a length scale given by ξ_{GL}. The sum of these two contributions determines whether an NS interface leads to a net gain or net loss and, hence, whether vortices are stable or not.

Detailed calculations yield the separating point between type-I and type-II behavior as $\kappa_0 = \frac{1}{\sqrt{2}}$. For $\kappa < \kappa_0$, forming an NS interface causes a net loss and is hence avoided. An external magnetic field is completely screened and penetrates the sample only in a thin surface layer given by λ_L. For increasing field, this state called the Meissner state – also referred to as the Meissner-Ochsenfeld effect – persists until a certain threshold field at which the superconductor breaks down. Materials only exhibiting the Meissner state are referred to as type I.

Materials with $\kappa > \kappa_0$ allow for an additional phase called the mixed state. As for $\kappa > \kappa_0$ the NS interface energy is positive, the total interface between normalconducting and superconducting areas is maximized. Therefore, the superconducting state does not break down for fields $B > B_{c1}$, but B penetrates the material through quantized flux lines.

Flux lines represent topological defects of the superconducting condensate, each carrying a magnetic flux quantum of $\Phi_0 = h/2e$. Analogous to an NS interface, the size of the normal core of the flux line, where the $|\psi|^2$ is suppressed, can be characterized by ξ_{GL}, while the length scale over which the circulating superconducting currents screen the magnetic field is quantified by λ_L. Due to these screening currents, flux lines are also called superconducting vortices. The superconducting state persists up to a second critical field B_{c2}, after which the superconducting state also breaks down in type-II materials.

In the most common case, due to a purely repulsive vortex interaction, vortices arrange in a perfect lattice structure called the VL schematically depicted in figure 2.1 (c). However, superconducting vortices can arrange in many different configurations discussed in the following.

2.2.2 Vortex Matter in Superconductors

Similar to conventional matter, a multitude of different factors governs the spatial arrangement of vortices [37]: (i) the (purely) repulsive interaction between vortices favors the formation of a regular hexagonal lattice, (ii) interactions between vortices and the underlying crystal structure impose the crystal's anisotropy onto the VL, (iii) local defects create pinning sites that lead to disordered or glassy vortex configurations, (iv) thermal fluctuations can cause the VL to melt, (v) topological constraints related to the sample's shape can result in non-uniform vortex arrangements, and (vi) an external current exerts a Lorentz force on the vortices, which can lead to a depinning of vortices. [38]. The similarity of the observed vortex configurations to conventional matter coined the term vortex matter [37]. Studying the properties of the VL and vortex matter allows us to access the different factors influencing the spatial arrangement of vortices. However, assigning the underlying mechanism to the observed effect can be non-trivial [39].

Besides the canonical hexagonal VL mentioned above, one also observes scalene and rectangular VLs due to the influence of the symmetry of the superconducting pairing mechanism and the materials crystal structure on the symmetry of the VL [40, 14, 39]. The disorder introduced by, e.g., pinning sites can break the long-range order of the VL, and one observes the Bragg glass state for moderate disorder [36, 41] before transitioning to the amorphous vortex glass state [10]. This is shown in figure 2.2 (a) depicting the schematic

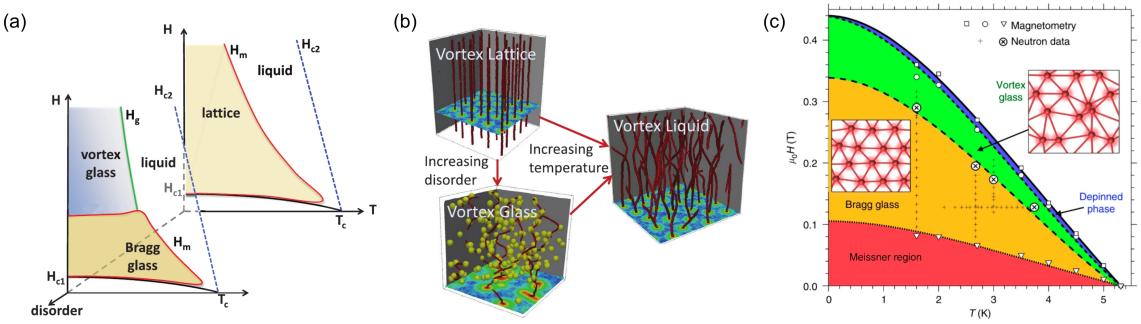

Figure 2.2: Vortex matter states in type-II superconductors. (a) Schematic phase diagram of a clean superconductor without disorder and intermediate degree of disorder. The clean superconductor exhibits the VL and vortex liquid state, whereas, with increasing disorder, the vortices arrange in a Bragg glass or vortex glass in addition to their liquid state. (b) 3D illustrations of the vortex arrangement as a function of temperature and disorder obtained from time-dependent Ginzburg-Landau equations. (c) Phase diagram of a vanadium single crystal sample from magnetometry and neutron scattering experiments. For low fields, the superconductor is found in the Meissner state. With increasing field, the superconductor transitions to the Bragg glass, vortex glass, and depinned liquid state. Panels (a,b) are reprinted with permission from [10]. Copyright (2016) IOP Publishing. Panel (c) is reprinted from [36] under the Creative Commons Attribution 4.0 International License.

phase diagram of a clean superconductor and a superconductor with a finite degree of disorder with the distinct vortex matter states of a lattice, glass, or liquid state. The different vortex configurations are also obtained from numerical calculations based on time-dependent Ginzburg-Landau equations shown in figure 2.2 (b). A controlled variation of the superconducting parameters via nanostructuring allows the use of vortices as a model system for more intricate physics, such as vortex ice [42].

Increasing thermal fluctuations with increasing temperature can induce melting of the VL [43]. This can be traced in the phase diagram of vanadium included in figure 2.2 (c). At a given field, with increasing temperature, the vortices transition from a Bragg glass to a vortex glass and are finally found in the depinned liquid state. However, instead of point-like particles, as in conventional matter, vortices are string-like objects, resulting in an entanglement of the individual vortices in the liquid state [10].

2.2.3 The Intermediate Mixed State and Vortex Clustering

While the Ginzburg-Landau theory offers a useful classification scheme, it is strictly valid only close to T_c. Furthermore, at (T_c, κ_0), often referred to as the Bogomolnyi point, all vortex configurations are degenerate, and the categorization into type-I and type-II breaks down [45]. Instead, one observes a wide range of exotic flux structures in the $\kappa - T$-plane below T_c for superconductors with $\kappa \approx \kappa_0$. A prominent manifestation of non-standard flux structures is the intermediate mixed state (IMS), where flux-free Meissner state domains coexist with mixed state domains as depicted in figure 2.3 showing examples of Bitter decoration images of the IMS in niobium (panel (a)) and a schematic drawing of the phase diagram and the observed phase separation of the homogeneous mixed state

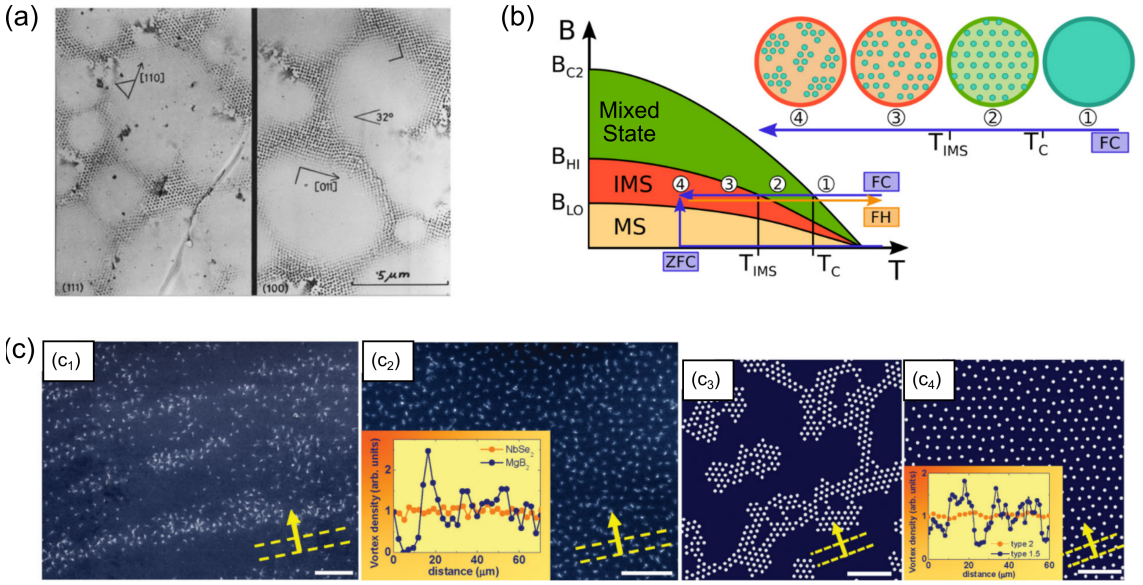

Figure 2.3: Bitter decoration images of vortex matter and vortex clustering in superconductors and schematic phase diagram of the IMS. (a) In the Bitter decoration technique, ferromagnetic particles are evaporated onto the sample, which can then be probed using microscopic techniques. The position of the ferromagnetic particles marks the position of vortices, whereas the light grey areas are the Meissner domains. (b) Schematic drawing of the phase diagram and the observed phase separation of the homogeneous mixed state into VL domains during field-cooled temperature scans. (c) Comparison of Bitter decoration images of vortex clusters in MgB_2 (panel (c_1)) and the homogeneous mixed state in $NbSe_2$ (panel (c_2)), as well as results from numerical simulations (panels (c_3-c_4)) reproducing the experimental results. Panel (a) is reproduced with permission from [9]. Copyright (2011) by Springer Nature. Panel (b) is reproduced with permission from [16]. Copyright (2019) by the American Physical Society. Panel (c) is reproduced with permission from [44]. Copyright (2009) by the American Physical Society.

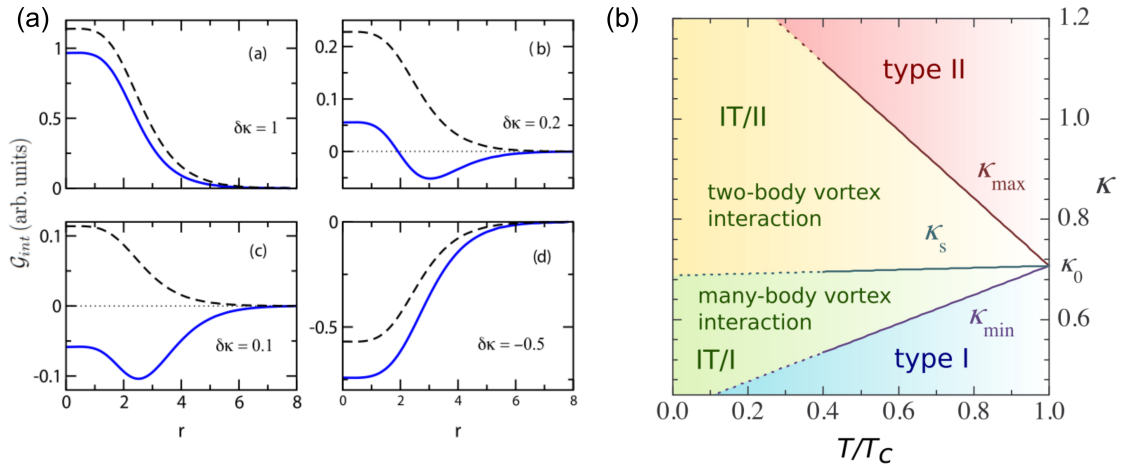

Figure 2.4: (a) Two-body vortex interaction potential as a distance r between vortices for different values of $\delta\kappa = \kappa - \kappa_0$ comparing the results obtained from the EGL (blue solid lines) with results using the classical GL theory (black dashed lines). Within the GL theory, the vortex potential is either purely attractive (type-I) or purely repulsive (type-II), whereas in the EGL, an additional regime with a non-monotonous interaction potential with a global minimum at a finite value $r > 0$ is observed. (b) $\kappa - T$ phase diagram showing the classical type-I and type-II regime and the intertype superconductivity. Both panels are reprinted with permission from [56]. Copyright (2017) by the American Physical Society.

into VL domains during field-cooled temperature scans (panel (b)). Ever since it was first observed via Bitter decoration more than 50 years ago [11], the IMS was studied extensively both theoretically and experimentally [46, 13, 47, 48, 49, 14, 40]. Recent observations of similar flux structures in two-band superconductors MgB_2 [44] and ZrB_{12} [50] (see figure 2.3 (c)) and sometimes referred to as type 1.5 superconductors [44, 51], renewed the interest in the study of the IMS and vortex clustering in different systems [9, 52, 15, 53, 16, 54].

Historically, the type-II regime was further subdivided into type-II/1 and type-II/2 to account for exotic flux structures, such as the IMS not complying with the original type-I/II dichotomy of the original Ginzburg Landau theory. Nb and other low-κ materials with $\kappa \geq \kappa_0$ exhibiting the IMS [55, 47], were referred to as type-II/1, whereas the remaining superconductors with $\kappa \gg \kappa_0$ were referred to as type-II/2. On theoretical grounds, the vortex clustering in low-κ superconductors and the consequent domain formation was explained due to an additional attractive interaction caused by a partial overlap of the vortices [48].

Recently, the group around A. Vagov and A. Shanenko [57, 58] presented the extended Ginzburg Landau formalism (EGL), which can act as a framework to place the type-II/1 regime within the larger phase-space referred to as intertype superconductivity. EGL represents an expansion of the microscopic BCS theory in terms of small deviations of temperature $\tau = 1 - T/T_c$ and the GL parameter $\delta\kappa = \kappa - \kappa_0$ around the Bogomolnyi point (T_c, κ_0) [59]. This expansion does not simply produce more accurate results but, more importantly, can also capture phenomena such as the IMS that are incompatible with the standard GL approach. The results of the perturbative approach within the

EGL formalism have also been confirmed using a fully microscopic description of the IMS [60].

The vortex interaction potential obtained from the classical GL theory as a function of $\delta\kappa$ is either fully attractive, and hence no vortices are stabilized, or fully repulsive, leading to the formation of the homogeneous mixed state. In contrast to that, the EGL shows an additional regime where the interaction potential exhibits a global minimum at a finite distance r. This is shown in figure 2.4 (a) comparing the two-body vortex interaction potential obtained from the classical GL theory with the results from the EGL for different values of $\delta\kappa$. As a result of the non-monotonous vortex interaction, a transitional regime called intertype superconductivity is obtained in addition to the classical type-I and type-II regimes. Figure 2.4 (b) shows the $\kappa - T$ phase diagram of intertype superconductivity obtained within the EGL.

A primary result of the EGL is that many-body vortex interactions become more relevant. In addition to the IT/II phase space roughly corresponding to the type-II/1 phase, where the two-body vortex interaction is sufficient to describe the vortex interaction, intertype superconductivity also encompasses a large phase-space IT/I, where the many-body vortex interactions determine the vortex configurations. The many-body vortex interaction stabilizes vortices in superconductors close to the classical type-I regime, where the two-body interaction would not allow for a vortex matter state [56]. As a result, vortex matter in the IT/I regime is qualitatively different from that observed in type-II and type-II/1 superconductors, where vortices are seen as elementary particles of the mixed state [56]. The many-body character becomes more pronounced in the vicinity of the transition toward the type-I regime.

Figure 2.5 depicts different flux structures obtained from Monte-Carlo simulations using the EGL. As a function of flux density B and $\delta\kappa$, several vortex matter states can be observed, including the homogeneous VL, vortex clustering, as well as disordered and liquid-like behaviors, and multiquanta vortices. Especially the appearance of the liquid-like behavior and the stability of large vortex cluster-droplets in the $\delta\kappa$ range corresponding to the IT/I regime can be seen as a confirmation of the many-body character of the vortex interaction potential [61].

In experiments, vortex clustering was first observed more than 50 years ago using the Bitter decoration technique [11]. The observed patterns encompass labyrinth-like, tubular, and stripe-like patterns and are very similar to the ones observed in the intermediate state of type-I superconductors [9]. Therefore, the vortex clustering was named intermediate mixed state. Studying the intermediate mixed state is a challenging task. Hysteresis loops of the magnetization only show subtle signs of the transition to the IMS [62, 63, 55] as demagnetization effects often blur the transition due to the sample shape. Furthermore, the transition can remain completely buried in temperature scans due to macroscopic flux freezing [16]. Surface-sensitive techniques such as the aforementioned Bitter decoration technique, [11], as well as magneto-optical imaging [64] directly probe the flux distribution at the surface of the sample. However, the surface flux distribution may not represent the underlying bulk structure due to surface defects and vortex branching. Furthermore, as the VL constant is below the resolution limit in magneto-optical imaging, the mixed state domains are sometimes misinterpreted as normal domains, resulting in the false conclusion

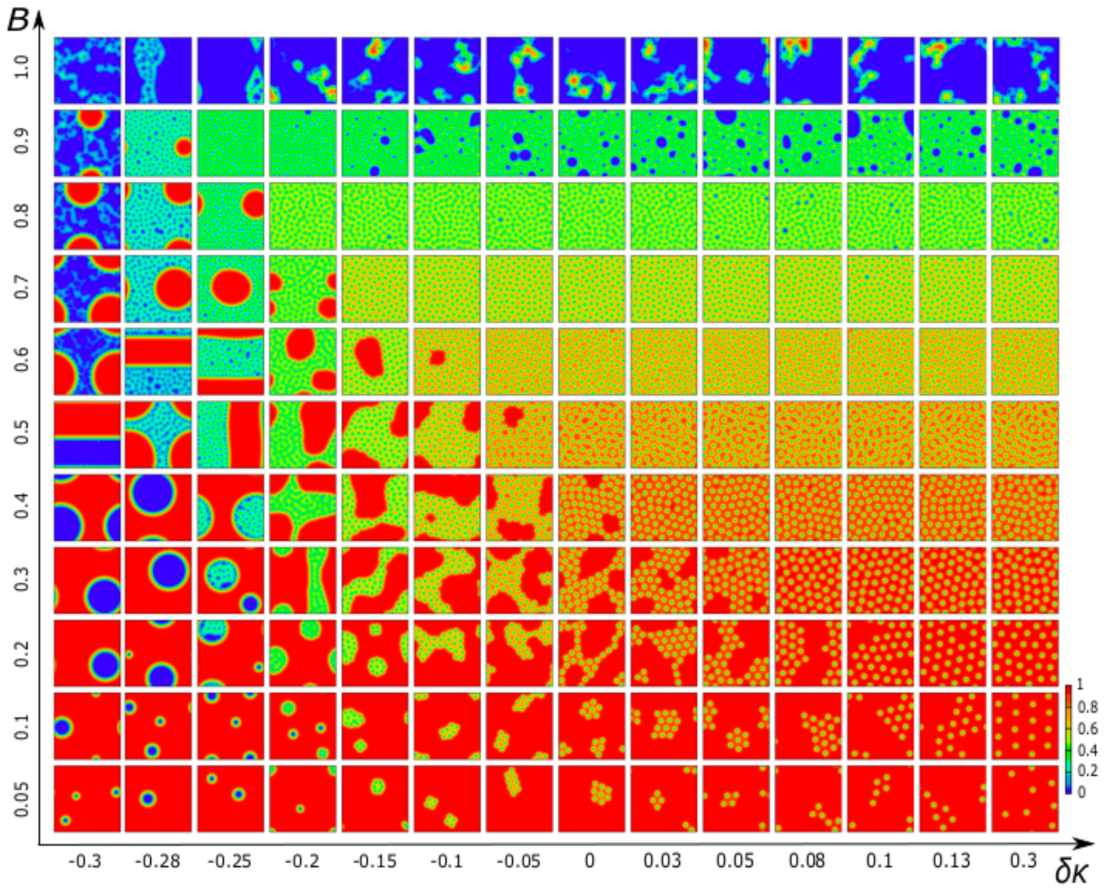

Figure 2.5: Different flux structures obtained from Monte-Carlo simulations using the EGL for different flux densities B and values of $\delta\kappa$. The spatial profile of the superconducting condensate $|\psi|^2$ ranges from zero (blue) to 1 (red). Reprinted with permission from [61]. Copyright (2020) by Springer Nature.

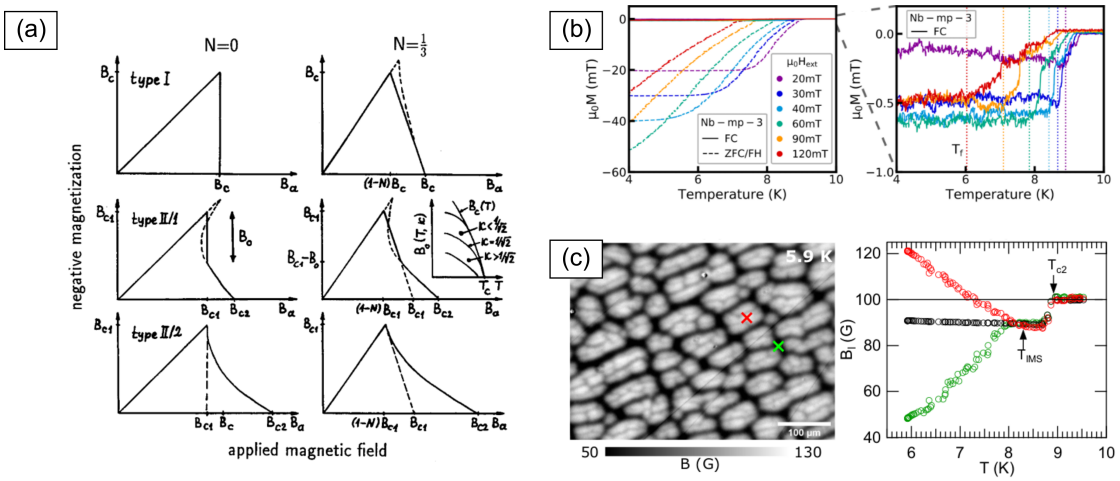

Figure 2.6: Examples of difficulties in experimental studies of the intermediate mixed state. (a) Theoretical magnetization curves of a type-I superconductor (top), type-II/1 superconductor (center), and type-II/2 (bottom) superconductor without ($N = 0$, left) and with demagnetization effects ($N > 0$, right). In the case of $N = 0$ (left), the magnetization curve exhibits a discontinuous jump for a type-I and type-II/1 superconductor, whereas a type-II/2 superconductor shows a gradual decrease of the negative magnetization. For $N > 0$, this discontinuous jump transitions to an area of constant slope, making it difficult to distinguish the IMS from the conventional mixed state. (b) Temperature scans of a Nb single crystal sample. No signs of a transition to the IMS are observed, whereas neutron scattering experiments (see figure 2.7) clearly show that the sample transitions into the IMS. (c) Results from magneto-optical imaging study of the IMS domain structure. In contrast to the Bitter decoration images, dark areas are in the Meissner state, whereas light regions are filled with the VL. The spatial resolution is not sufficient to detect individual vortices. The right panel shows the average internal field in the two positions marked by the green and red cross in the left panel in the same color code, as well as the average induction over the entire area shown on the left (black markers). Panel (a) is reproduced with permission from [9]. Copyright (2011) by Springer Nature. Panel (b) is reproduced with permission from [16]. Copyright (2019) by the American Physical Society. Panel (c) is reproduced with permission from [64], Copyright (2021) by the American Physical Society.

that the observed domain structure in pure niobium is the intermediate state of a type-I superconductor [65].

Neutron scattering techniques, on the other hand, directly probe the bulk properties of the sample and give unambiguous proof of bulk vortex clustering in the IMS [13, 47]. Reimann *et al.* and, more recently, Backs *et al.* [53, 16] studied the IMS in niobium samples of different purity and shape. Using multi-scale neutron techniques consisting of small-angle neutron scattering, neutron grating interferometry (NGI), and very/ultra small-angle neutron scattering (VSANS/USANS) in combination with magnetometry and molecular dynamic simulations (MDS), they studied the IMS transition as a function of field and temperature. SANS gives direct access to the VL morphology via the VL Bragg peaks (see figure 2.7 (a)). Inside the IMS, the VL constant is independent of the applied field, acting as a hallmark of the IMS [13]. This is shown in figure 2.7 (c-d), showing the temperature dependence of the VL constant a_{VL} as a function of the field in samples with varying purity. Remarkably, the temperature dependence of a_{VL} of the three samples could all be fitted with the same phenomenological function shown as black solid lines in

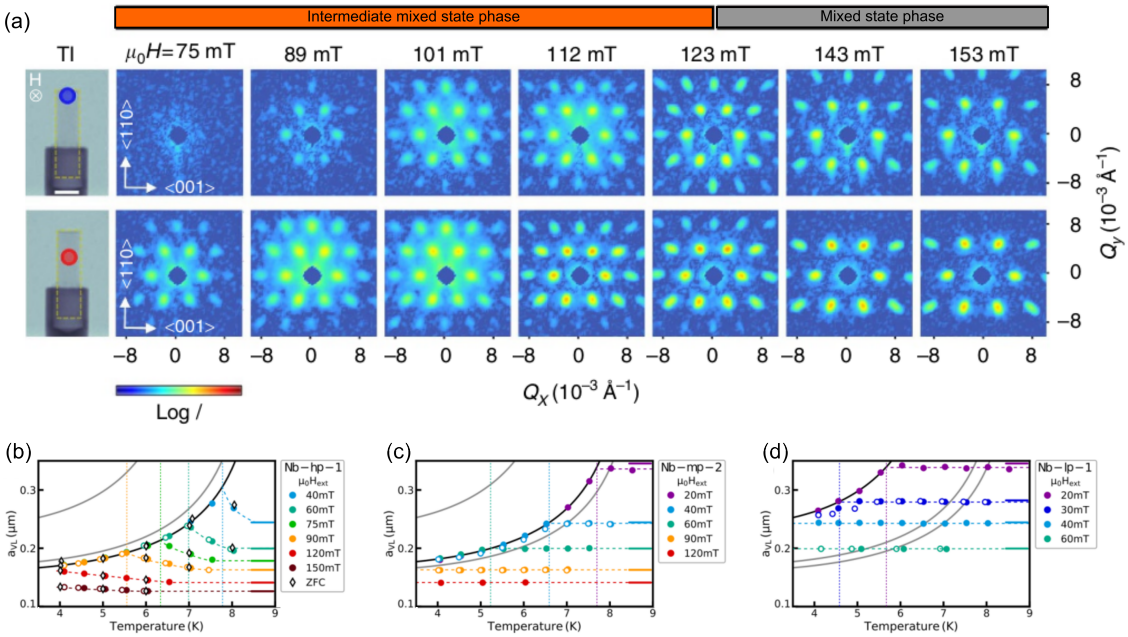

Figure 2.7: Examples of neutron-based studies of the IMS. (a) 2D detector images of the small-angle neutron scattering pattern of the IMS at two different positions in the sample during a field ramp. The VL leads to a hexagonal pattern. The IMS micrometer-sized domain structure leads to diffuse scattering near the masked direct beam. Due to demagnetization effects caused by the sample shape, the penetration of the VL is delayed at the upper end of the sample. (b) Vortex lattice constant a_{VL} as a function of temperature and field for Nb samples of different purity (hp=high purity, mp = medium purity, lp = low purity). a_{VL} is extracted from the SANS Bragg peaks. Inside the IMS, a_{VL} follows a universal field-independent temperature dependence included as a black solid line in each panel. Panel (a) is reproduced from [15] under the Creative Commons Attribution 4.0 International License. Panels (b-d) are reproduced with permission from [16]. Copyright (2019) by the American Physical Society.

figures 2.7 (c-e) and derived from numerical solutions for the superconducting penetration depth λ_L in the Bardeen-Cooper-Schrieffer (BCS) formalism [16]. Furthermore, while magnetization measurements show no indication of the IMS transition in temperature scans (see figure 2.6), SANS experiments revealed that the IMS forms over a wide range of pinning characteristics. This also suggests that the attractive vortex interaction leads to a breakdown of pinning and the formation of the domain structure of the IMS. This pinning breakdown might explain the remarkable stability of the IMS over a wide range of pinning characteristics observed in experiments [53, 16] as well as MDS [54].

The micrometer-sized IMS domain structure was studied using a combination of USANS/VSANS and NGI measurements covering length scales from micrometers to millimeters. Results from USANS measurements indicate that the micrometer-sized inter-domain distance extracted from the correlation peak in USANS patterns is only a function of the applied field but exhibits a constant value in temperature scans. This behavior is reminiscent of the phase-separating behavior encountered in the context of spinodal decomposition. It has been successfully used to model the behavior of the IMS in Nb [53]. The field dependence of the correlation peak agreed well with the field dependence of the do-

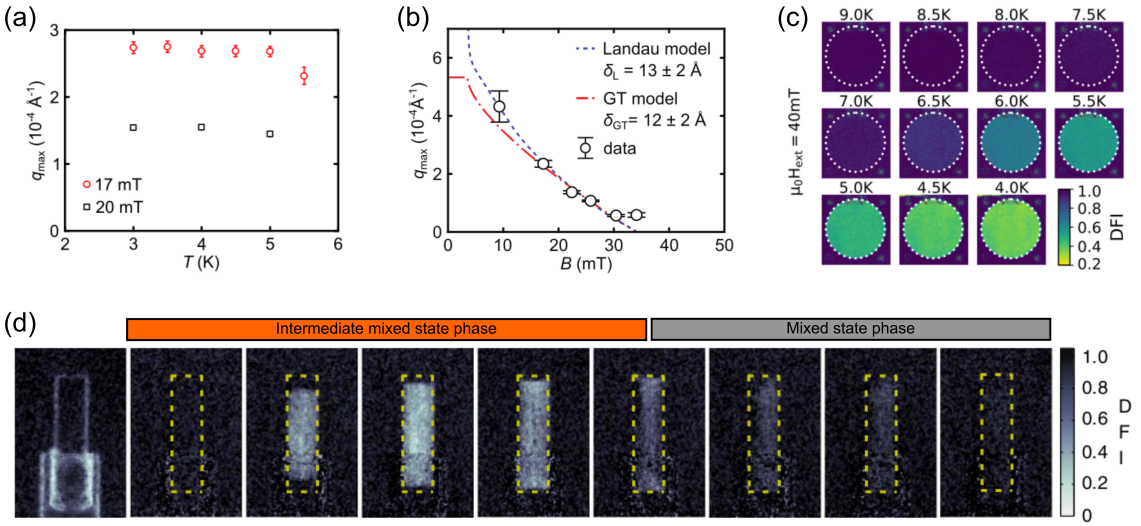

Figure 2.8: Examples of neutron-based studies of the IMS giving access to the micrometer-sized domain structure. (a) Position of the correlation peak in USANS measurements in field-cooled temperature scans. (b) Extracted correlation peaks as a function of the field fitted by the Landau and Goren-Tinkham model of domains in superconductors adapted to the IMS. (c-d) Results of neutron grating interferometry measurements of two Nb single crystal samples of different purity during field-cooled temperature scans and during a field scan showing the dark field image. The dark field image (DFI) provides information on the loss of coherence due to ultra small-angle scattering caused by the micrometer-sized domain structure. A decrease in the DFI corresponds to the presence of the IMS and appears in white. During temperature scans, the DFI is homogeneous over the sample, whereas during field scans, the DFI shows spatial heterogeneity. Panels (a,b) are reproduced with permission from [53]. Copyright (2017) by the American Physical Society. Panel (c) is reproduced with permission from [16]. Copyright (2019) by the American Physical Society. Panel (d) is reproduced from [15] under the Creative Commons Attribution 4.0 International License.

main size derived from the Landau [66] and Goren-Tinkham theory of domains [67] in the intermediate state of type-I superconductors, which was adapted to the domain structure of the IMS [53].

NGI measurements were used to address the spatial distribution of the IMS in the sample during field and temperature scans. During temperature scans, the IMS develops homogeneously, showing no spatial distribution. This contrasts the behavior in field scans where heterogeneous flux distributions can be observed. Measurements on a cylindrical Nb single crystal sample of exceptional purity have shown that the IMS nucleation, as well as the transition to the mixed state phase, are delayed at the sample edges with respect to the sample center (see figure 2.7 (d)). This can also be traced in the SANS patterns shown in figure 2.7 (a). Furthermore, field ramps after field-cooling in a constant applied field resulted in a gradual suppression of the IMS starting from the sample edges [54] according to the critical state model of Bean [68].

While significant advances have been made in the understanding of the field and temperature dependence of vortex clustering in samples of different purity and shape, the influence

of current on the IMS domain structure is still poorly understood and dealt with in the following.

2.3 Current-induced Vortex Matter States

The perfect superconducting state in the vortex-carrying state is only true up to a certain threshold current referred to as critical depinning current. For higher currents, vortices are depinned and start moving in the direction orthogonal to the applied current due to the current-induced Lorentz force $\mathbf{F}_L = \mathbf{J}_t \times \mathbf{B}$ as schematically depicted in figure 2.9 (a). Moving vortices lead to a buildup of a voltage in the direction parallel to the applied current and, hence, the destruction of the zero-resistance state. Inhomogeneities and defects can act as pinning sites, preventing the movement of vortices and recovering the zero-resistance state. As this is the sought-after state in most technological applications, much theoretical and experimental effort has gone into studying the mechanisms involved in vortex pinning and the optimization of the critical depinning current [10, 69] and is discussed in section 3.2.

Besides being relevant for technological applications, the study of current-induced depinning of vortex matter also offers an ideal model system to elucidate more generic phenomena connected to non-equilibrium phases and non-equilibrium phase transitions observed over a wide range of branches of modern physics dealing with driven elastic media in random potentials [70]. Therefore, studying current-induced vortex matter allows us to probe whether universal properties are shared between non-equilibrium states across different physical systems [71]. Yaron *et al.* [72] (see figure 2.9 (b)) showed that driven vortex matter exhibits a two-step depinning process where an initially static, pinned VL first shows disordered plastic motion before it transitions to a coherent moving flux crystal state. The current-induced order can be preserved by quenching the current to zero [73]. The current-induced ordering is also nicely seen in the 2D SANS images from measurements on a Pb–10%In sample (see figure 2.9 (c)). Due to the presence of the transport current, the shape of the flux lines is altered from perfectly straight to continuously bent due to the current-induced magnetic self field [74]. Furthermore, SANS experiments of an Nb wire in the 'force-free' configuration, where the current is applied in the direction parallel to the applied field, and hence $\mathbf{F}_L = 0$, showed that the current-induced self-field leads to a second set of circular vortex loops that coexist with the dominant, axial vortices [75].

Current-induced flux flow is not limited to vortex-carrying superconductors but can also be observed in the intermediate state of type-I superconductors, where normal domains move in the direction orthogonal to the applied current due to the Lorentz force. Recently, it has been shown that a transport current can influence the domain structure and, depending on the history, transform between laminar and tubular flux structures in pinning-free Pb strips [77] (see figure 2.9 (d)).

In the IMS, the heterogeneous domain structure consisting of mixed state and flux-free Meissner state domains represents an additional topological constraint influencing the current distribution in the sample. Due to Ampere's law, current can only exist in areas with a non-vanishing curl of B. As the Meissner state domains are completely flux-free,

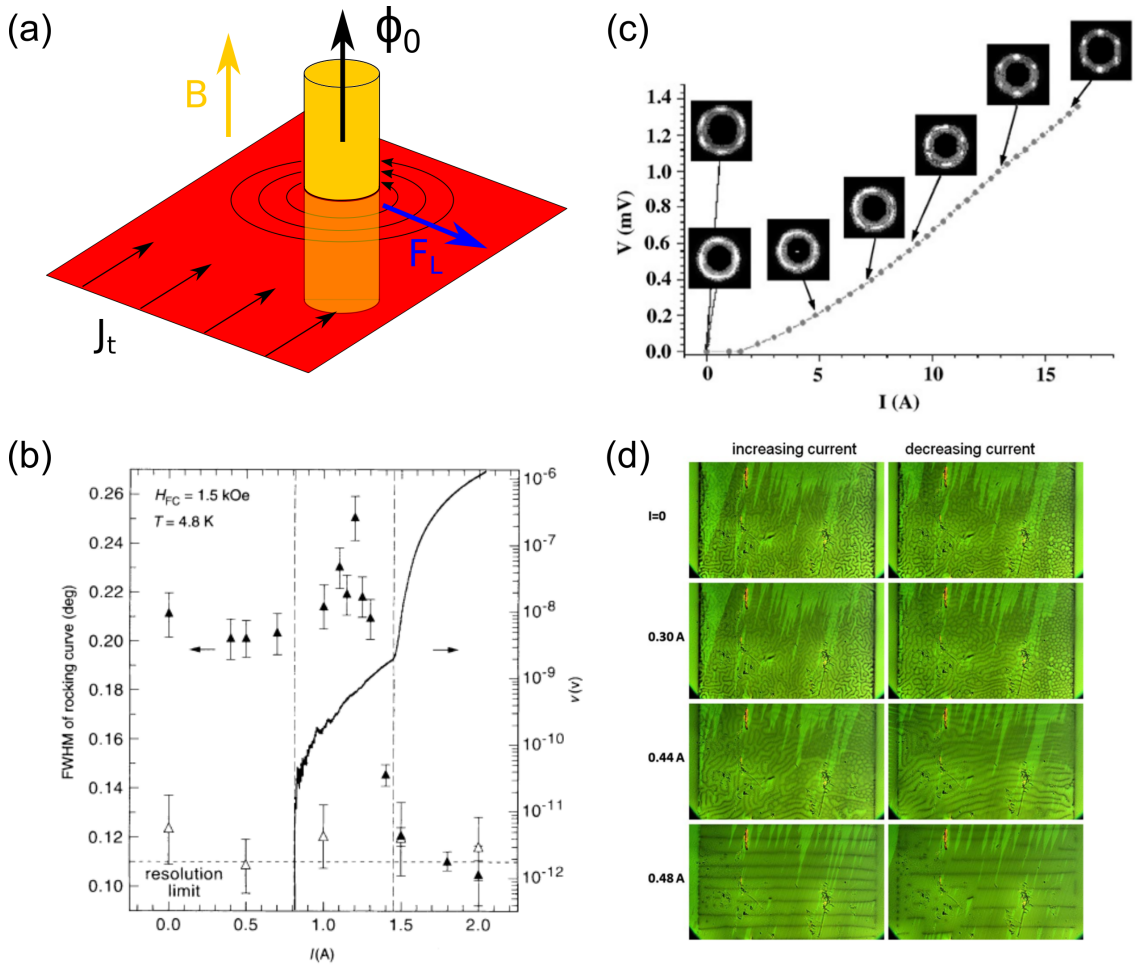

Figure 2.9: Current-induced moving flux structures in superconductors. (a) Schematic drawing of the interaction of a flux line with a transport current J_t leading to the Lorentz force F_L and depinning of the flux line. (b) Vortex lattice disorder in a field-cooled 2H-$NbSe_2$ sample in the mixed state quantified by the rocking curve widths for both increasing (filled triangles) and decreasing (open triangles) currents. The voltage response is shown as a solid line. The VL disorder increases near the critical depinning current and rapidly decreases with increasing voltage. In decreasing current, the VL disorder stays constant. The three different regimes of a pinned lattice, the plastic motion, and the flowing crystal can be traced from the voltage response as well as the VL disorder. (c) Voltage response and SANS images of a Pb–10%In sample after a field-cool and consequent current ramp. The initially disordered VL can be reoriented by the current, which is preserved after the current is removed. (d) Flux structures in the intermediate state of Pb samples in a constant field H=350 Oe while increasing the current from zero (left) and decreasing the applied current after the sample was driven to the normal state using current (right). Panel (b) is reprinted with permission from [72]. Copyright (1995) Springer Nature. Panel (c) is reprinted with permission from [76]. Copyright (2003) Elsevier. Panel (d) is reprinted with permission from [77]. Copyright (2008) American Physical Society.

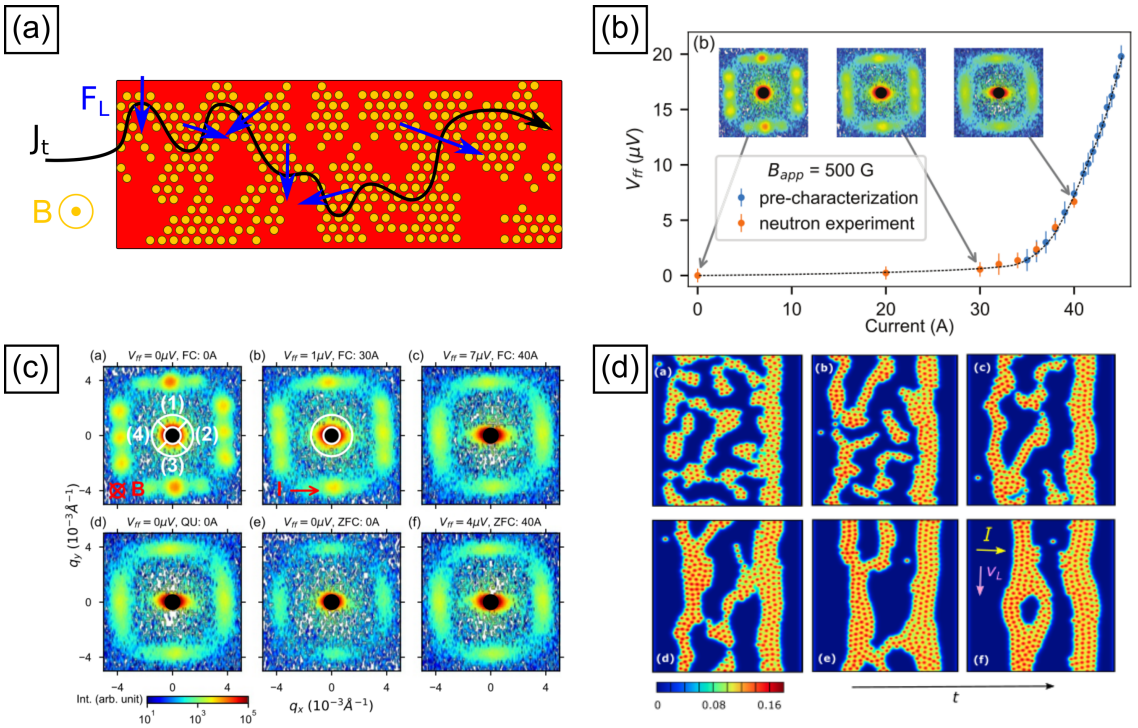

Figure 2.10: Flux flow in the intermediate mixed state. (a) Schematic drawing of a potential current path in the IMS. (b) I-V characteristics of an Nb single crystal and the corresponding SANS pattern. (b) 2D SANS images of the IMS as a function of current and different measurement procedures. The current, voltage V_{ff}, and measurement procedure are indicated above each panel. The current and field directions are indicated in red at the bottom of the first two panels of the first row. A field-cool (FC) followed by a current ramp up to 40 A induces a rearrangement of the IMS domains as inferred from the current-induced anisotropy in the horizontal direction. The rearrangement is preserved when the current is quenched to zero (QU). No ordered VL is obtained after a zero field cool followed by a field ramp. However, a consequent current ramp to 40 A yields the same scattering pattern as is obtained in the corresponding FC measurement procedure. (d) Numerical simulations of the IMS time evolution showing the spatial distribution of the magnetic field. The initial random domain structure is rearranged to parallel stripes under the influence of the current. This is consistent with the experimental results. Panels (b-d) are reprinted from [17] under the Creative Commons Attribution 4.0 licence.

current is constrained to the mixed state domains, its interfaces with the Meissner state domains, and the sample's surfaces, creating an interesting scenario for vortex matter studies as schematically shown in figure 2.10.

Until recently [17], the influence of a transport current on the IMS domain structure remained experimentally unexplored. Using a combined transport measurement and SANS setup, it was found that the IMS persists in the flux flow state. Furthermore, the SANS results showed that the initial random domain structure rearranged into an aligned stripe structure oriented orthogonal to the applied current. The realigned structure was preserved when the current was rapidly removed. The absence of hysteretic behavior following different measurement procedures suggests that the aligned stripe pattern is the steady state configuration in the flux flow regime. The experimental results were complemented by numerical simulations using a system of coupled time-dependent Ginzburg-

Landau (TDGL) equations acting as a qualitative model to study the time evolution of the current-induced rearrangement of vortex clusters [17]. While based on a simplified model, the simulation results included in figure 2.10 (d) agreed well with the experimental observations of a current-induced rearrangement to a stripe structure and painted a detailed picture of the rearrangement process.

3 Experimental Methods

After having reviewed superconductivity and the plethora of magnetic flux structures in superconductors, we will summarize the experimental methods used within the scope of this thesis to study vortex matter in the intertype superconductor Nb. We first focus on lab-based characterization tools to characterize the magnetic and electrical properties of superconductors. Section 3.1 introduces the reader to the main concepts of magnetic susceptibility measurements on superconducting materials. We then turn to transport measurements of superconductors and pinning theory in section 3.2. The section concludes with a brief introduction to neutron scattering with a focus on the peculiarities of small-angle neutron scattering from large magnetic structures.

3.1 Magnetic Susceptibility

AC susceptibility is a widespread technique used to characterize magnetic and superconducting samples. In this section, we introduce the reader to the terminology and the basic principle of AC susceptibility with a focus on superconducting vortex matter, roughly following [78] and [79]. We also refer the reader to the latter for the treatment of AC susceptibility measurements in other magnetic systems.

In general, magnetic susceptibility, both DC and AC, quantifies the magnetic response of a sample to an external magnetic field H given as

$$\chi = \lim_{H \to 0} \frac{M}{H}, \tag{3.1}$$

where M is the magnetization of the sample. As the limit of zero field can not be approached in experiments, the susceptibility is often measured as a differential susceptibility given as

$$\chi_{exp} = \frac{\delta M}{\delta H} \approx \mu_0 \frac{\delta M}{\delta B}, \tag{3.2}$$

where $\delta B = \mu_0 \delta H$ is a finite applied magnetic field and we used $B = \mu_0(H + M) \approx \mu_0 H$ in the case of $\chi \ll 1$.

In DC magnetic susceptibility measurements, δB is a small static magnetic field, and the resulting magnetization δM is recorded, for example, as a function of temperature to yield $M(T)$ and hence $\chi(T)$ via equation 3.2.

In AC magnetic susceptibility measurements, a time-varying magnetic field of the form $H_{AC} = H_{ac} \cos(\omega t)$ is applied to the sample. In general, the measured magnetisation M_{AC} is now time-dependent and the AC susceptibility χ_{AC} is defined according to

$$\chi_{AC} = \frac{M_{AC}}{H_{AC}}, \tag{3.3}$$

where it was assumed that the response of the sample to the drive is linear and that χ_{AC} is a constant proportionality factor.

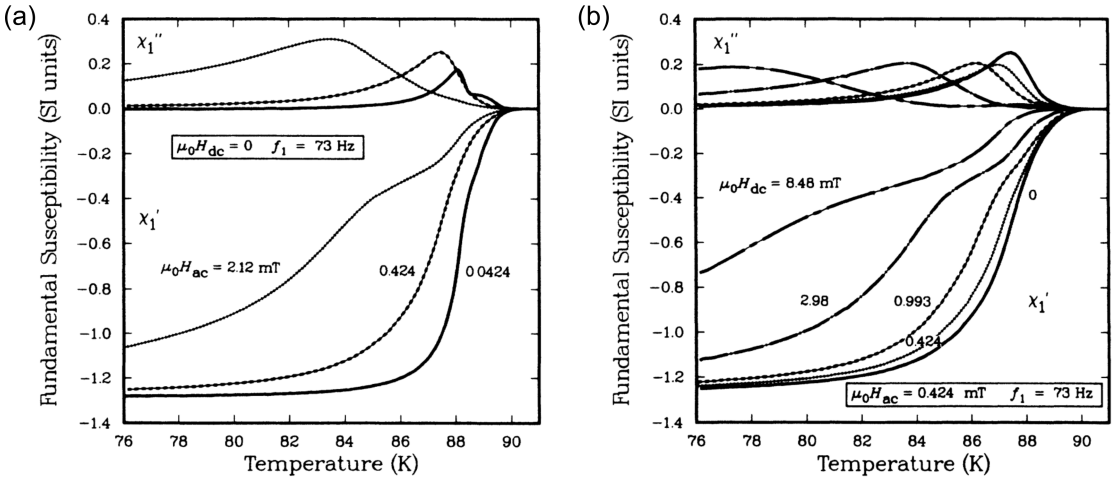

Figure 3.1: Examples of temperature scans of χ' and χ'' for (a) different values of the drive amplitude $\mu_0 H_{AC}$ and (b) different values of the static applied magnetic field $\mu_0 H_{dc}$. The drive frequency is constant for both panels. Note that the shown data is not corrected for the demagnetization factor of the studied specimen explaining why the low-temperature value of χ' is not approaching -1. Reprinted with permission from [80]. Copyright (1990) American Physical Society.

In general, the magnetic response is not in phase with the driving field, and the AC susceptibility is complex-valued $\chi_{AC} = \chi'_{AC} + i\chi''_{AC}$. In conventional magnetic systems, where the magnetization is determined by the magnetic moments of individual atoms, this phase lag can be related to the characteristic magnetic relaxation time τ of the magnetic moments due to the different coupling interactions between them.

The magnetization of the superconducting state is characterized by the Meissner screening currents and the superconducting vortices. Type-I superconductors are only found in the Meissner state, where an external magnetic field is completely screened, and the magnetization is given as the negative applied magnetic field. Therefore, the magnetic response of a type-I superconductor yields $\chi_{AC} = -1$. In type-II superconductors, where the field can enter the sample in the form of vortices, the scenario is slightly more complicated, and the penetration of an external magnetic field depends on the pinning characteristics of the sample.

Due to the presence of vortices and their ability to be unpinned via the Lorentz force, the AC magnetic response of superconductors does not only depend on the drive frequency of the AC field as is the case for other magnetic systems characterized only by a relaxation time τ [79]. Instead, the AC susceptibility of superconductors also depends on the amplitude H_{ac} of the drive field as well as the strength of a potential additional static DC magnetic field. Additionally, in this thesis in section 5, we will explore the effect of a transport current on the AC susceptibility signal.

Examples of temperature scans of χ' and χ'' of a superconductor in different static fields and for different drive amplitudes are shown in figure 3.1. The general temperature dependence shows a pronounced drop of χ' with falling temperature corresponding to the shielding of the external magnetic field via the Meissner shielding currents. The temper-

ature dependence of χ'' shows a peak below the transition temperature T_c corresponding to the temperature where the AC field penetrates the center of the sample. Both of these contributions are dependent on the AC field and the DC field and also show a frequency dependence [80, 79]. In addition to that, polycrystalline samples, as is often the case in the study of high-temperature superconductors, usually show an additional broadening in the transition of χ' and can exhibit a double peak structure of χ'' due to the coupling between the individual grains [81].

The theoretical description of a superconductor filled with vortices to an AC magnetic field is linked to the mobility of vortices. In the case that the vortices are only weakly pinned and the AC field penetrates the sample through viscous vortex flow, the AC response can be modeled within the linear diffusion model. If vortices are no longer only weakly pinned, the AC magnetic susceptibility can be described using Bean's critical state model, where the field gradient corresponds either to the local critical current density or is zero. The two scenarios have different parameters influencing the magnetic response and are plotted in figure 3.2 showing the terms χ' and χ'' for the linear diffusion model (panel (a)) and the Bean's critical state model (panel (b)). We first focus on the linear diffusion model.

In the case of the linear diffusion model, the penetration depth of the AC magnetic field is governed by $\delta = \sqrt{2\rho/\mu_0\omega}$ where ω is the drive field frequency and ρ is the resistivity of vortex flow [79]. The magnetic response is governed by the dimensionless ratio $x_{lin,diff}$ given as

$$x_{lin,diff} = \frac{\omega}{(\mu_0 d^2/2\rho)}, \tag{3.4}$$

where $\omega = 2\pi f$ is the frequency of the drive field, d is the sample thickness, μ_0 is the vacuum permeability, and ρ is the flux flow resistivity. Considering a fixed value of ρ, this can be explained in the following way. For low frequencies, the AC field completely penetrates the sample, resulting in $\chi' \to 0$ and $\chi'' \to 0$. For very high frequencies, the penetration depth is very small, and the magnetic field is almost entirely screened, resulting in $\chi' \to -1$ and $\chi'' \to 0$. We note that the flux flow resistivity ρ is a tunable parameter and can be changed by changing the DC field according to $\rho \approx \rho_n \frac{B}{B_{c2}}$.

In the second case of strongly pinned vortices, the response is no longer linear and includes non-vanishing higher harmonic terms. Using Bean's critical state model, the fundamental terms can be linked to the ratio of the AC driving field $B_{ac} = \mu_0 H_{ac}$ and the critical depinning current J_c for flux flow and are shown in figure 3.2 (b). Considering a fixed value of J_c, we can distinguish between the two limiting scenarios. For low values of B_{ac}, the AC field is almost completely screened and only penetrates a small surface layer. Correspondingly we observe $\chi' \to -1$ and $\chi'' \to 0$. For high values of B_{ac}, the entire sample is penetrated by the AC field, and analogous to the linear diffusion model, this results in $\chi' \to 0$ and $\chi'' \to 0$. The maximum absorption occurs if the penetrating AC field generates a gradient that is comparable to the magnetic field gradient corresponding to the critical depinning current.

In our experiments, the AC susceptibility is measured making use of the mutual inductance method using an AC susceptometer. In a typical AC susceptometer, an excitation coil provides the AC magnetic driving field, while a pick-up coil is used to record the magnetic response of the sample subjected to the driving field. Optionally, DC magnet coils provide an additional static DC magnetic field.

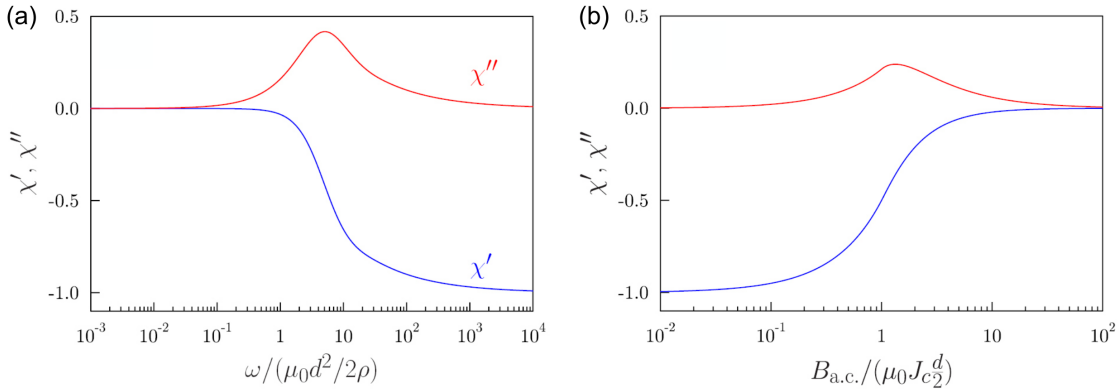

Figure 3.2: Theoretical AC susceptibility signal: (a) Linear diffusion and (b) Bean's critical state model. Reprinted with permission from [79]. Copyright (2019) IOP Publishing.

The induced voltage in the pick-up coil is created by the change in total magnetic flux through the pick-up coil. The total magnetic flux consists of a contribution from the sample via its magnetization and the AC field created by the driving coil. By connecting two identical but counter-wound coils in series as a pick-up coil and placing the sample in one of the two coils, the contribution of the AC field can be nulled. Therefore, the induced voltage is only proportional to the change in magnetization of the sample, which can be written as

$$v(t) = -d\Phi/dt = -\alpha \cdot dM/dt, \tag{3.5}$$

where we subsumed geometrical contributions like the coil shape, total winding number, etc., in the constant α. Similar to the average magnetic flux density, M can be written as a Fourier expansion

$$M(t) = M_0 + \sum_{n=1}^{\infty} H_{ac} \left(\chi_n' \cos(n\omega t) + \chi_n'' \sin(n\omega t) \right), \tag{3.6}$$

resulting in the voltage

$$v(t) = \alpha H_{ac} \omega \sum_{n=1}^{\infty} n \left(\chi_n' \sin(n\omega t) - \chi_n'' \cos(n\omega t) \right). \tag{3.7}$$

Again, only considering $n = 1$, we deduce for the voltage $v_1(t)$

$$v_1(t) = \alpha H_{ac} \omega \left(\chi' \sin(\omega t) - \chi'' \cos(\omega t) \right), \tag{3.8}$$

where we have dropped the index 1 as we only concentrate on the $n = 1$ term in our measurements.

If the measurement system doesn't show any parasitic effects resulting in any additional phase shifts, χ' is contained in the voltage signal shifted by $\pi/2$, while χ'' can be extracted from the voltage signal measured at a phase shift of π with respect to the drive field of the form $H_{AC} = H_{ac}\cos(\omega t)$.

3.2 Transport Measurements and Pinning Theory

A transport current density $\boldsymbol{J}$ applied to a superconductor filled with vortices and mean induction $\boldsymbol{B}$ induces the Lorentz force

$$\boldsymbol{F}_L = \boldsymbol{J} \times \boldsymbol{B}, \tag{3.9}$$

which is given as a force per unit volume. In a perfect superconductor without any defects, any current $J > 0$ leads to a moving VL of velocity $\boldsymbol{v}$. The movement of vortices induces an electromotive force, which is driving the normal electrons in the vortex core, resulting in an Ohmic loss. This is equivalent to the destruction of the zero-resistance state and hence hinders the technological applications of superconductors. The lossless state can be recovered by preventing the movement of vortices [82].

In real materials, inhomogeneities and defects such as dislocations and normal precipitates represent areas of lower condensation energy and can act as pinning sites for individual vortices, preventing their movement. This is schematically depicted in figure 3.3 (a), showing two vortices, of which one is positioned on top of two defects representing areas of lower condensation energy. If the normal core, modeled as a flexible tube of radius ξ_{GL}, is running through a defect of lower condensation energy, its potential energy is reduced by the amount $\Delta \mathrm{E}_{\mathrm{pot}} = \tilde{\mathrm{E}}_{\mathrm{cond}} \pi \xi^2 L_D p$. Here, $\tilde{\mathrm{E}}_{\mathrm{cond}}$ is the condensation energy per unit volume, L_D is the length over which the vortex is running through a defect and p is a parameter in the range from 0 to 1 quantifying the reduction of the condensation energy inside the defect [83].

The vortex occupies a state of minimal potential energy as represented in figure 3.3 (b), showing the potential energy as a function of distance r from the axis of the vortex. The extent of the potential well is characterized by the width of the defect r_p. The resulting elementary pinning force is determined by the gradient of the potential energy and can be approximated as $f_p = -\frac{\delta \mathrm{E}_{\mathrm{pot}}}{\delta r} \approx -\frac{\Delta \mathrm{E}_{\mathrm{pot}}}{r_p}$ [83]. The action of these elementary pinning forces on the VL results in the macroscopic pinning force density F_p counteracting the Lorentz force. As a result, vortices remain pinned for current densities up to a critical value $J_c = \frac{F_p}{B}$.

The theoretical determination of F_p is a challenging problem as it is not generally given as the sum of the elementary pinning forces but requires taking into account the interaction of the elastic VL with the statistically distributed pinning sites. This is known as the summation problem [82]. The calculation of F_p highly depends on the density of pinning sites, the strength and range of the elementary pinning force, and the density and the elastic properties of the vortices determined by the magnetic field and temperature. However, the resulting field dependence often yields a power-law of the form B^m. Therefore, fitting the exponent of the experimentally observed field dependence of the critical depinning current can reveal details about the underlying pinning mechanism.

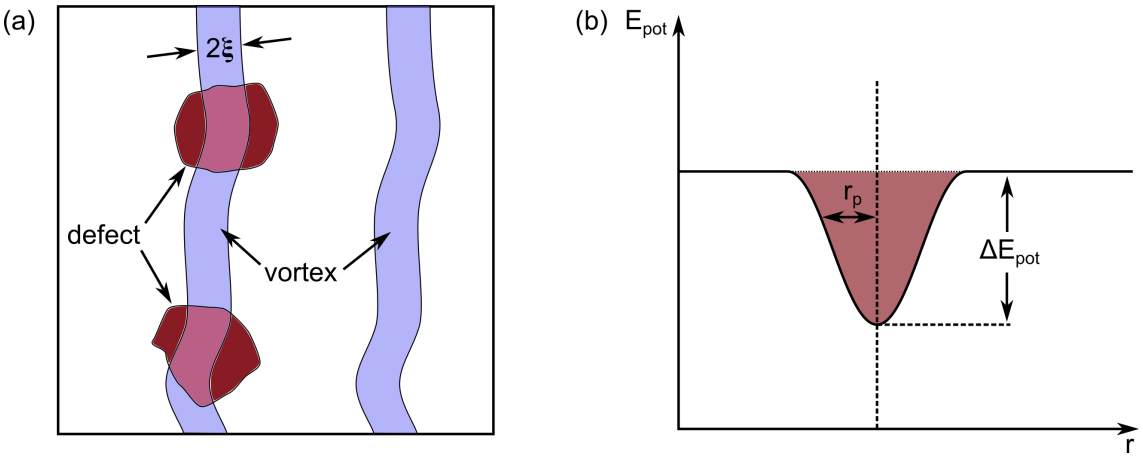

Figure 3.3: (a) Schematic representation of vortex pinning due to defects and (b) the potential energy curve in the direction orthogonal to the vortex axis. Reproduced from [83].

Table 3.1: Field dependence of the critical depinning current in different pinning regimes. Adapted with permission from [10]. Copyright IOP Publishing (2016).

Collective Pinning		**Strong Pinning**		
$R_c < \lambda_L$	$R_c > \lambda_L$	Direct collision	Trapping instability	All pins occupied
$\exp(-\alpha B^{3/2}/n_p)$	$n_p^2 B^{-3}$	$n_p B^{-1/2}$	$n_p B^{-5/8}$	$n_p B^{-1}$

The different pinning mechanisms are usually split into two subgroups: (i) collective pinning refers to the combined action of a large collection of weak pinning sites, and (ii) strong pinning refers to a scenario where the individual pinning sites have a large pinning force but are dilute and act on individual vortices. The theoretical treatment of these different scenarios yields different field dependencies discussed in the following.

For collective pinning, two regimes exist and are separated based on the relative size of the London penetration depth λ_L and the extent of the well-ordered VL in the transverse direction quantified by the transverse Larkin length R_c [69, 10]. The field dependence of the critical depinning current in the collective pinning regime is determined by the stiffness of the VL quantified via the shear and tilt modulus. One can distinguish two different regimes: (i) For $\lambda_L < R_c$ the critical current has a field dependence $\propto B^{-3}$ and the rapid decrease of J_c is mostly caused by a stiffening of the VL with increasing field [10]. For $\lambda_L > R_c$, the field dependence becomes exponential.

For strong pinning, the field dependence shows two regimes depending on the fraction of pin sites occupied. For the case that pin sites remain unoccupied, the critical current scales with an exponent close to $-1/2$, where slight differences appear if individual pins are only able to directly trap vortices close to their ideal lattice position (direction collision: $m = -1/2$) or whether the pin-sites can also trap remote vortices (trapping instability: $m = -5/8$). Above a threshold field, where all pin sites are occupied by vortices, the critical depinning current scales as B^{-1}. The different pinning mechanisms and their field dependence are summarized in table 3.1.

For currents exceeding the critical depinning current, vortices are depinned. In the flux flow state for $J > J_c$, the Lorentz force is counteracted by the pinning force and the viscous or drag force connected to the mechanism of Ohmic energy dissipation due to the movement of the vortices. Both forces act in the direction opposite to the vortex motion given by the unit vector $\boldsymbol{\delta} = \boldsymbol{v}/|\boldsymbol{v}|$ with the velocity of the vortices $\boldsymbol{v}$ and depend on the magnitude of the magnetic induction $|\boldsymbol{B}|$ and temperature T. Again, given as a force per unit volume, they read

$$\boldsymbol{F}_p = \quad -F_p(|\boldsymbol{B}|, T)\boldsymbol{\delta}, \tag{3.10}$$

$$\boldsymbol{F}_v = \quad -\eta(|\boldsymbol{B}|, T)\tfrac{|\boldsymbol{B}|}{\Phi_0}\boldsymbol{v}, \tag{3.11}$$

with η the viscous coefficient related to the flux flow resistivity [82].

The moving vortices result in a buildup of an electric field parallel to the direction of the transport current. This is equivalent to a breakdown of the zero-resistance state. In the usual geometry, where the current and the magnetic field are perpendicular to each other, the electric field $\boldsymbol{E}$ in the steady state is given as

$$\boldsymbol{E} = \boldsymbol{v} \times \boldsymbol{B}, \tag{3.12}$$

where $\boldsymbol{v}$ is governed by the balance of forces given as

$$\boldsymbol{F}_L + \boldsymbol{F}_p + \boldsymbol{F}_v = 0. \tag{3.13}$$

The response in the flux-flow regime is Ohmic with a flux flow resistance R_{ff} proportional to the normal state resistance R_n and the applied field B derived within the Bardeen-Stephen model [84]

$$R_{ff} \propto R_n \frac{B}{B_{c2}}. \tag{3.14}$$

In addition to the current-induced depinning, vortices can also be depinned via thermal activation, often referred to as thermally activated flux creep. Flux creep is a stochastic process governed by the Arrhenius expression $\exp -U/k_BT$, where U represents an energy barrier that has to be overcome to reach a different local minimum in the potential energy. The attempt frequency is given as $\nu_0 = \Phi_0\alpha_L/2\pi B\eta$, where the Labusch parameter α_L describes the harmonic approximation of the restoring force density $F = -\alpha_L u$ for a displacement u around the current equilibrium vortex position and η is the viscous coefficient [82]. In general, the hopping distance is comparable to the lattice spacing a_{VL}. The induced electric field due to thermal activation in the direction of the transport current is then given by

$$E = Ba_{VL}\nu_0 \left[\exp\left(-\frac{U}{k_BT}\right) - \exp\left(-\frac{U'}{k_BT}\right)\right], \tag{3.15}$$

where U and U' are the energy barrier in a parallel and antiparallel direction to the Lorentz force, respectively, as flux creep is possible in all directions.

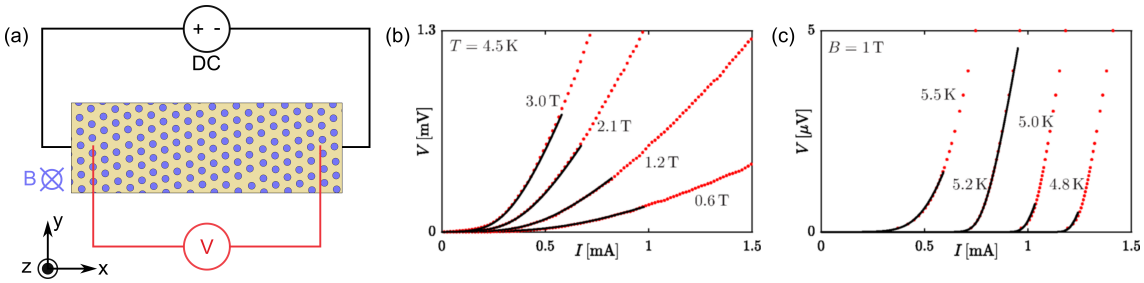

Figure 3.4: Transport measurements of superconductors. (a) Schematic drawing of a four-probe transport measurement setup. (b) I-V characteristics of $\alpha-$MoGe sample in different applied fields in a constant temperature. (c) I-V-characteristics of 2H-$NbSe_2$ sample in a constant applied field measured at different temperatures. Panels (b,c) are reprinted with permission from [85]. Copyright (2019) American Physical Society.

Especially for high-temperature superconductors, thermally activated flux creep is more pronounced and represents a major hindrance in the technological application of superconductors at temperatures close to their transition temperatures T_c. For low-temperature superconductors such as niobium, thermally activated flux creep plays a minor role [10].

Most commonly, the electrical properties of superconductors are studied using the four-probe method schematically depicted in figure 3.4 (a). In a standard four-probe setup, the current is applied to the sample using a pair of current leads, and the voltage across a portion of the sample in between the two current contacts is recorded.

Figures 3.4 (b,c) include experimental results obtained from two superconducting samples either for different applied fields and at a constant temperature or for a constant applied field at varying temperatures. The general shape of the individual curves is qualitatively identical, showing a vanishing voltage at low currents and a linear flux flow regime at high currents above the critical depinning current I_c. In the direct vicinity of I_c, the voltage response shows a finite curvature, which becomes more pronounced with increasing temperature due to the increased impact of thermal fluctuations. The slope in the flux flow is proportional to the applied field as expected from equation 3.14.

3.3 Neutron Scattering

Neutron scattering is a well-established technique to study magnetic bulk samples. We give a brief summary of the main concepts with a focus on the scattering from superconducting VLs and from large magnetic domains in the micrometer range roughly following [86] and [87]. An introductory level treatment of neutron scattering theory can be found in the textbook by Sivia [88] while Squires [89] or Schober [90] provide a more in-depth treatment of neutron scattering.

In neutron scattering, we distinguish between nuclear scattering, resulting from the interaction of the neutron with the atom core via the strong nuclear force, and magnetic scattering, caused by the dipole-dipole interaction of the spin-$\frac{1}{2}$-carrying neutrons with the magnetic moments present in the sample. For thermal and cold neutrons with typical wavelengths of λ_N of several Å, these two interaction potentials are inherently different.

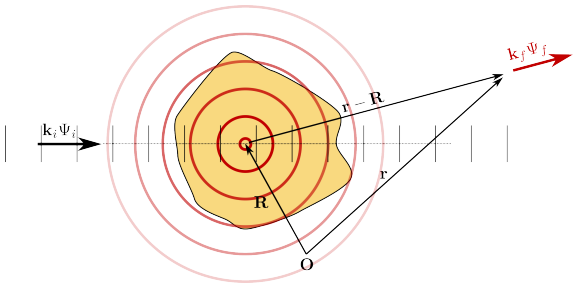

Figure 3.5: Schematic drawing of the scattering process. The incoming neutron $(\boldsymbol{k}_i, \Psi_i)$ is scattered at the position $\mathbf{R}$. For weak scattering within the Born approximation, the scattered neutron $(\boldsymbol{k}_f, \Psi_f)$ is given as the superposition of the initial plane wave with a spherical wave origination at $\mathbf{R}$.

The range of the strong nuclear force ($\approx 10^{-4}$ Å) is small compared to the neutron wavelength. Therefore, the nuclear scattering interaction potential can be considered point-like. The strength of the interaction is quantified using the scalar parameter named scattering length b, which is isotope and spin-dependent. Hence, the nuclear interaction potential of the neutron with the sample consisting of N atoms at positions $\mathbf{r}_i$ can be well-described using the Fermi pseudo-potential

$$V_{nuc}(\mathbf{r}) = \frac{2\pi\hbar^2}{m} \sum_{i=1}^{N} b_i \delta(\mathbf{r}_i), \tag{3.16}$$

where b_i is the scattering length of the atom at position $\mathbf{r}_i$.

The interaction of the neutron with an external or internal magnetic field $\mathbf{B}$ is governed by the Zeeman interaction

$$V_{mag}(\mathbf{r}) = -\boldsymbol{\mu} \cdot \mathbf{B}(\mathbf{r}), \tag{3.17}$$

with the magnetic dipole moment of the neutron $\boldsymbol{\mu}$. The principal source of magnetic constituents in samples comes from unpaired electrons. Therefore, the magnetic interaction of thermal neutrons can no longer be considered point-like and has a directional dependence expressed via the dot product in equation 3.17.

Mathematically, the wave properties of the neutron are described using the stationary Schrödinger equation

$$E\Psi(\boldsymbol{k}, \boldsymbol{r}) = \left[-\frac{\hbar^2}{2m} \nabla^2 + V(\boldsymbol{r}) \right] \Psi(\boldsymbol{k}, \boldsymbol{r}), \tag{3.18}$$

with the neutron mass m, energy E, wave function Ψ and interaction potential V.

In a scattering process, we are interested in the wave function of the neutron after it interacts with the sample. This process is schematically depicted in figure 3.5.

The wave function of the incoming neutron Ψ_i (where $V = 0$) is given by solving equation 3.18. The solution is a plane wave of the form

$$\Psi \propto \exp\left(ikx\right), \tag{3.19}$$

with the wavevector k given as

$$k^2 = \frac{2mE}{\hbar^2}. \tag{3.20}$$

The wave function of the scattered neutron after it has interacted with the sample can be obtained by solving the Schrödinger equation, this time with $V \neq 0$. A solution of the Schrödinger equation is given implicitly by the Lippmann-Schwinger equation

$$\Psi_f\left(\boldsymbol{k_f}, \boldsymbol{r}\right) = \Psi_i\left(\boldsymbol{k_i}, \boldsymbol{r}\right) - \frac{m}{2\pi\hbar^2} \int \frac{\exp\left(ik_f\left|\boldsymbol{r}-\boldsymbol{R}\right|\right)}{\left|\boldsymbol{r}-\boldsymbol{R}\right|} V(\boldsymbol{R}) \Psi_f\left(\boldsymbol{k_f}, \boldsymbol{r}\right) d\boldsymbol{R}. \tag{3.21}$$

By iteratively inserting $\Psi_f\left(\boldsymbol{k_f}, \boldsymbol{r}\right)$ into the right-hand side of equation 3.21, we obtain the solution in the form of an expansion, called the Born series. In the case of a weak interaction potential, this expansion can be interrupted after the first integral term leading to the Born approximation for Ψ_f [90].

$$\Psi_f\left(\boldsymbol{k_f}, \boldsymbol{r}\right) = \exp\left(i\boldsymbol{k_i} \cdot \boldsymbol{r}\right) + \frac{\exp\left(i\boldsymbol{k_f} \cdot \boldsymbol{r}\right)}{r} f(\boldsymbol{q}), \tag{3.22}$$

where q denotes the wavevector transfer $\boldsymbol{q} = \boldsymbol{k_f} - \boldsymbol{k_i}$. The interaction of the neutron with the sample is contained in the scattering amplitude $f(\boldsymbol{q})$ given as the Fourier transform of the interaction potential

$$f(\boldsymbol{q}) = -\frac{m}{2\pi\hbar^2} \int V(\boldsymbol{R}) \exp\left(-i\boldsymbol{q} \cdot \boldsymbol{R}\right) d\boldsymbol{R} \tag{3.23}$$

The measured quantity in elastic neutron scattering experiments is the scattering intensity given as the number of neutrons per second scattered into the solid angle element $d\Omega$. It can be connected to the differential scattering cross section $\frac{d\sigma}{d\Omega}$ defined by

$$\frac{d\sigma(\boldsymbol{q})}{d\Omega} = \frac{\#\text{ of neutrons per second scattered into } d\Omega}{\Phi_{in} \times d\Omega} = \left|f(\boldsymbol{q})\right|^2 \tag{3.24}$$

where the incoming neutron flux Φ_{in} is given in units of neutrons per second per unit area.

In the case of the previously mentioned nuclear scattering potential given in equation 3.16 of a sample consisting of N atoms, the differential scattering cross section results in

$$\frac{d\sigma(\boldsymbol{q})}{d\Omega} = \left|\sum_j b_j e^{i\boldsymbol{q}\boldsymbol{r}_j}\right|^2. \tag{3.25}$$

3.3.1 Coherent and Incoherent Scattering

As mentioned before, the scattering length b is an isotope and spin-dependent quantity. In real samples, as it is impossible to know the spin and isotope-state of each nucleus, let alone calculate the differential cross section taking into account this variation, the differential scattering cross section is calculated using the mean value $\overline{b}$ and mean squared value $\overline{b^2}$ of the scattering length defined as

$$\overline{b} = \sum_i p_i b_i, \tag{3.26}$$

$$\overline{b^2} = \sum_i p_i b_i^2 \tag{3.27}$$

with p_i the abundance of the isotope/spin-state with scattering length b_i. This is justified as the number of atoms in a sample is large, and the distribution of the specific isotope and spin states can be assumed to be random. Using this definition and assuming for simplicity that the scattering lengths are real, the differential cross section in equation 3.25 can be rewritten as

$$\frac{d\sigma(\boldsymbol{q})}{d\Omega} = \sum_{jk} \overline{b_j b_k} e^{i\boldsymbol{q}\cdot(\boldsymbol{r}_k - \boldsymbol{r}_j)}, \tag{3.28}$$

where the square modulus has been written out explicitly as the product of one factor times its complex conjugate. Splitting up the sum in $j \neq l$ and $j = k$ this can be rewritten in

$$\frac{d\sigma(\boldsymbol{q})}{d\Omega} = \sum_{j\neq k} \overline{b_j b_k} e^{i\boldsymbol{q}\cdot(\boldsymbol{r}_k - \boldsymbol{r}_j)} + \sum_j \overline{b_j^2} \tag{3.29}$$

$$= \sum_{jk} \overline{b}_j \overline{b}_k e^{i\boldsymbol{q}\cdot(\boldsymbol{r}_k - \boldsymbol{r}_j)} + \sum_j \left(\overline{b_j^2} - \overline{b}_j^2\right) \tag{3.30}$$

$$= \left(\frac{d\sigma(\boldsymbol{q})}{d\Omega}\right)_{coh} + \left(\frac{d\sigma(\boldsymbol{q})}{d\Omega}\right)_{inc}. \tag{3.31}$$

We identify the first term as the *coherent* differential scattering cross section and the second term as the *incoherent* differential scattering cross section. The coherent term stems from the interference of neutrons scattered from different nuclei. In elastic scattering, the coherent scattering term gives access to the interatomic distances and structure of the sample. In inelastic scattering, the coherent term provides information about the system's collective excitations.

The incoherent scattering term is the sum of the intensities of neutrons scattered at different nuclei with no interference from the different wavefunctions. Elastic incoherent scattering is $\boldsymbol{q}$-independent and yields a 'flat' background. Inelastic incoherent scattering is connected to the atomic diffusion.

3.3.2 Total Scattering Cross Section

Integrating the different differential scattering cross sections over the solid angle gives access to the respective contribution in the total scattering cross section $\sigma_{tot,scat}$

$$\sigma_{tot,scat} = \frac{\text{total neutrons scattered per second}}{\Phi_{in}} \tag{3.32}$$

$$= \int d\Omega \left(\frac{d\sigma(\boldsymbol{q})}{d\Omega}\right)_{coh} + \int d\Omega \left(\frac{d\sigma(\boldsymbol{q})}{d\Omega}\right)_{inc} \tag{3.33}$$

$$= \sigma_{coh} + \sigma_{inc} \tag{3.34}$$

The total scattering cross section σ_{tot} represents the effective area of the nucleus as seen by an incoming neutron. It is most commonly measured in barns (1 barn = 10^{-28} m^2) and quantifies the probability that any scattering event will occur independent of the energy and momentum transfer.

3.3.3 Absorption Cross Section

In the previous paragraphs, it was assumed that the imaginary part of the scattering length can be neglected due to a weak probability of absorption processes and simplicity. In reality, and especially in the vicinity of an absorption resonance, this is no longer the case, and the imaginary part gives rise to an absorption cross section σ_{abs} leading to a decrease in the intensity I when passing through a material of thickness l according to the Beer-Lambert law

$$I = I_0 e^{-n\sigma_{abs}l}, \tag{3.35}$$

where n is the number of atoms per unit volume. Therefore, the total interaction cross section of a neutron with a sample reads

$$\sigma_{tot} = \sigma_{coh} + \sigma_{inc} + \sigma_{abs} \tag{3.36}$$

The absorption and incoherent scattering lead to an effective reduced incoming neutron flux. This is usually corrected via a transmission correction to properly normalize the scattering intensity.

3.3.4 Scattering from Large Magnetic Structures in the IMS

This thesis studies magnetic structures in the IMS with sizes in the range from 0.1 μm to tens of micrometers. For scattering from such large structures, a description of the scattering interaction via the sum of point-like Fermi pseudo-potentials is no longer adequate. The exact positions of the individual atoms lose relevance, and it is more instructive to transition to a continuum description via the scattering length density (SLD) $\rho(\boldsymbol{r})$ given as the average scattering length per unit volume. For purely nuclear scattering, the SLD is determined by the average nuclear scattering length inside the sample. For magnetic scattering from vortex structures, the magnetic SLD can be expressed via the flux density $B(\boldsymbol{r})$ according to

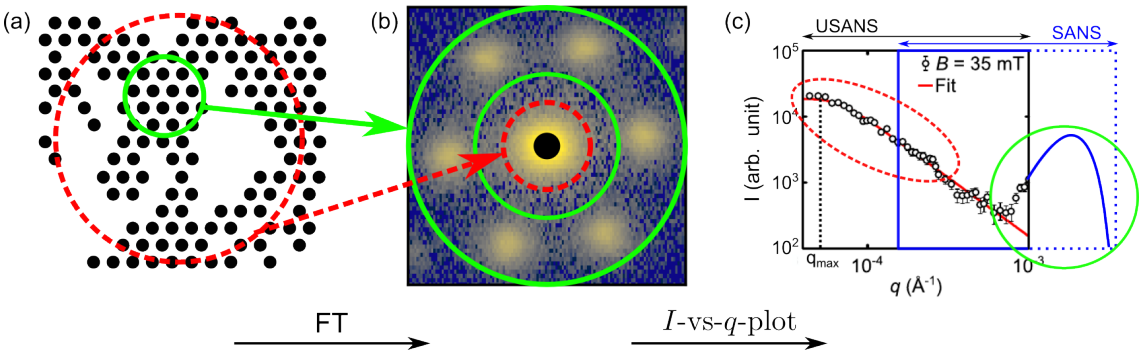

Figure 3.6: Schematic representation of the different scattering contributions in the SANS pattern. (a) The VL within the mixed state has a hexagonal arrangement (green circle), whereas the micrometer-sized IMS domain structure shows no regular structural arrangement (red circle). (b) The SANS pattern, representing a Fourier transform (FT) of the real space structure, contains VL Bragg peaks as well as diffuse power-law scattering in the vicinity of the blacked-out direct beam connected to the IMS domain structure. (c) Ultra small-angle neutron scattering (USANS) allows to resolve the correlation peak q_{max}, whereas SANS only gives access to the VL Bragg peak as well as the high-q tail of the IMS domain scattering. The USANS data in panel (c) is reprinted with permission from [86]. The overall figure is adapted from [18].

$$\rho(\boldsymbol{r}) = \frac{\gamma_N B(\boldsymbol{r})}{4\Phi_0}, \tag{3.37}$$

with the neutron's magnetic moment in nuclear magnetons $\gamma_N = 1.913$ and the magnetic flux quantum $\Phi_0 = h/2e$. The SLD has units of inverse area and is most commonly expressed in Å^{-2}. Using the definition of the SLD, equations 3.23 and 3.24 can be combined and rewritten to

$$\frac{d\sigma(\boldsymbol{q})}{d\Omega} = |f(\boldsymbol{q})|^2 = |FT(\rho(\boldsymbol{r}))|^2 = \left| \int \rho(\boldsymbol{R}) \exp(-i\boldsymbol{q}\cdot\boldsymbol{R}) d\boldsymbol{R} \right|^2, \tag{3.38}$$

where FT stands for the Fourier transform. SANS experiments often times study samples consisting of many similar scattering objects such as micelles, nanoparticles, skyrmions, or vortices. Oftentimes, the differential scattering cross section can then be rewritten using two factors referred to as the form factor $F(\boldsymbol{q})$ and structure factor $S(\boldsymbol{q})$.

The form factor $F(\boldsymbol{q})$ quantifies the scattering pattern from neutrons scattered from a single scattering object, whereas the structure factor $S(\boldsymbol{q})$ is connected to the spatial arrangement of the individual scattering objects with respect to each other. For dilute systems, where the distance between individual scattering objects is much larger than their individual size, $S(\boldsymbol{q})$ can be considered a constant with a value close to unity. Therefore, samples, especially in soft matter studies, are commonly prepared as dilute systems if possible, as this considerably simplifies the modeling and fitting of the scattering pattern.

The IMS can't be considered a dilute system, and we have to take into consideration the impact on the spatial arrangement of the two distinct types of scattering objects, namely the micrometer-sized domain structure consisting of mixed state and Meissner state domains and the individual vortices within the mixed state domains as schematically

depicted in figure 3.6. The domains of variable shape, size, and relative orientation lead to isotropic power-law scattering in the SANS regime and are marked by the red, dashed circle in figure 3.6 (b). For the IMS, a clear separation of the scattering pattern into a structure and form factor is not possible without additional information. In contrast to that, the periodic structure of the VL leads to clear Bragg peak scattering found in between green circles in figure 3.6 (b). The scattering contribution of the VL can be separated into the VL structure factor and the VL form factor. In the following, we first focus on the scattering contribution of the IMS domain structure before we focus on the mathematical description of the VL scattering and the extraction of VL correlation lengths.

3.3.5 Scattering from the IMS Domain Structure

The IMS consists of domains of variable size, shape, and relative orientation. Previously, this two-phase domain structure has been studied via means of ultra small-angle neutron scattering (USANS) [86, 87]. The scattering data showed a broad correlation peak located at small q-values corresponding to length scales of 1-10 μm and a high-q power-law tail as shown in figure 3.6 (c). The USANS scattering data was fitted with a phenomenological model function derived within the framework of spinodal decomposition [91] and given as

$$I(q) = I_{max} \frac{\left(1 + \frac{\gamma_s}{2}\right) \left(\frac{q}{q_{max}}\right)^2}{\frac{\gamma_s}{2} + \left(\frac{q}{q_{max}}\right)^{2+\gamma_s}}, \tag{3.39}$$

where q_{max} and I_{max} are the position and the intensity of the correlation peak, respectively. The parameter γ_s is connected to the dimensionality of the system and describes the power law scattering tail. In this work, we studied the IMS using SANS. The accessible length scales in a conventional SANS setup are limited by the available neutron wavelengths and resolvable scattering angles with a rough upper limit for resolvable structures of approximately one micrometer. Therefore, the correlation peak connected to the domain structure is not resolvable using a SANS instrument. However, the high-q power-law scattering found in the low-q regime of a SANS instrument still contains valuable structural information about the IMS domains as shown in figure 3.6 (c). The IMS power-law scattering can be analyzed using a modification of the well-known Porod-law [92]. Conventionally, the Porod law describes the isotropic scattering of isotropically distributed scattering objects with smooth surfaces and reads

$$I(q) = 2\pi \left(\Delta\rho\right)^2 \frac{1}{q^4} \left.\frac{S}{V}\right|_{spec}. \tag{3.40}$$

Here, $\Delta\rho$ is the scattering length density contrast, and $\left.\frac{S}{V}\right|_{spec}$ is the specific surface area given as the number density multiplied by the surface area of the individual scattering objects. In the case of the IMS, the individual scattering objects are given as the interfaces between the mixed state and Meissner state domains along the field direction. As these surfaces are aligned along the field direction, the condition of isotropically distributed scattering objects is not fulfilled and has to be taken into account to extract the correct specific surface area. We will show in chapter 4 that in the case of a highly aligned domain

structure such as the IMS, $\frac{S}{V}\big|_{spec}$ extracted from the modified Porod law can be connected to the mean repetition length of the domain structure.

3.3.6 Scattering from the Vortex Lattice

In a superconductor filled with a VL, the magnetic flux density used to calculate the magnetic SLD is determined by the VL. The VL in a superconductor can be expressed via the sum of the positions of the individual vortices $L(\boldsymbol{r}) = \sum_i \delta(\boldsymbol{r} - \boldsymbol{r}_i)$. The magnetic flux density $B(\boldsymbol{r})$ is then obtained via a convolution of $L(\boldsymbol{r})$ with the flux density $B_V(\boldsymbol{r})$ generated by each vortex. Thus, the magnetic SLD of a VL reads

$$\rho_{VL} = \frac{\gamma_N}{4\Phi_0} \left(L \star B_V\right)(\boldsymbol{r}), \tag{3.41}$$

where $\star$ is the convolution operator. Inserting equation 3.41 into equation 3.38 and making use of the convolution theorem for Fourier transforms the differential scattering cross section of a VL reads

$$\begin{aligned}
\frac{d\sigma(\boldsymbol{q})}{d\Omega} &= \frac{\gamma_N^2}{16\Phi_0^2} \left|FT(L(\boldsymbol{r}))\right|^2 \left|FT(B_V(\boldsymbol{r}))\right|^2 && (3.42)\\
&= \frac{\gamma_N^2}{16\Phi_0^2} \left|\sum_{R_j} \exp(-i\boldsymbol{q}\cdot\boldsymbol{R}_j)\right|^2 \left|\int B_V(\boldsymbol{r}) \exp(-i\boldsymbol{q}\cdot\boldsymbol{r}) d\boldsymbol{r}\right|^2 && (3.43)\\
&= \frac{\gamma_N^2}{16\Phi_0^2} S(\boldsymbol{q}) \left|F_{VL}(\boldsymbol{q})\right|^2 && (3.44)
\end{aligned}$$

where we identify the Fourier transform of the flux density as the VL form factor $F_{VL}(\boldsymbol{q})$ and the structure factor $S(\boldsymbol{q})$. Assuming perfect periodicity of the VL, the structure factor can be expressed using two-dimensional delta functions $S(\boldsymbol{q}) \propto \sum_{\boldsymbol{G}} \delta(\boldsymbol{q} - \boldsymbol{G})$, where $\boldsymbol{G}$ is a reciprocal lattice vector. In the case of a hexagonal VL, this leads to a hexagonal pattern in reciprocal space that is rotated by 90°, and the reciprocal lattice constant g_{VL} can be connected to the real space lattice constant a_{VL} via

$$g_{VL} = \frac{4\pi}{\sqrt{3} a_{VL}}. \tag{3.45}$$

The position of the Bragg peak scattering can be used to calculate the average internal magnetic field B_{int} according to

$$B_{int} = q_1 q_2 \sin(\alpha) \frac{\Phi_0}{(2\pi)^2}, \tag{3.46}$$

with the Bragg peak positions q_1 and q_2 of two adjacent Bragg peaks, the angle α between them, and the magnetic flux quantum Φ_0. In the case of a perfect hexagon with $q_1 = q_2$ and $\sin(\alpha) = \frac{\sqrt{3}}{2}$ this reduces to $B_{int} = \frac{q^2 \Phi_0 \sqrt{3}}{8\pi^2}$.

The intensity of a Bragg peak is related to the VL form factor $F_{VL}(\boldsymbol{q})$. It contains information about the local magnetic flux density and has been calculated based on different approximations. One of the simplest forms is based on the London model with an additional Gaussian cut-off term taking into account the finite size of the normal core [93, 27]

$$F_{VL}(\boldsymbol{q}) = \frac{B_{int}}{1 + (\lambda q)^2} \exp\left(-c(q\xi)^2\right), \tag{3.47}$$

with the constant c set to values between 0.25 and 2. Conventionally, we find $\lambda q >> 1$ resulting in a form factor proportional to an exponential decay with a constant prefactor of $\frac{\sqrt{3}\Phi_0}{8\pi^2\lambda^2}$ in the case of a perfectly hexagonal lattice. Extracting the VL form factor from the Bragg peak intensity measured in different fields allows one to determine the penetration depth λ_L and superconducting coherence length ξ_{GL} [27].

3.3.7 Rocking Scans

Just like in conventional crystal lattice diffraction experiments, the VL Bragg peaks can only be observed if the Bragg condition is fulfilled. For elastic scattering of perfectly collimated and monochromatic neutrons, the VL has to be rocked onto the Bragg condition to observe a specific Bragg peak. From the Ewald construction schematically depicted in figure 3.7 (a), it also becomes clear that we are not able to resolve the full lattice symmetry simultaneously at a single VL orientation. Instead, the scattering intensity is recorded as a function of the rocking angle around one or two axes perpendicular to the neutron beam. Most commonly, this is referred to as a rocking scan and schematically depicted in figure 3.7 for the rocking angle ω around the vertical y-axis. The full lattice structure is then obtained by summing the individual scattering patterns collected at different rocking angles (see figure 3.7 (b)). Additional information can be obtained by extracting the summed intensity inside a region of interest, e.g., centered on a Bragg peak, as a function of the rocking angle, referred to as a rocking curve. This is schematically depicted in figure 3.7 (c) showing the rocking curve of the left and right Bragg peak as a function of rocking angle ω. The integrated intensity $I(\boldsymbol{q})$ of a Bragg peak at $\boldsymbol{q}$ can then be connected to $F_{VL}(\boldsymbol{q})$ according to the Christen formula [13]

$$I(\boldsymbol{q}) = \left(\frac{\gamma_N \lambda_N}{4\Phi_0}\right)^2 \frac{2\pi}{|\boldsymbol{q}|} |F_{VL}(\boldsymbol{q})|^2 V \eta_{VL}, \tag{3.48}$$

where V is the sample volume and η_{VL} is the mixed state volume fraction, which is 1 in the pure mixed state and 0 in the pure Meissner state. The measured Bragg peak width in the three reciprocal space directions is determined by a combination of the VL size and perfection and the instrumental resolution. In the following, we first focus on the standard SANS data reduction workflow. After that, we turn our attention to extracting the VL correlation lengths from the measured Bragg peak widths.

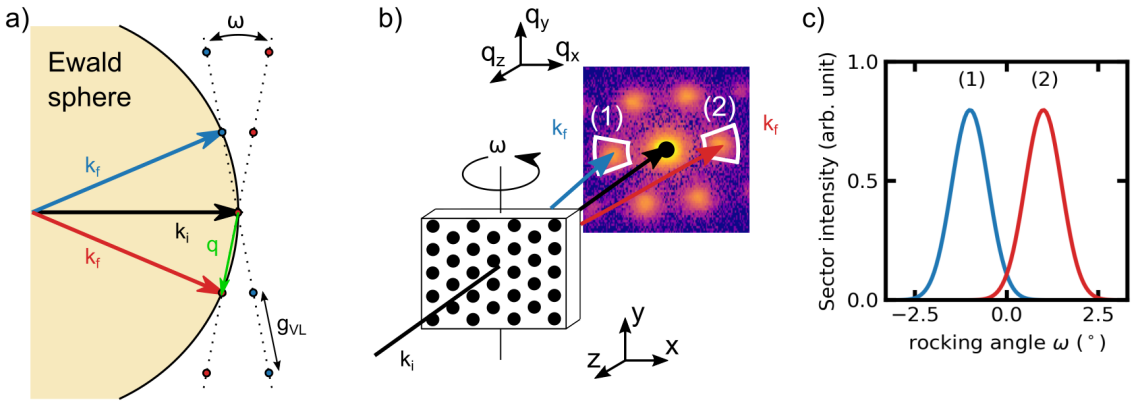

Figure 3.7: Schematics of a rocking scan on the example of two horizontal VL Bragg peaks. (a) Schematic representation of the Ewald construction showing the VL orientation at two different angles ω to fulfill the Bragg condition of two opposing Bragg peaks. (b) Sketch of a rocking scan of the angle ω to fulfill the Bragg condition. (c) Resulting rocking curves of the two sectors indicated in white in panel (b). The figure is adapted from [18]

3.3.8 Data Reduction of IMS SANS Data

Figure 3.7 (b) includes a typical 2D SANS detector image showing the two distinct scattering contributions: (i) the VL inside the mixed state domains results in well-defined Bragg peak scattering and (ii) the IMS domain structure leads to low-q power-law scattering, as discussed above. A typical VL SANS data set consists of 2D SANS detector images recorded at different rocking angles ω and ϕ. After normalization, calibration, background subtraction, and eventual transmission correction, the data set is reduced to 1D scattering curves to perform a quantitative data analysis of the two scattering contributions. In the following, we outline the principal steps of our data reduction workflow, which sets the basis for the data analysis presented later on.

The corrected data I_{corr} is obtained from the data following the standard data reduction scheme using the SANS data analysis software GRASP [94] according to

$$I_{corr} = \frac{1}{T_s} I_{FG} - I_{BCK}, \tag{3.49}$$

with the foreground data I_{FG}, the background data I_{BCK}, and the relative beam attenuation of the sample expressed as a transmission T_s. The relative beam attenuation of the transmitted beam is a result of the magnetic scattering in the superconducting state. The above-presented data correction is strictly speaking only valid for beam attenuation caused by absorption [94], but has been used to background correct neutron scattering data of the IMS [15]. The transmission is calculated for each rocking angle as the ratio of the intensity of the transmitted direct beam of the foreground and background data. In the analysis of quantities where absolute scattering units are not of relevance (e.g., for the analysis of Bragg peak widths), the value of T_s can be manually set to 1. After background correction, I_{corr} only contains the magnetic scattering contribution. Absolute scattering intensities are calculated using the standard SANS data calibration dividing the intensity by the illuminated sample volume, direct beam flux, and the pixel solid angle.

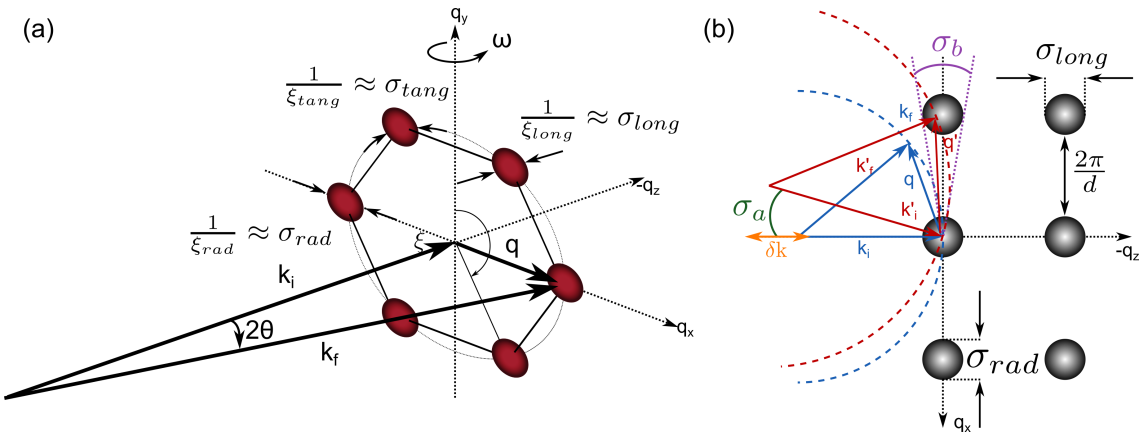

Figure 3.8: (a) Schematic representation of the VL Bragg peak widths in radial, tangential, and longitudinal direction and (b) the influence of the instrumental resolution on the measured Bragg peak width on the example of the longitudinal and radial Bragg peak width.

To further analyze the data, the 2D SANS images at different rocking angles are reduced to 1D scattering curves. For radial curves $I(q)$ and azimuthal curves $I(\xi)$, the intensity inside each pixel is summed over the entire range of rocking angles if not specified differently. The intensity is then represented in polar coordinates as a function of the azimuthal angle ξ and wavevector modulus $q = |\boldsymbol{q}|$. The azimuthal angle ξ is defined on the detector plane in the clockwise direction, with the q_y axis corresponding to 0°. For radial curves, the intensity is integrated over ξ to obtain $I(q)$, whereas for azimuthal curves, the 2D data is integrated over q to obtain $I(\xi)$. The area of integration can be limited using user-defined masks such as sectors around Bragg peaks. For the extraction of rocking curves, the 2D scattering data is not integrated over the range of rocking angles. The intensity inside a region of interest given by a user-defined mask is summed for each rocking angle to obtain the intensity $I(\omega)$ and $I(\phi)$ for rocking scans around the y-axis and x-axis, respectively.

3.3.9 Extracting Vortex Lattice Correlation Lengths

In standard crystal diffraction, finite-sized crystallites contribute to the extracted widths of Bragg peaks, best known as finite-size broadening. This concept is not limited to crystal diffraction but can also be applied to the analysis of SANS Bragg peak scattering from large-scale crystalline structures to quantify the size and perfection of, e.g., nanopore lattices [95], skyrmion lattices [96, 97], or superconducting VL [98, 99, 100]. The volume of the well-ordered lattice structure can be expressed using the three correlation lengths ξ_i inversely related to the intrinsic Bragg peak widths in radial σ_{rad}, tangential σ_{tang}, and longitudinal σ_{long} direction as schematically depicted in figure 3.8 (a). The measured Bragg peak widths are given as a convolution from the different broadening effects due to the finite sample volume, the size and perfection of the well-ordered VL, and the instrumental resolution. This is schematically depicted in figure 3.8 (b) showing the adapted Ewald construction including the different broadening contributions such as a finite beam divergence σ_a, wavelength spread $\frac{\delta\lambda_N}{\lambda_N}$ causing a change in the length of the wavevector δk and finite longitudinal Bragg peak width σ_{long}. The different broadening effects affect the

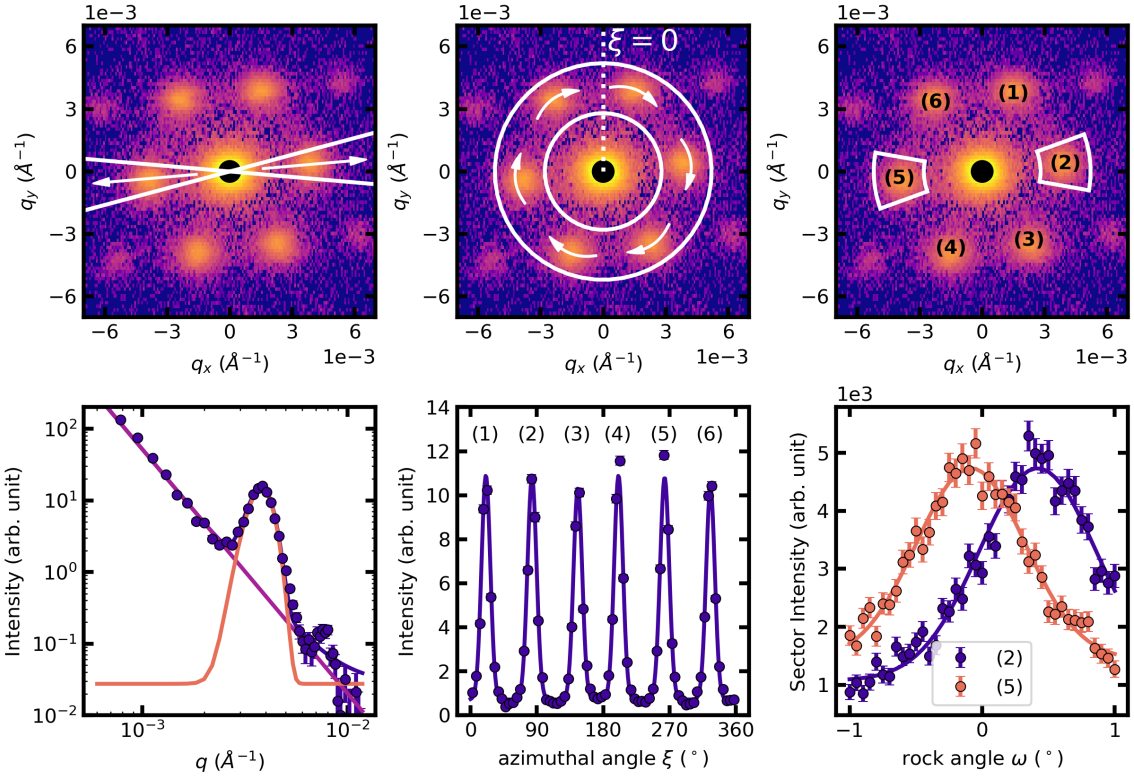

Figure 3.9: Extraction of the measured radial width, tangential width, and rocking curve width from 2D SANS data.

measured Bragg peak widths differently depending on the exact direction of the extracted width.

In our analysis, we follow the method firstly presented by Cubitt *et al.* [99] to calculate the intrinsic Bragg peak widths σ_i in the three reciprocal space directions by taking into account their mutual contributions and the instrumental resolution. The method presented in [99] is based on monochromatic SANS experiments and was recently expanded and adapted by Campillo *et al.* [98] to also cover the treatment of time of flight (TOF) SANS experiments. Here, we briefly summarize the main steps in the calculation of σ_i but refer the reader to [99] and [98] for a more detailed description.

We first define the different parameters affecting the measured Bragg peak widths before we deal with the extraction of the intrinsic Bragg peak width. In a second step, we define the real space correlation lengths calculated from the Bragg peak widths.

The instrumental resolution is determined by the shape of the incoming neutron beam via its finite wavelength spread $\Delta\lambda_N/\lambda_N$ and finite angular spread σ_a.[1] The lattice structure can be characterized by its spread in lattice planes $\delta d/d$, mosaic spread σ_b, and rotational disorder σ_t corresponding to the intrinsic lattice disorder [36, 73, 99].

[1] While not relevant at this point we note that for a parameter or quantity denoted x the symbols σ_x and $\frac{\delta x}{x}$ refer to its rms width and relative rms width, whereas Δx and $\frac{\Delta x}{x}$ are used if the width and relative width correspond to its full width at half maximum (FWHM) value if not stated differently.

In practice, the Bragg peak widths are measured as the radial width W_q, azimuthal width W_φ, and rocking curve width W_ω as depicted in figure 3.9.

W_q is extracted from fits to the radial curves $I(q)$ in reciprocal space units. In Cubitt *et al.* [99], the radial width is expressed in terms of the scattering angle 2θ by converting W_q to $W_{2\theta}$ analogous to

$$2\theta = 2 \arcsin\left(\frac{q\lambda_N}{2\pi}\right). \tag{3.50}$$

$W_{2\theta}$ contains different contributions depending on whether it is extracted from the sum over a rock or only from the frame corresponding to the peak of the rocking curve. We first treat the case of the sum over a rock, where it has the rather simple expression

$$W_{2\theta}^2 = \sigma_a^2 + 4\sigma_c^2. \tag{3.51}$$

σ_c is given as

$$\sigma_c = \theta\sqrt{\left(\frac{\delta\lambda_N}{\lambda_N}\right)^2 + \left(\frac{\delta d}{d}\right)^2}, \tag{3.52}$$

with 2θ given as the scattering angle of the Bragg peak and where we assumed that the wavelength spread usually given as a FWHM can be represented by the rms equivalent $\frac{\delta\lambda}{\lambda}$ of a Gaussian function of the same FWHM.

σ_a is obtained by displacing the beam center on top of the Bragg spot, calculating the radial curve $I(q)$ and extracting the width of the direct beam as shown in figure 3.10. Analogous to the radial Bragg peak width, the width of the direct beam has to be converted to units of 2θ according to equation 3.50. As the FWHM wavelength spread $\frac{\Delta\lambda_N}{\lambda_N} = 10\ \%$ is known, the spread in lattice planes can be directly extracted by solving for $\frac{\delta d}{d}$.

In the case, the radial Bragg peak width is extracted from the scattering data centered on the rocking angle corresponding to the peak of the rocking curve, $W_{2\theta}$ also contains a contribution from the mosaic spread σ_b according to

$$W_{2\theta}^2 = \frac{\sigma_a^2\sigma_c^2 + \sigma_a^2\sigma_b^2 + 4\sigma_b^2\sigma_c^2}{\sigma_a^2 + \sigma_b^2 + \sigma_c^2}. \tag{3.53}$$

Without further knowledge we can't extract $\frac{\delta d}{d}$ from equation 3.53 as it contains the two unknowns $\frac{\delta d}{d}$ and σ_b. Therefore, we need a second equation to solve for the two unknowns.

W_{rock} depends on the different broadening effects according to

$$W_{\text{rock}} = \sigma_a^2 + \sigma_b^2 + \sigma_c^2. \tag{3.54}$$

W_{rock} is extracted as an angular width from the rocking curve as depicted in figure 3.9 and has to be converted to radians. We obtain a system of linear equations consisting of equation 3.54 and equation 3.53 that can be solved for σ_b (in radians) and $\frac{\delta d}{d}$ (unitless). Lastly, the azimuthal width W_{azi} contains information on the rotational lattice perfection according to

$$W_{\text{azi}}^2 = a^2 + \sigma_t^2. \tag{3.55}$$

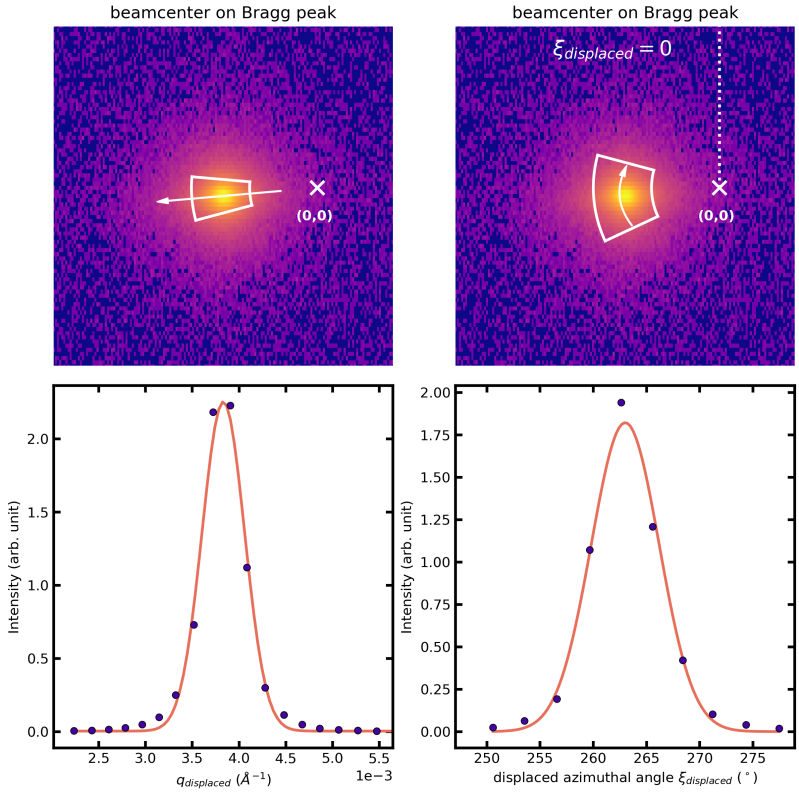

Figure 3.10: Extraction of the direct beam width in the radial and tangential direction from 2D SANS data.

The two contributions of the azimuthal broadening are schematically shown in figure 3.11. The top panel depicts the scenario where the width is entirely determined by the divergence of the direct beam, while the bottom panel illustrates the condition where only the rotational spread of the lattice planes contributes to the azimuthal broadening of the Bragg peak. W_{azi} is extracted as an angular width on the detector plane by performing a fit to the azimuthal curves $I(\varphi)$ as depicted in figure 3.9 and converting it to radians. Analogous to before, the angular spread of the direct beam is extracted by displacing the beam center and extracting its angular width on the detector. The rotational disorder is directly obtained by solving for σ_t.

We obtain the intrinsic lattice parameters $\frac{\delta d}{d}$ (unitless), σ_b (radians), and σ_t (radians). We convert these to the corresponding intrinisic Bragg peak widths σ_{rad}, σ_{long}, and σ_{tang} in reciprocal space units (Å^{-1}) according to

$$\sigma_{rad} = q\frac{\delta d}{d}, \tag{3.56}$$

$$\sigma_{tang} = q\tan(\sigma_t), \tag{3.57}$$

$$\sigma_{long} = q\tan(\sigma_b). \tag{3.58}$$

The intrinsic Bragg peak widths are indirectly proportional to the correlation lengths in real space via the relation $\xi_i = \frac{const}{\sigma_i}$. The relation stems from the Fourier transform of the Bragg peak width in reciprocal space to real space. The definition of the proportionality factor *const* depends on factors such as the peak shape and, in general, is prone to subjectivity as can be seen from the different factors used in literature [73, 72, 95, 27, 16]. As a full discussion of the different definitions is beyond the scope of this thesis, we limit ourselves to some common considerations and justify our choice.

In the case of large-scale crystalline structures completely filling the sample, such as VL or skyrmion lattices, the correlation length is used to quantify the real space length over which the VL is still in phase. The extracted correlation length is often defined as the width of the Fourier-transformed peak, which depends on the peak shape of the Bragg peak in reciprocal space. A Gaussian peak shape in reciprocal space of root mean square (rms) width σ_{rec} results in a Gaussian peak shape in real space width $\sigma_{\text{real}} = 1/\sigma_{\text{rec}}$. Consequently, the correlation lengths are defined as $\xi_i = 1/\sigma_i$ in the case of Gaussian peaks. For Lorentzian-shaped Bragg peaks, the rms width is not defined, but the width is extracted as the full width at half maximum (FWHM). Fourier transforming a Lorentzian function with an FWHM of Δq and a peak position of q_0 results in an exponential function according to

$$L(q) = \frac{1}{\pi}\frac{\frac{\Delta q}{2}}{(q-q_0)^2 - \left(\frac{\Delta q}{2}\right)^2)} \Longrightarrow FT(L(q)) = e^{-\Delta q\pi|x|}. \tag{3.59}$$

The FWHM of the exponential function is then given as $\frac{2ln(2)}{\Delta q\pi}$.

In the case of the IMS, the correlation length is used to quantify the size of the actual size of the individual mixed state domains. Therefore, the broadening is not just caused by, e.g., a finite spread of lattice spacing but results from the convolution of a top-hat

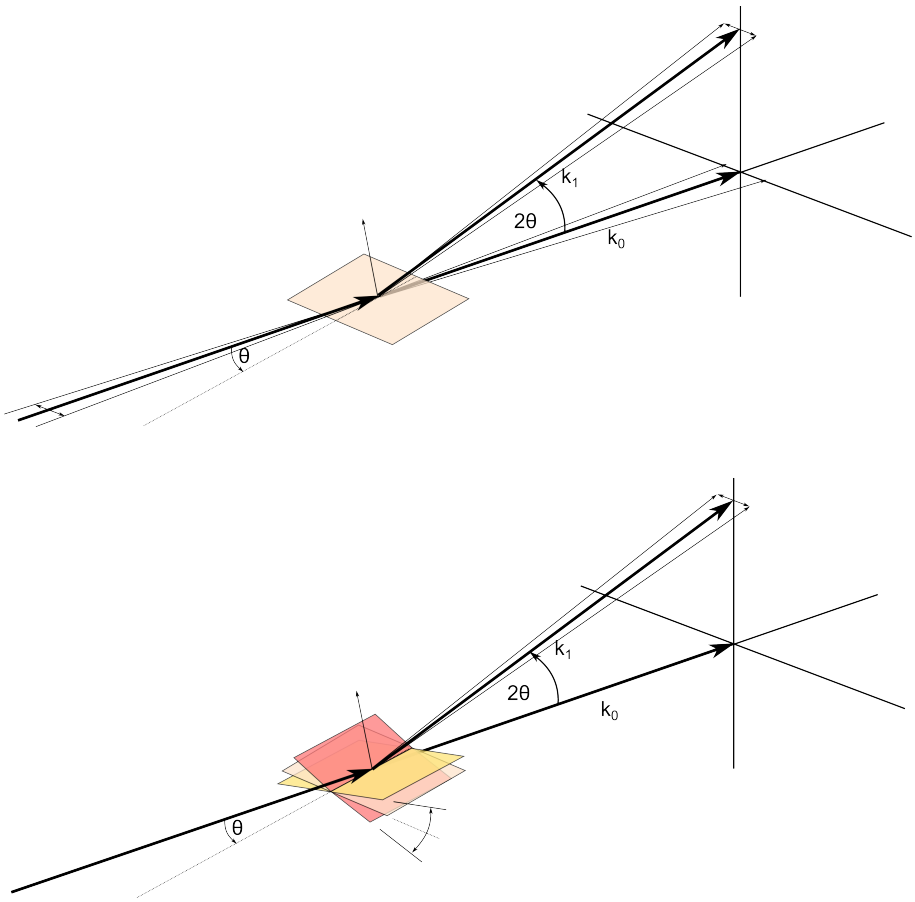

Figure 3.11: Schematics of the beam divergence (top) and the finite lattice perfection (bottom) contribution to the measured tangential width.

Table 3.2: Comparison of different definitions of correlation lengths. For the different methods, we list the definition of the intrinsic width, the FWHM equivalent of the Bragg peak width in reciprocal space Δq, the intrinsic real space correlation length ξ, and the FWHM equivalent of the real space correlation length $\Delta\xi$, expressed in multiples of the intrinsic correlation length ξ_L based on Lorentzian method. $k = 2\sqrt{2ln(2)}$ is a constant factor used to connect the rms width of a Gaussian peak to its FWHM equivalent.

method	intrinsic width	Δq (FWHM)	intrinsic ξ	$\Delta\xi$ (FWHM)
Lorentzian	Δq (FWHM)	Δq	$\frac{2ln(2)}{\Delta q\pi}$ (FWHM)	$\xi_\mathrm{L} = \frac{2ln(2)}{\Delta q\pi}$
Gaussian (G)	σ (rms)	$k\sigma$	$\frac{1}{\sigma}$ (rms)	$\frac{k^2}{\Delta q} = 4\pi\xi_\mathrm{L} \approx 13\xi_\mathrm{L}$
Scherrer (G)	σ (rms)	$k\sigma$	$\frac{2\pi}{\Delta q}$ (FWHM)	$\frac{2\pi}{\Delta q} = \frac{\pi^2}{ln(2)}\xi_\mathrm{L} \approx 14\xi_\mathrm{L}$

function with the VL, which represents the finite size of the mixed state domains. This is analogous to the finite size broadening observed in powder diffraction experiments on small crystallites. The size of the crystallites τ can be extracted using the Scherrer equation [101] according to

$$\tau = \frac{K\lambda}{\Delta(2\theta)\cos(\theta)}, \tag{3.60}$$

with the wavelength of the used radiation λ, K a dimensionless factor close to unity connected to the shape of the crystallite, and the width of the Bragg peak $\Delta(2\theta)$ at the Bragg angle θ expressed as a full width at half maximum in radians. For small angles, where we can use the small angle approximation $q \approx 2\pi 2\theta/\lambda$, this can be rewritten to

$$\tau = \frac{2\pi 2\theta}{q\Delta(2\theta)} = \frac{2\pi}{\Delta(q)}, \tag{3.61}$$

where we have used $K = 1$ due to simplicity. In the last equal sign, we used $\Delta(q)/q = \Delta(2\theta)/2\theta$ with $\Delta(q)$ expressed as a full width at half maximum. As we are dealing with an actual finite size of the mixed state domains, a definition of the correlation length according to equation 3.61 seems more appropriate. It is also used for the analysis of Bragg peak widths outside the field range of the IMS to avoid any discontinuities due to a change in the definition of the correlation length. The presented methods to convert the intrinsic Bragg peak widths to correlation lengths are summarized in table 3.2. It is instructive to compare the different correlation lengths obtained from the different methods, assuming the fits of the Bragg peak width are performed with a fixed FWHM independent of the fit function. We then calculate the FWHM equivalent $\Delta\xi$ of the correlation length in real space. To convert the rms width σ of a Gaussian to its FWHM equivalent Δq we can use the relation $\sigma = k\Delta q$ with the constant factor $k = 2\sqrt{2ln(2)} \approx 2.35$. We then express the FWHM equivalent $\Delta\xi$ of each method to the correlation length ξ_{L} obtained from fitting the peak shape with a Lorentzian fit function. We observe that both the Gaussian and the Scherrer methods yield a similar result if the real space correlation length is expressed as the FWHM equivalent. However, if we compare the Lorentzian method to the Gaussian or Scherrer method, the results differ by more than one order of magnitude. [2]

3.3.10 Neutron Coherence Volume for Lattice Structures

As we are dealing with large-scale structures approaching the resolution limit of SANS, we quickly shed light on the parameters influencing neutron coherence volume. The neutron coherence volume determines the volume over which two neutrons scattered from different points in the sample can yield constructive interference and hence give access to structural information. If neutrons are scattered from structures that are much larger than the neutron coherence volume, the information only gives access to the local features of that structure, such as the surfaces or edges. However, long-range order on length scales that are much larger than the neutron coherence volume can not be resolved. The resulting

[2] We note that in the Scherrer method, as we are calculating the correlation length as an FWHM from the Bragg peak width, also extracted as an FWHM, there's no difference between choosing a Gaussian or Lorentzian fitting function if the FWHM of the Bragg peak is fixed.

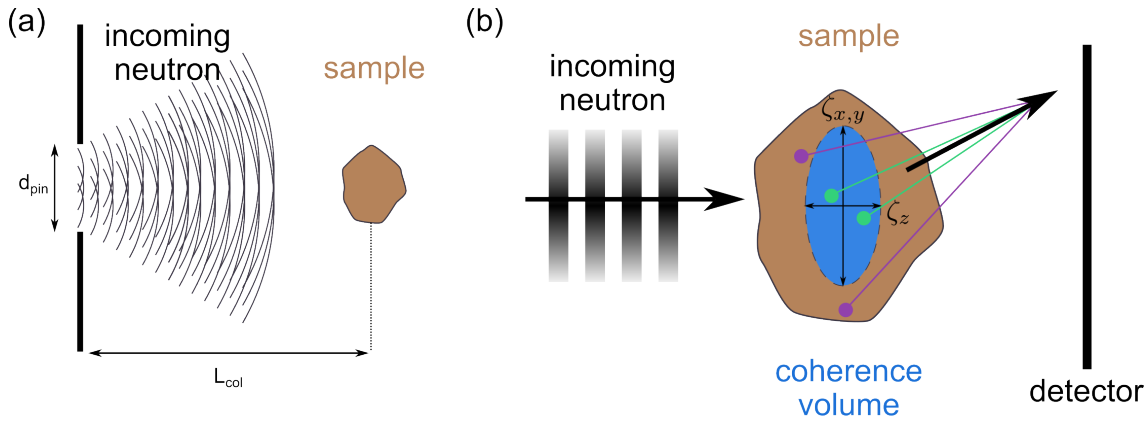

Figure 3.12: (a) Schematic representation of the increasing beam coherence with flight distance L_{col} from an incoherent source of the size d_{pin}. (b) The incoming neutron beam can be modeled as a plane wave with finite coherence volume determined by the coherence length ζ_z along the beam and $\zeta_{x,y}$ orthogonal to the beam. Two neutrons scattered within a volume smaller than the coherence volume can interfere coherently. The entire sample contributes to the incoherent scattering intensity (purple and green arrows). The figure is adapted from [87].

scattering is comparable to the Porod scattering [92]. A schematic representation of the neutron coherence volume is represented in figure 3.12.

The coherence volume can be assumed to have an asymmetric, ellipsoidal shape and can be decomposed in the coherence length orthogonal to the beam direction $\zeta_{x,y}$ and the coherence length along the beam directionζ_z. Conventionally, the coherence length in the direction orthogonal to the incoming neutron beam is determined by the diameter d_{pin} of the pinhole, the length of the collimation L_{col}, and the neutron wavelength λ_N defining the incoming neutron beam according to [102]

$$\zeta_{x,y} = \frac{L_{col}\lambda_N}{\pi d_{pin}}. \tag{3.62}$$

We directly see that $\zeta_{x,y}$ is increasing along the flight path L_{col} of the incoming neutron and changing along its flight path. In the case of an asymmetric pinhole, $\zeta_{x,y}$ is also asymmetric.

The neutron coherence length ζ_z along the incoming neutron beam is constant along the flight path and usually much smaller than $\zeta_{x,y}$. It is connected to the wavelength spread $\Delta\lambda_N/\lambda_N$ and given as [102]

$$\zeta_z = \frac{\lambda_N^2}{\Delta\lambda_N}. \tag{3.63}$$

However, in our case of a highly aligned structure of the VL, the value of ζ_z is not given by equation 3.63. Instead, the neutron coherence length for scattering off from lattice structures is much larger and determined by the interplane spacing d and the wavelength spread [95].

This can straightforwardly be derived using the aforementioned approach, linking the rocking curve width to the VL correlation length, but this time assuming a perfect lattice structure. In the following, we derive the neutron coherence length along the beam direction in the case of large crystalline structures.

For a perfect lattice structure ($\sigma_b = \frac{\delta d}{d} = 0$) with lattice spacing d, we observe Bragg peak scattering at $\theta = \frac{2d}{\lambda_N}$. However, from equation 3.54, we see that the rocking curve width W_{rock} still has a finite width corresponding to the neutron coherence length along the beam direction. This holds as long as the sample dimension along the neutron flight path is larger than the neutron coherence length. Using the above formalism and $\theta = \frac{2d}{\lambda_N}$ we derive for the resolution limited rocking curve width of an ideal lattice

$$W_{res}^2 = \left(\frac{\lambda_N}{2d}\right)^2 \left(\frac{\Delta\lambda_N}{\lambda_N}\right)^2 + \sigma_a^2 \tag{3.64}$$

In analogy, how σ_b is converted to ξ_{long} of the lattice structure, W_{res} can be converted to the neutron coherence length along the beam direction ζ_{long} using $\sigma_{res} = q\tan(W_{res}) \approx qW_{res}$ and $\zeta_{long} = \frac{2\pi}{\sigma_{res}}$. Ignoring the influence of the finite beam divergence, therefore the neutron coherence length ζ_z along the beam direction can be estimated to

$$\zeta_z \approx \frac{2\pi}{qW_{res}} < \frac{2d^2}{\lambda_N}\left(\frac{\lambda_N}{\Delta\lambda_N}\right), \tag{3.65}$$

where the $<$ takes into account neglecting the beam divergence term in the calculation. The derived term of ζ_z is in analogy to the neutron coherence length calculated in [95], but differs by a factor of 2. Nevertheless, it shows that the neutron coherence length along the beam direction in scattering experiments from large crystals is much larger than the neutron coherence length in standard SANS experiments.

3.4 Instrumental Setup

The neutron scattering data presented in this thesis were performed using the small-angle neutron diffractometer D33 situated at the Institut Laue-Langevin and described in detail in [94]. The instrument schematically depicted in figure 3.13 is a typical pinhole SANS instrument with maximum collimation and sample-to-detector flight path of 13 m. The instrument can be grouped into four sections: (i) beam conditioning and neutron optics, including the velocity selector, (ii) the collimation consisting of reflecting neutron guides and absorbing collimation tubes equipped with variable diaphragms of different sizes and shapes, (iii) the sample zone containing the sample and various sample environments such as cryostats and magnets, and (iv) the evacuated detector tank containing the detector installed on a movable trolley with a variable sample-detector distance of up to 13 m.

As in the IMS, we are dealing with structures of spatial size in the range of several 100 nanometers to several tens of micrometers, the instrument was configured to resolve small q-values. This involves long collimation and sample-detector distances close to their maximum lengths combined with large neutron wavelengths as well as small source and sample apertures to separate the transmitted neutron beam from the scattering signal.

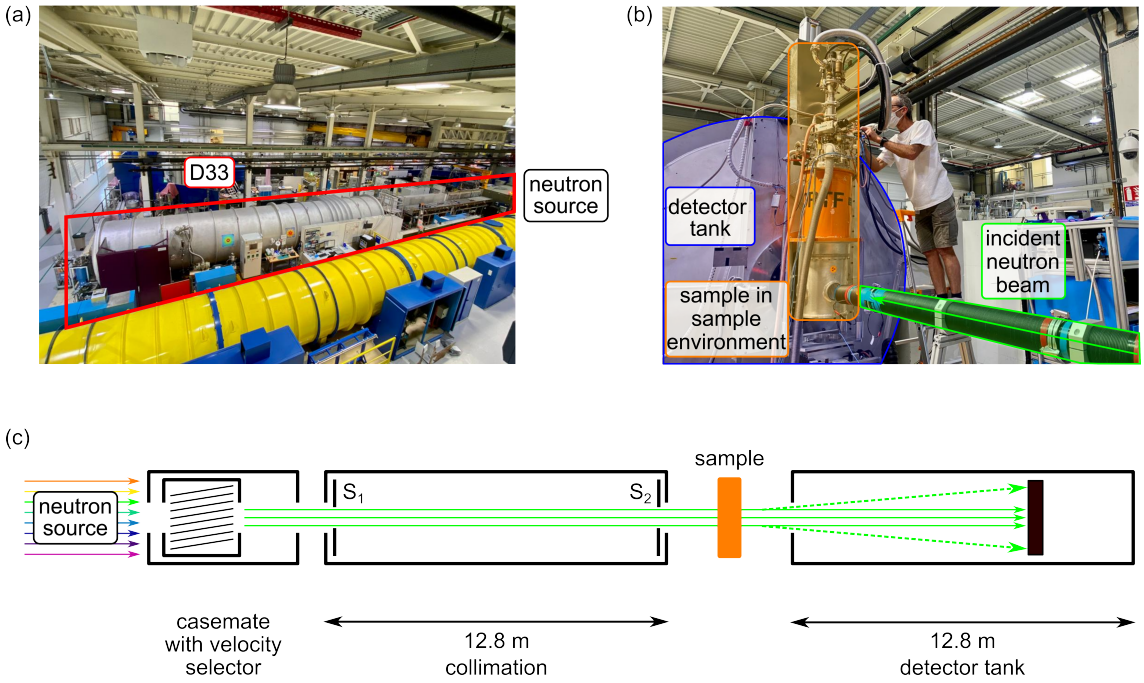

Figure 3.13: Photos and schematic drawing of the SANS instrument D33. (a) Photo of the D33 instrument (framed in red). (b) Detailed view of the instrument sample zone. (c) Schematic depiction of the instrumental setup. The incoming neutrons are monochromatized using a velocity selector. The neutron beam is shaped using neutron-absorbing collimation tubes of adaptable length and diaphragms (S). The 2D position-sensitive detector can be placed at different sample-detector distances of up to 13 m to detect the neutrons scattered by the sample. The figure is reproduced from [18].

The exact instrument settings and the used sample environment varied slightly for the individual neutron beamtimes and are summarized in table 3.4.

3.5 Sample overview

The experiments conducted within the scope of this thesis were conducted using Nb single crystal samples. All samples were cut from the same 'parent' single crystal obtained from Heraeus as samples used previously [16, 17]. While material parameters such as the superconducting transition temperature and the normal state resistance are mostly governed by the bulk properties and therefore determined by the 'parent' single crystal, other properties such as the critical depinning current are sample-specific as they depend on the individual characteristics of the sample, e.g., the sample shape, dimension, and surface treatment. The different samples were cut from the 'parent' crystal to allow measurements to highlight different characteristics of the IMS in the field-temperature-current phase diagram. The sample-specific characteristics of the samples used for the different experiments are summarized in table 3.3.

Previously, a residual resistivity ratio of RRR ≈ 390 [17] was obtained from transport measurements on a smaller sample cut from the same single crystal. Transport measurements using Nb-1, Nb-2, and Nb-4 yielded similar results, showing RRR values of approximately 400. Temperature scans of the AC magnetic susceptibility using our custom-built AC-susceptometer (see chapter 5) yielded a superconducting transition temperature in zero field of $T_c = (9.2 \pm 0.1)$ K determined by the drop in the inductive channel. This agrees well with the literature values of T_c for high purity Nb [103].

Table 3.3: Overview of the single crystal Nb samples. The sample dimensions are given as the three edge lengths. The demagnetizing factor D is obtained by using the formula presented in [104] for rectangular samples. Additional information regarding the cross section shape, sample preparation steps and crystal orientation with respect to the applied field B_{app}, the neutron beam n, and current direction I are given.

name -	l × w × t (mm^3)	cross section –	sample preparation –	D –	axis ∥ B_{app} [hkl]	axis ∥ I [hkl]	axis ∥ n [hkl]
Nb-1	$15 \times 1 \times 0.1$	rectangle	spark cut, polished, etched	0.87	[100]	[010]	[100]
Nb-2	$15 \times 1.4 \times 0.1$	rectangle, beveled edges	spark cut	≈ 0.86	[101]	[010]	[101]
Nb-3	$12 \times 2.8 \times 1$	parallelogram, $\alpha = 45°$	spark cut	≈ 0.63	[101]	-	[101]
Nb-4	$15 \times 1 \times 0.1$	rectangle	spark cut	0.87	[100]	[010]	-

Table 3.4: Overview of the instrument configurations and samples used in the different neutron beamtimes listing the collimation length D_{col}, sample detector distance D_{det}, neutron wavelength λ_N, source aperture d_{source}, sample aperture d_{sample} or $a_x \times a_y$, and the sample environment.

experiment –	sample –	D_{coll} (m)	D_{det} (m)	d_{source} (mm)	d_{sample} (mm)	$a_x \times a_y$ (mm^2)	λ_N (Å)	sample environment –
5-31-2911	Nb-1	12.8	12.8	20	–	5×1.5	14	cryomagnet
5-31-2951	Nb-2	12.8	8.0	10	3	–	14	Orange type cryostate + HTS
5-42-573	Nb-2	12.8	13	10	–	5×1.5	14	Orange type cryostat + HTS
5-42-579	Nb-3	12.8	13	10	–	5×1.5	14	Orange type cryostat + HTS

4 Extracting Extraordinary Lengths Using a Modified Porod Law

The contents of this chapter are published in the Journal of Applied Crystallography as a research paper with the title Pushing the limits of accessible length scales via a modified Porod analysis in small-angle neutron scattering on ordered systems [100]. The figures in this chapter are adapted or reproduced from [100]. The neutron data of this chapter is available on the data platform of the Institut Laue-Langevin [105].

Small angle neutron scattering is routinely used to characterize structures in bulk samples with length scales in the range of 10 - 1000 nm in scientific fields ranging from biology [106], material science [107] to magnetism and superconductivity [108]. The study of larger structures is hampered by the available neutron wavelengths and resolvable scattering angles in a conventional SANS setup, and we find an upper limit of roughly one micrometer. In this chapter, we show how, in the special case of an oriented domain structure, we can circumvent this limitation by using a modification of the well-known Porod law. We employ the method to extract the micrometer-sized domain structure of the intermediate mixed state in niobium.

The Porod law, in its conventional form, relates the isotropic q^{-4} scattering from isotropically distributed scattering objects with smooth surfaces to their specific surface area $\frac{S}{V}\big|_{spec}$ according to

$$I(q) = 2\pi \left(\Delta\rho\right)^2 \frac{1}{q^4} \left.\frac{S}{V}\right|_{spec}, \tag{4.1}$$

which we already introduced in section 3.3 but is included again for convenience. In the case of the IMS or other similar aligned systems, the inverse of $\frac{S}{V}\big|_{spec}$ can be directly linked to the repeat distance $m+d$ of the domain structure. Using this method, we extract length scales of up to 40 μm from SANS data obtained in a conventional SANS setup. In the following, we first give details about the instrumental setup and the scattering geometry in section 4.1. In section 4.2, we then focus on the data reduction and data analysis process with a focus on the extraction of correlation lengths from the Bragg peak scattering and the modified Porod analysis of the low-q power-law scattering of the IMS domain structure. The results of the analysis method are presented in section 4.3, first focusing on the Bragg peak scattering before turning our attention to the low-q IMS scattering. Finally, the results will be discussed further and compared to previous results in section 4.4.

4.1 Experimental Setup

The SANS measurements were performed using the small angle neutron diffractometer D33 at the Institut Laue-Langevin [94], of which a schematic drawing is included in section 3.3. A schematic drawing of the common VL SANS experiment geometry is depicted in figure 4.1 showing the orientation of the sample with its crystallographic orientation,

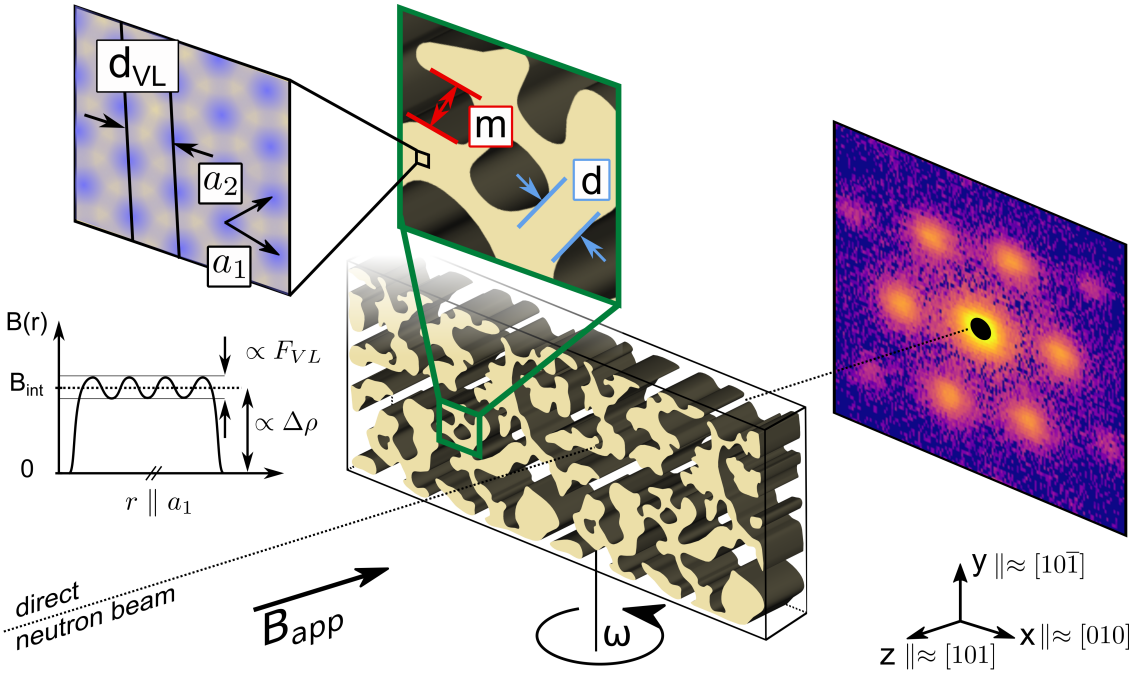

Figure 4.1: Schematic drawing of the scattering geometry. The applied magnetic field *Bapp* is aligned parallel to the incoming neutron beam. The scattered neutrons are recorded using a position-sensitive 2D detector placed behind the sample. The two VL vectors a_i, the interplanar VL distance d_{VL}, the VL domain size d, and the Meissner state domain size m are marked by arrows in the zoomed-in schematics of the insets. A schematic drawing of the magnetic field distribution $B(r)$ along the direction of a_1 is also included. The magnetic scattering length density contrast $\Delta\rho$ is determined by the difference in the magnetic field between mixed state domains (internal magnetic field B_{int}) and Meissner state domains (zero internal field) and connected to the IMS scattering. The VL form factor amplitude F_{VL} connected to the Bragg peak scattering is resulting from the close to sinusoidal field variation inside the mixed state domains.

the direction of the applied magnetic field B_{app} and the coordinate system used in the following.

The prism-shaped Nb single crystal sample Nb-3 was used in the experiments. Details about the sample are summarized in section 3.5 in table 3.3 comparing all the samples studied within the scope of this thesis.

The sample had a [101] crystallographic direction aligned close to parallel to the large sample face surface normal and a [010] crystallographic direction close to parallel to the long sample dimension, respectively, resulting in the orientation as shown in the coordinate system of figure 4.1. The crystallographic directions were confirmed using an X-ray diffractometer prior to the neutron experiments. The sample was positioned in the neutron beam with the long sample dimension close to parallel to the x-axis, and the large sample face aligned perpendicular to the magnetic field, resulting in a large demagnetizing factor and large phase space of the IMS in the field temperature phase diagram. Initially, the magnetic field was aligned parallel to the incoming neutron beam, but the sample environment consisting of the cryostat with the sample inside the magnet could be rotated around the y-axis by an angle ω.

The instrument was configured in a high-resolution setup optimized to resolve small values of the wavevector transfer q. A maximum collimation length of $D_{\mathrm{col}} = 12.8$ m, sample detector distance $D_{\mathrm{det}} = 13$ m and neutron wavelength $\lambda_n = 14$ Å with a full width at half maximum wavelength spread $\Delta\lambda_n/\lambda_n = 10$ % were used. The beam size was determined by a neutron absorbing source aperture of diameter $d_{\mathrm{source}} = 10$ mm and a rectangular neutron absorbing sample aperture of $a_x \times a_y = 5 \times 1.5$ mm^2 illuminating the central part of the sample. This resulted in an effective sample volume in the beam of $V = 5 \times 1.5 \times 1$ mm^3. The applied magnetic field B_{app} and cryogenic environment were supplied via a dry high T_c superconducting magnet in combination with an Orange-type cryostat. If not indicated else, all measurements were performed at $T = 4$ K following a field-cool (FC) measurement procedure from $T = 10$ K and were background corrected using a high-temperature background measured in zero field at $T = 10$ K above the superconducting transition temperate T_c. For each field value B_{app}, the angle ω was scanned in the range of $-1°$ to $1°$ with a step-size of $\Delta\omega = 0.05°$, referred to as a rocking scan.

4.2 SANS Data Analysis

The different length scales found in the IMS call for a careful analysis of the SANS pattern dealing with both the Bragg peak scattering connected to the VL within the mixed state domains and the low-q IMS scattering. The analysis of the Bragg peak scattering, including the extraction of correlation lengths ξ_i from the Bragg peak widths in the three reciprocal space directions and the determination of the internal magnetic field B_{int} from the Bragg peak positions in q and ξ was already dealt with in section 3.3. Here, we focus on the low-q power-law scattering and on how to extract the correct value of $\frac{S}{V}\big|_{spec}$ using a modification of the well-known Porod law. In a second step, we will then show how to connect the specific surface area to the repetition length $m + d$ given as the sum of the average mixed state domain size d and the average size of Meissner state domains m.

Porod Scattering from the IMS Domain Structure

The Porod law in equation 4.1 is derived using the angular average of $I(\boldsymbol{q})$ over all possible directions of the wavevector transfer $\boldsymbol{q}$. In its original form, it is only valid in the case of spherical symmetric scattering objects [109] where the scattering intensity only depends on the wavevector modulus $q = |\boldsymbol{q}|$ and not the direction given by its unit vector $\hat{\boldsymbol{q}}$. The Porod law has been adapted to anisotropic particle systems with smooth boundaries (i.e., with no sharp edges and/or vertices) and strictly convex particles.[3] The resulting scattering intensity was found to show the same q^{-4} power-law behavior [111] as the original Porod law according to

$$I(q\hat{\boldsymbol{q}}) \approx \frac{4\pi^2(\Delta\rho)^2}{q^4} \sum_j \frac{1}{|\kappa_{G,j}(\pm\hat{\boldsymbol{q}})|}, \tag{4.2}$$

where $I(q\hat{\boldsymbol{q}})$ denotes the q-dependent intensity along a fixed direction $\hat{\boldsymbol{q}}$ and $\kappa_{G,j}$ describes the Gaussian curvature of the jth scattering particle. The notation $\kappa_{G,j}(\pm\hat{\boldsymbol{q}})$ stands for the particles curvatures with their surface normal parallel or antiparallel to the unit vector $\hat{\boldsymbol{q}}$ ensuring that only these terms enter in the calculation of the scattering intensity in the direction of $\hat{\boldsymbol{q}}$. The interpretation of equation 4.2 is that for anisotropic particles, the measured intensity is higher for directions where the Gaussian curvature is smaller. This is equivalent to directions where the surface of the particles is close to flat.

The scattering from anisotropic two-phase systems can be expressed in an alternative formulation, closely reflecting the morphology of the IMS. The power-law scattering can be linked to the angular distribution of the surface normals between the two phases in the sample $P((\boldsymbol{n}))$ according to [112]

$$I(q\hat{\boldsymbol{q}}) \approx \frac{8\pi^2}{q^4}(\Delta\rho)^2 \left.\frac{S}{V}\right|_{spec} P(\pm\hat{\boldsymbol{q}}), \tag{4.3}$$

where $P(\pm\hat{\boldsymbol{q}})$ denotes the angular distribution $P(\boldsymbol{n})$ evaluated for directions parallel/antiparallel to $\hat{\boldsymbol{q}}$. The conventional Porod law of equation 4.1 is recovered by inserting the isotropic angular distribution $P(\boldsymbol{n}) = 1/4\pi$ [112]. When the conventional Porod law (see equation 4.1) is compared to the anisotropic case (see equation 4.3) one sees that the correct value of $\left.\frac{S}{V}\right|_{spec}$ can not be obtained when using the conventional Porod law for scattering patterns stemming from anisotropic particles/surface normals.

The scattering system encountered in the IMS is a two-phase domain structure consisting of mixed state and Meissner state domains as schematically depicted in figure 4.1. The domain structure is aligned with its surface normals, given by the interface of the mixed state and Meissner state domains, close to orthogonal to the incoming neutron beam. This leads to a massive overestimation of $\left.\frac{S}{V}\right|_{spec}$ when extracted using equation 4.1. The correct value can only be obtained taking into account $P(\pm\boldsymbol{q})$. The aligned character of the IMS with the surface normals close to orthogonal to the incoming neutron beam simplifies the calculation of $P(\pm\boldsymbol{q})$, which reduces to a simple scaling factor α_{orient}. In the

[3] We note, that taking into consideration the finite pixel size of the detector, the condition of convex particles can be relaxed and the q^{-4} power-law decay is also observed in the presence of particles with non-convex surfaces possibly also including edges, vertices and planar facets [110].

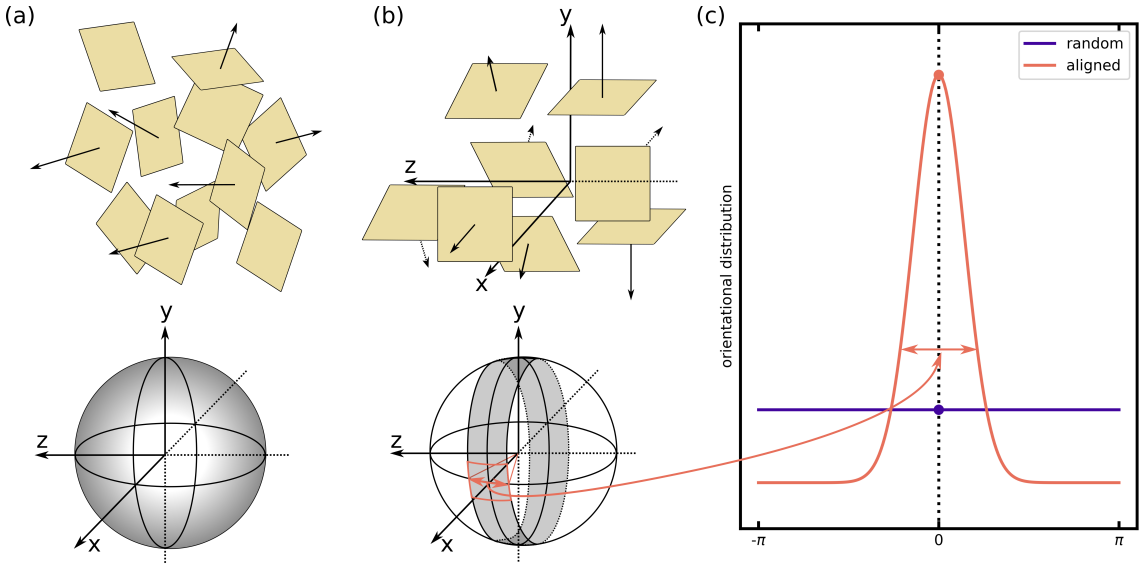

Figure 4.2: Schematic representation of the surface normals in a sample with randomly oriented scattering particles (panel (a)) vs. a sample with aligned surfaces such as the IMS domain structure (panel (b)). Panel (c) illustrates the distribution of the random (purple line) and aligned case (orange line), which, for data that is isotropic on the detector plane, is just a 1D curve. The width of the distribution of the aligned case is estimated by the width of the IMS rocking curves shown in figure 4.3 (d). The correction factor α_{orient} is given as the ratio of the constant value of the flat distribution and the peak value of the aligned distribution marked by a purple and orange solid dot, respectively. Note that the width of the shown distribution is exaggerated for illustrative purposes and not to scale.

following, the rocking curve width of the low-q IMS intensity will be connected to α_{orient} to calculate the corrected specific surface area $\frac{S}{V}\big|_{spec,corr}$. In the second step, $\frac{S}{V}\big|_{spec,corr}$ will be connected to the repetition length $m + d$.

Correction Factor α_{orient} for Highly Oriented Structures

In a simple picture and without loss of generality, the surfaces of the scattering particles in the studied system can be considered as square-shaped platelets. For a random arrangement of particles, the surfaces are isotropically oriented in space as schematically depicted in figure 4.2 (a). The angular distribution of the particles' surfaces is best described and visualized by the surface of the unit sphere. In the aligned case, the vectors describing the surface normals collapse into a single plane orthogonal to the neutron beam as schematically depicted in figure 4.2 (b). Some finite degree of imperfection leads to a finite spread around that plane, which can be quantified using a Gaussian distribution of width σ included in the schematics as the gray ribbon on the unit sphere in figure 4.2 (b).

The conventional Porod law in equation 4.1 represents the scattering intensity for a fixed magnitude of q averaged over all possible directions of $\hat{\boldsymbol{q}}$. The IMS scattering (for zero current) is isotropic on the detector plane. Therefore, the calculation of the scaling factor reduces to a one-dimensional problem. The probability density distribution over 2π is compressed into the small ribbon, which can be quantified by a distribution of width σ as depicted in figure 4.2 (c).

Ignoring the morphology and alignment of the scattering system in the analysis would result in an overestimation of $\frac{S}{V}\big|_{spec}$. Defining the factor α_{orient}, given as the ratio of the isotropic Porod scattering and the aligned case, allows the extraction of the corrected specific surface area $\frac{S}{V}\big|_{spec,corr}$ and is obtained via

$$\left.\frac{S}{V}\right|_{spec,corr} = \alpha_{orient} \left.\frac{S}{V}\right|_{spec}. \tag{4.4}$$

The correction factor α_{orient} is given as the ratio of a normalized uniform distribution on the unit circle ($1/2\pi$) and the peak value of a normalized Gaussian of width σ ($1/\sqrt{2\pi\sigma^2}$) and reads

$$\alpha_{orient} = \frac{\sqrt{2\pi\sigma^2}}{2\pi}. \tag{4.5}$$

In the calculation of α_{orient}, the IMS rocking curve width σ_{IMS} is used as an estimate for the width σ of the distribution of the surface normals. An example is included in figure 4.3 (d) depicting the IMS rocking curves measured in a field of $B_{app} = 20$ mT. The user-defined mask is represented by the white sectors included in figure 4.3 (b). To extract the width, the individual rocking curves are fitted with a Gaussian function drawn as solid lines. The value σ_{IMS} used in the calculation of α_{orient} is obtained as the average of the two rocking curve widths of sectors (1) and (2).

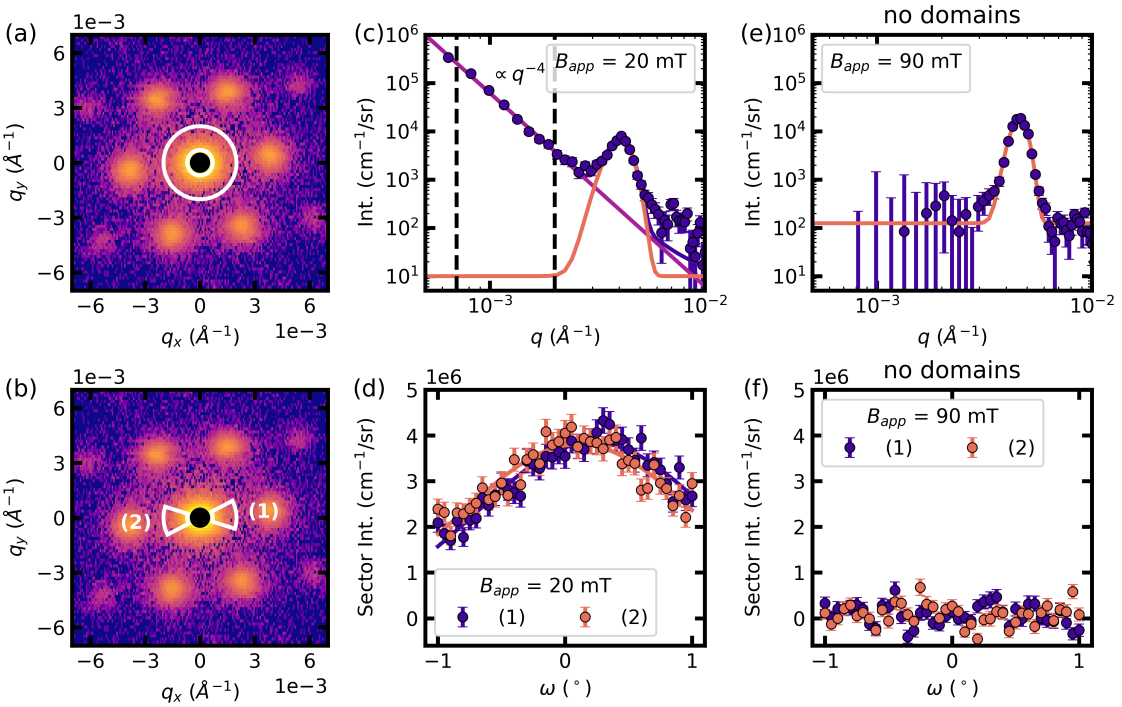

Figure 4.3: Examples of scattering data to extract the low-q scattering connected to the specific surface area of the domain structure: (a,b) 2D detector image of the scattering pattern in B_{app} = 20 mT with the definition of the low-q sector (panel (a)) for the extraction of radial curves $I(q)$ (shown in panel (c)) and the IMS rocking scan sector (panel (b)) for the extraction of the IMS rocking curve (shown in panel (d). (c) The fit of the power law to extract the IMS intensity is constrained to the data in between the dashed vertical lines, (d) the rocking curve of the IMS intensity within the sector shown in panel (b) is fitted with a Gaussian function to extract its width. Equivalent 1D plots for B_{app} = 90 mT where no domain structure is present: No low-q power-law scattering is observed in the radial curve $I(q)$ (panel (e)) and the rocking curve is flat around zero intensity (panel (f)).

Extracting Length Scales from $\frac{S}{V}\big|_{spec,corr}$

After the correction factor α_{orient} was introduced to derive the corrected specific surface area $\frac{S}{V}\big|_{spec,corr}$, it will be shown how to connect $\frac{S}{V}\big|_{spec,corr}$ to a characteristic length scale of the IMS by virtually regrouping and rearranging the domain structure found in the IMS.

$\frac{S}{V}\big|_{spec,corr}$ represents the total interface area A_{tot} between the two phases consisting of the mixed state and Meissner state domains, normalized by the sample volume V. Virtually regrouping and reorienting the domain structure into small areas where the phase boundaries are parallel to each other as schematically depicted in figure 4.4 results in a system of layers of mixed state domains of thickness d separated by Meissner state domains of thickness m. The two length scales represent an average value over all domain thicknesses in the system. This system can be modeled assuming that the individual layers of the mixed state domains are made up of small platelets of area $l_1 \times l_2$ and thickness d separated by a distance given as the thickness m of the Meissner state domains. A schematic drawing of this is depicted in figure 4.4 (b). Using this virtual reorganization, the total number of interfaces can be calculated to

$$N = 2\frac{L_1}{l_1}\frac{L_2}{l_2}\frac{L_3}{m+d}, \tag{4.6}$$

where $L_1 \times L_2 \times L_3 = V$ denote the dimensions and the volume V of the sample. The factor two stems from the fact that each platelet has two surfaces.

Combining equation 4.6 with the definition of the specific surface area allows us to connect $\frac{S}{V}\big|_{spec,corr}$ to the repetition length $m + d$ according to

$$\frac{S}{V}\bigg|_{spec,corr} = \frac{A_{tot}}{V} = \frac{N \cdot l_1 l_2}{V} = 2\frac{L_1}{l_1}\frac{L_2}{l_2}\frac{L_3}{d+m} \cdot \frac{l_1 l_2}{V} = \frac{2}{m+d}. \tag{4.7}$$

The specific surface area in the special case of a two-phase system with alignment along one direction can be interpreted as an inverse length scale. In the special case of the IMS, it can be used to extract the field-dependent repetition length $m + d$.

The last missing link in the extraction of $m + d$ from the low-q power-law scattering using the modified Porod analysis is the determination of the scattering length density contrast $\Delta\rho$ in equation 4.1.

According to equation 3.41 in section 3.3, the scattering length density is proportional to the magnetic flux density $B(\boldsymbol{r})$. The IMS consists of flux-free Meissner state domains with $B = 0$ and mixed state domains with an average internal magnetic field B_{int}. Hence, $\Delta\rho$ can be calculated according to

$$\Delta\rho = \frac{\gamma_N}{4\Phi_0} B_{int}. \tag{4.8}$$

B_{int} is obtained from the Bragg peak positions according to equation 3.46.

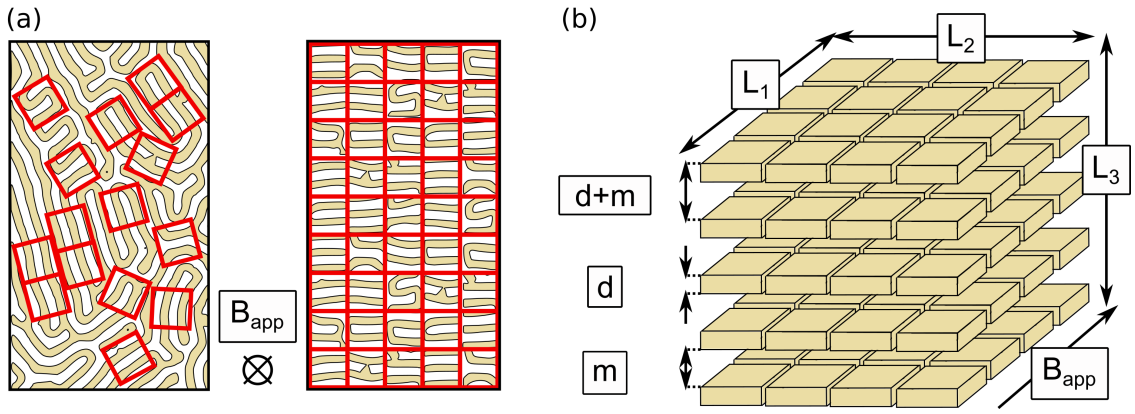

Figure 4.4: Schematics of the virtual reorientation of randomly oriented domains to aligned planes. The direction of the applied magnetic field B_{app} is indicated by the black cross and the black arrow in panels (a) and (b). The superconducting domain structure in panel (a) is adapted from [113].

Inside the IMS, a typical value measured at $T = 4$ K is of $B_{int} = 73$ mT. Inserting this value into equation 4.8 yields $\Delta\rho = 1.7 \times 10^{-7}$ Å^{-2}. This is comparable to the nuclear scattering length density of D_2O, which can be calculated using the SLD calculator on https://www.ncnr.nist.gov/resources/activation/ with a mass density of $\rho_m = 1.11 \frac{\mathrm{g}}{\mathrm{cm}^3}$ for D_2O yielding a value of $\rho_{D2O} = 6.4 \times 10^{-6}$ Å^{-2}.

In practice, $\frac{S}{V}\big|_{spec}$ was obtained by fitting equation 4.1 with $\Delta\rho$ defined by equation 4.8 to the radial curves $I(q)$. The radial curves in absolute units were obtained from the transmission and background corrected scattering pattern at $\omega = 0$ according to the data reduction workflow outlined in section 3.3.8. The range of the fit was constrained to the data in between the white circles shown in figure 4.3 (a) corresponding to the intensity in between the vertical dashed lines shown in figure 4.3 (c). Using the correction factor α_{orient}, $\frac{S}{V}\big|_{spec,corr}$ was then calculated according to equation 4.4.

4.3 Results

In the following section, we present the results of our detailed analysis of the SANS data. We first focus on B_{int} and the VL correlation lengths ξ_i extracted from the VL Bragg peak scattering before we turn our attention to $\frac{S}{V}\big|_{spec,corr}$ and the repetition length $m+d$ obtained from the modified Porod analysis of the low-q power-law scattering stemming from the IMS domain structure.

B_{int} and Vortex Lattice Correlation lengths

Figure 4.5 (a) depicts the local internal field B_{int} as a function of B_{app} in $T = 4$ K. B_{int} was calculated using the positions q_i of two adjacent Bragg peaks and their angle α in between according to equation 3.46. The graph shows two distinct regimes separated by the value $B_{app} = B^* \approx 75$ mT: For high fields, B_{int} decreases linearly with decreasing

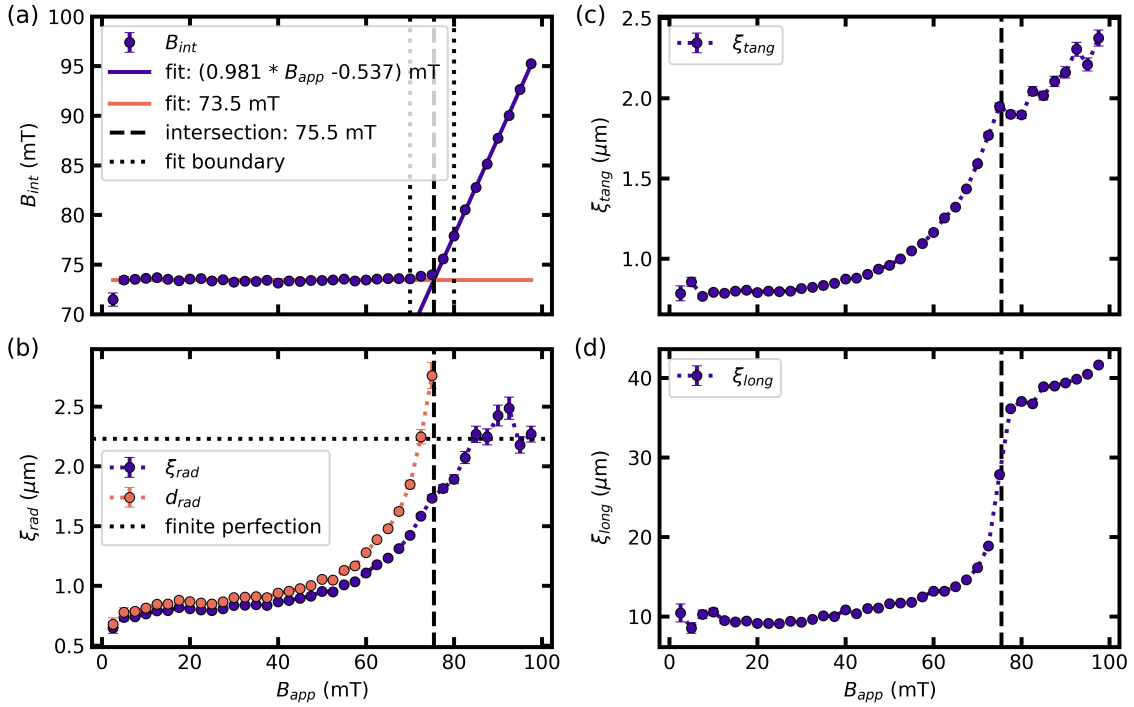

Figure 4.5: (a) Local internal magnetic field B_{int} and (b-d) radial, longitudinal, and tangential correlation length extracted from the Bragg peak width in the three reciprocal space directions. Panel (b) additionally shows the size of mixed state domains d_{rad}.

B_{app} down to the value $B_{app} = B^*$. For lower fields, the extracted value of B_{int} is close to constant ($B_{int} = (73.5 \pm 0.3)$ mT) with a slight downturn for $B_{app} = 2.5$ mT. The two regimes are fitted with a linear function of the form $B_{int} = a \cdot B_{app} + const$, where a is set to $a = 0$ for the low-field regime and *const* denotes a constant that is fitted. The data points found between the two dotted vertical lines close to the transition are excluded from the fits. The fit results are included as a solid orange and purple line for the low-field and high-field regimes, respectively. Equating the two fits allows to determine the line of intersection with a value of $B^* = 75.5$ mT, which is included as a vertical dashed line in all panels of figure 4.5.

The two different regimes can also be traced in the VL correlation lengths extracted from the Bragg peak widths according to the data analysis procedure presented in section 3.3.9. Figures 4.5 (b,c,d) depict the VL correlation ξ_i lengths in the radial, tangential, and longitudinal direction, respectively. We first focus on the correlation lengths ξ_{rad} and ξ_{tang}, that lie in the plane orthogonal to the direction of B_{app}. Again starting at high values of B_{app}, ξ_{rad} is scattered around a finite value of $\xi_{finite} \approx 2.2\mu$m. For lower fields $B_{app} < B^*$, we observe a rapid decrease followed by leveling off to a value of $\xi_{rad} \approx 0.7\mu$m for the B_{app} approaching zero. The observed behavior of ξ_{tang} is very similar except for the high field regime. Instead of a scatter around a close to constant value, ξ_{tang} decreases with decreasing field for $B_{app} > B^*$. For decreasing $B_{app} < B^*$, ξ_{tang} exhibits the same rapid decrease with a leveling off to a constant value of $\xi_{tang} \approx 0.8\mu$m. We now turn our attention to ξ_{long} quantifying the correlation length in the direction parallel to the direction of B_{app} shown in figure 4.5 (d). Over the entire measured field range, the extracted values

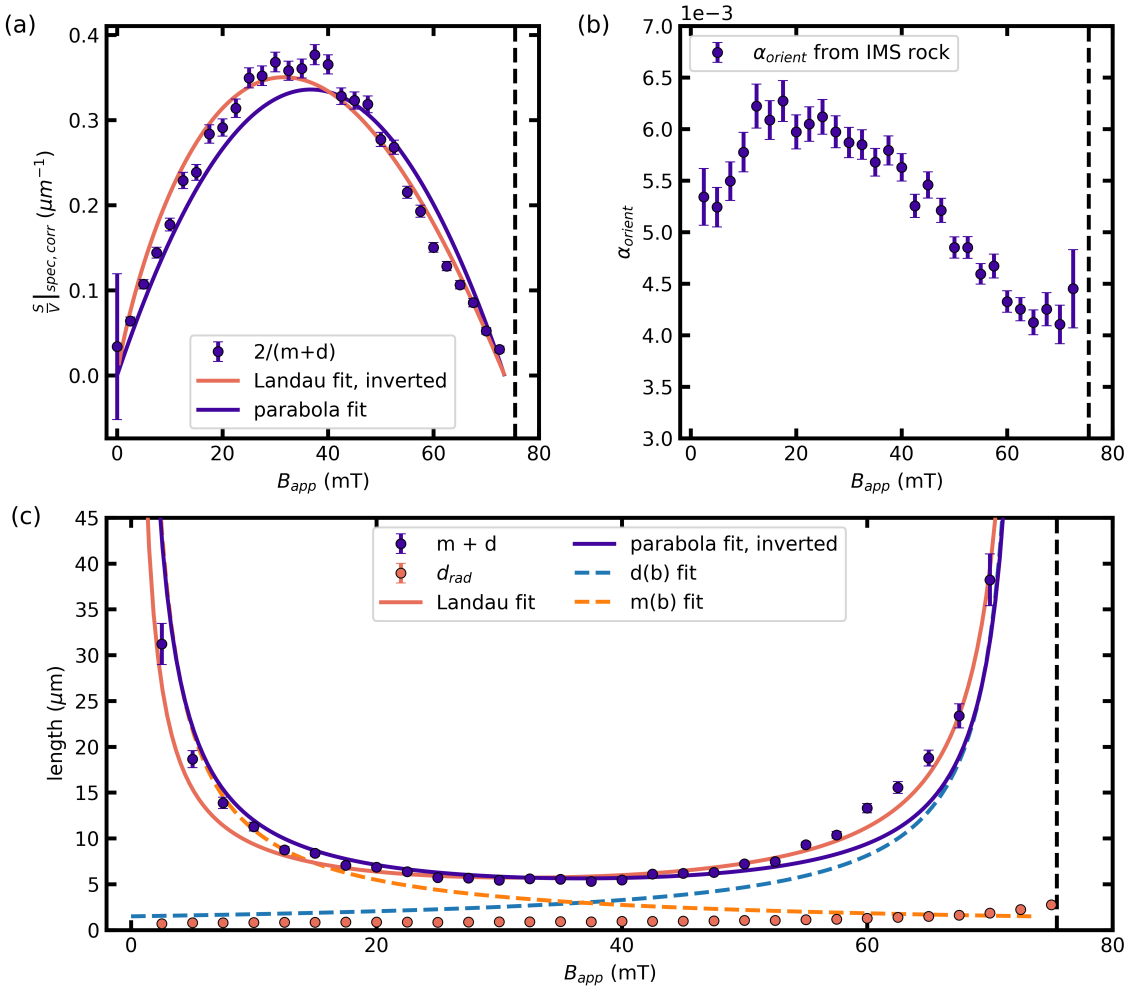

Figure 4.6: Corrected specific surface area $\frac{S}{V}\big|_{spec,corr}$ and repetition length $m+d$. (a) $\frac{S}{V}\big|_{spec,corr}$ extracted from the low-q power-law scattering, taking into account the aligned character of the IMS. (b) Correction factor α_{orient} obtained via equation 4.5, (c) Repetition length $m+d$, radial correlation length ξ_{rad} and d_{rad} extracted from ξ_{rad} according to equation 4.9. The solid lines in panels (a,c) represent fits and their inverted fits to Landau's model of domains (purple) and a parabola (orange) representing a simple model of the functional dependence of the sum of the size of mixed state domains d (blue dotted line) and Meissner state domains m (orange dotted line).

of ξ_{long} are by more than an order of magnitude larger than the respective values of ξ_{rad} or ξ_{tang}. Considering the elongated nature of the vortices along the field direction, this is not surprising. Nevertheless, we observe the same qualitative behavior of a high-field regime with a value close to 40 μm followed by a rapid decrease in the vicinity of B^* and a consequent leveling off to a low-field value of $\xi_{long} \approx 10$ μm when approaching zero field.

Results of the Modified Porod Analysis

We now focus on the low-q IMS scattering and the results of the modified Porod analysis presented in section 4.2 to extract $\frac{S}{V}\big|_{spec,corr}$ to subsequently calculate the repetition length $m + d$.

Figure 4.6 (a) depicts $\frac{S}{V}\big|_{spec,corr}$ calculated from $\frac{S}{V}\big|_{spec}$ and α_{orient} according to equation 4.4. As for fields $B_{app} > B^*$ no IMS scattering is observed (see figure 4.3 (e,f)), the figure only includes data for $B_{app} < B^*$. The correction factor α_{orient} is obtained according to equation 4.5 from the IMS rocking curve width and included in figure 4.6 (b). For field values $B_{app} = 0$ and $B_{app} = 75$ mT with low IMS scattering intensity, the IMS rocking curve width and with it the correction factor had an error larger than 15 %. The corresponding data points are excluded from the following analysis. For the remaining data points, the correction factor is on the order of magnitude of $\approx 5 \cdot 10^{-3}$. Focusing on $\frac{S}{V}\big|_{spec,corr}$: Both, close to the high field range and close to zero field, $\frac{S}{V}\big|_{spec,corr}$ approaches zero. For intermediate field values, $\frac{S}{V}\big|_{spec,corr}$ is close to symmetric around its maximum value of $\frac{S}{V}\big|_{spec} = 0.38\mu\text{m}^{-1}$ at $B \approx 0.5B^*$. The symmetric shape can be fitted with a parabola, which is included as a purple solid line.

We can rearrange equation 4.7 to extract from $\frac{S}{V}\big|_{spec,corr}$ the repetition length $m + d$ shown in figure 4.6 (c). As $m + d$ is essentially the inverse of $\frac{S}{V}\big|_{spec,corr}$, we observe a diverging behavior when approaching both zero field and $B_{app} = B^*$. In between, the shape is close to symmetric and close to flat for field values with a value of the range from 20 mT to 50 mT. We extract a value of $m + d = 5.5$ μm at $B_{app} \approx 0.5B^*$.

4.4 Discussion

After the results have been presented in the previous section, we will give a quick summary of the main findings. In a second step, we will further develop and compare the results to previous works and discuss some limitations in the presented analysis approach.

We observe a constant value of the internal field B_{int} independent of B_{app} below the transition field B^*. This is a well-known hallmark of the IMS and is caused by the non-monotonic vortex interaction leading to a constant inter-vortex distance and, hence, a constant value of B_{int}. The extracted value of $B_{int} \approx 73$ mT agrees well with values obtained in previous studies using samples cut from the same single crystal [17, 16].

The transition to the IMS also manifests itself in the field dependence of the VL correlation lengths: The correlation lengths in the three space directions exhibit a rapid decrease at $B_{app} \approx B^*$, marking the transition to the IMS. The observed behavior of ξ_{rad} and ξ_{tang} are very similar, and their values lay almost on top of each other. This suggests that the mean size of the mixed state domains in the plane orthogonal to B_{app} is independent of the direction. Expressed differently, the mean size of the VL domains is isotropic with respect to the VL orientation, which can also be concluded from the isotropic low-q IMS scattering.

Using the presented modified Porod analysis (see section 4.2), we have extracted the repetition length $m + d$ over the field range of the IMS. Our extracted values are on the same order of magnitude as values obtained from USANS measurements and a detailed analysis of the correlation peak stemming from the IMS domain structure [53]. This indicates that our proposed modified Porod analysis yields physically meaningful results. A similar conclusion can be drawn when comparing $m + d$ from the Porod analysis to the values of the radial correlation length ξ_{rad}. Based on the symmetric shape of $m + d$ a simple assumption is that at $B_{app} \approx 0.5B^*$, the mixed state and Meissner state domains are of similar size $m = d = 0.5(m + d)$ yielding a value of $d \approx 2.8$ μm at $B_{app} = 0.5B^*$. While this is slightly larger than the extracted value of $\xi_{rad} = 0.8$ μm, it is on the same order of magnitude.

In the following, we further develop the results of this section with a detailed focus on VL correlation lengths, domain sizes, and the modified Porod analysis to extract $m + d$.

Average Horizontal Projection of the Mixed State Domain Size d_{rad}

In the field range of the IMS, the VL correlation length ξ_{rad} contains both the finite VL perfection as well as the contribution due to the finite size of the mixed state domains. In the following, we present an attempt to deconvolute the two contributions and remove the contribution of the finite VL perfection from ξ_{rad} to yield the actual size of the mixed state domains. Our observation of a close to constant value of ξ_{rad} for $B_{app} > B^*$ implies that, even within the field range of the pure mixed state, the spatial extent of the well-ordered VL is constrained by an upper limit. Assuming that the finite lattice perfection and the finite size of the VL contribute independently, we can estimate the horizontal projection of the mixed state domain size, d_{rad}, using the following relation

$$d_{rad} = \frac{1}{\sqrt{\frac{1}{\xi_{rad}^2} - \frac{1}{\xi_{finite}^2}}}. \tag{4.9}$$

In equation 4.9, we assumed that the individual contributions of finite size and lattice perfection to the total Bragg peak width combine quadratically. Additionally, we take the average value of the VL perfection in the mixed state, $\xi_{finite} \approx 2.2$ μm, as the maximum achievable VL perfection in the IMS.

The results, displayed in figure 4.5(b) and figure 4.6 (c) as orange dots, show that at low applied fields, the field dependence of d_{rad} mirrors the qualitative behavior of ξ_{rad}. Additionally, as the field increases toward B^*, d_{rad} now shows a more pronounced increase, consistent with an increasing volume fraction of the mixed state domains.

As discussed in section 3.3.9, the exact values of ξ_i and their derived quantities are somewhat subjective, depending on the specific definition of the correlation length. We defined ξ_i as $\xi_i = 2\pi/\mathrm{FWHM}_i = 2\pi/\sigma_i k$, following the analogy with the Scherrer equation, which is commonly used to estimate crystallite sizes in powder diffraction experiments [101].

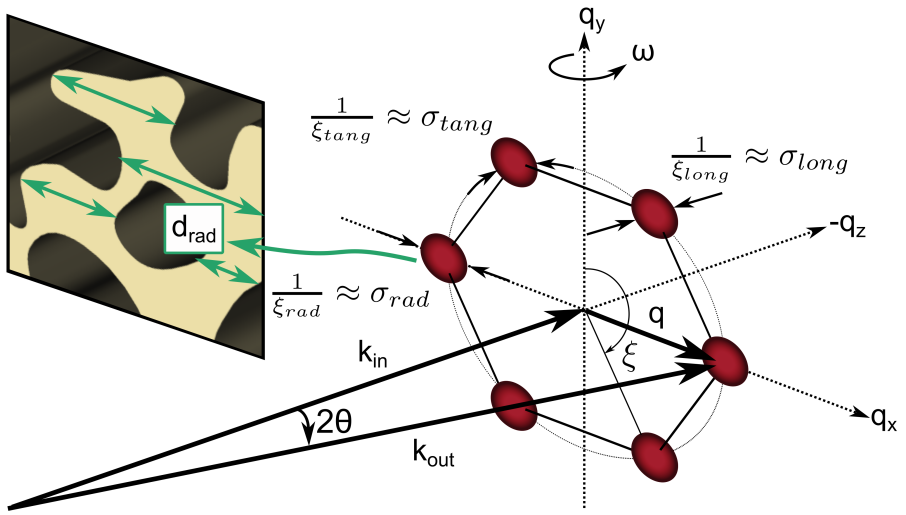

Figure 4.7: Schematic illustration of the projected average length of the mixed state domains d_{rad} in the direction parallel to **q**.

Besides the subjectivity in defining ξ_i, a given mixed state domain may contain multiple crystallites or voids. Additionally, the assumption that the lattice perfection is independent of the mixed state domain size may be overly simplistic, contributing to the uncertainty in the extracted value of d_{rad}. Hence, the derived value of d_{rad} should be regarded as an estimate of the average mixed state domain size rather than a precise value. We also emphasize that the value of d_{rad} represents only the projected average length of the mixed state domains in the direction parallel to **q** as illustrated schematically in figure 4.7.

Field dependence of α_{orient}

The size d of the mixed state domains averaged over all directions is contained in the repetition length, $m + d$, which will be discussed in the following. We now shift our focus to the analysis of the repetition length, domain sizes, and other quantities derived from the modified Porod analysis.

The repetition length, $m + d$, is calculated using the correction factor α_{orient}. We observe a non-trivial field dependence of α_{orient}, which exhibits a slight peak at intermediate fields within the IMS, as shown in figure 4.6 (b). The correction factor is determined by the width of the IMS rocking scan, σ_{IMS}, which reflects the straightness of the domain boundaries along the field direction. A possible explanation for this non-trivial field dependence lies in the interaction between the pinning landscape and the VL as a function of B_{app} influencing the straightness of the mixed state domains. This is schematically illustrated in figure 4.8, which shows the straightness of the mixed state domains along the field direction at three different values of B_{app}.

The interaction between the mixed state domain and the pinning landscape is controlled by the elastic properties of the VL. In analogy to the elastic moduli in crystal lattices, we can define elastic moduli for the VL, which are governed by VL interactions and quantify

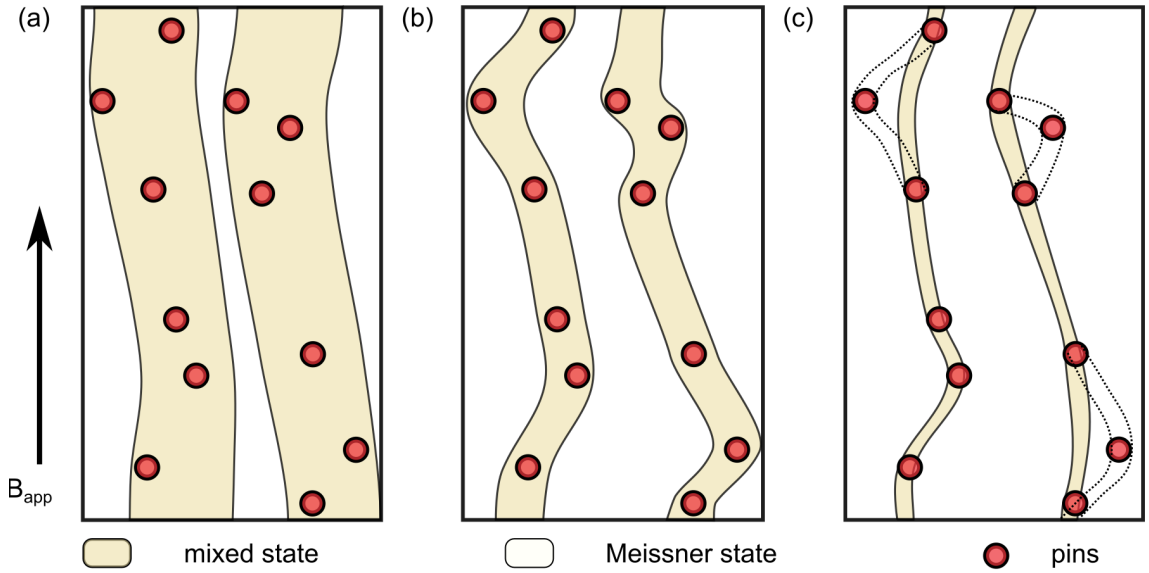

Figure 4.8: Schematic illustration of the field-dependent curvature of mixed state domains along the field direction which is directly related to σ_{IMS} used in the calculation of α_{orient}. (a) For high values of B_{app}, the domains are large, and the influence of the pins on the straightness along the field direction is limited. (b) For intermediate field values, the mixed state domains are increasingly bent due to the interaction with the pinning landscape. This leads to an increase in σ_{IMS} and α_{orient} with decreasing field. (c) For low fields approaching zero, the maximum curvature determined by the elastic moduli prohibits the accommodation of all pins, leading to increased straightness and decreasing values of σ_{IMS} and α_{orient} as compared to intermediate field values. The schematic drawings are exaggerated and not to scale.

the elastic properties of the VL [38]. The elastic moduli impose an upper limit on the curvature of the VL along the field direction as it adjusts to pinning sites. In the IMS, where the spacing between vortices is independent of the applied field, the elastic moduli can be considered close to independent of the value of B_{app}, leading to a maximum possible curvature of the vortices across the entire field range of the IMS.

Therefore, for a given pinning landscape, the curvature of the flux lines along the field direction is determined solely by d, as illustrated schematically in figure 4.8. At high fields, where d is large, the curvature is minimal, and the domain boundaries remain nearly parallel to the field direction. As the field decreases and d becomes smaller, the curvature of the domains increases, leading to larger values of σ_{IMS} and α_{orient}. Below a certain threshold, when d becomes sufficiently small, the flux lines reach their maximum curvature. Consequently, at low fields, the value of σ_{IMS} is higher compared to intermediate fields, which explains the non-trivial field dependence of α_{orient}.

Landau's Theory for Domain Structures

Recently [53], Landau's theory [66] for domain structures in superconductors has been used to model the repetition length of the IMS domain structures

$$m + d = \sqrt{\left(\frac{\delta t}{f_L(b)}\right)}, \tag{4.10}$$

with the thickness of the superconducting sample t, reduced field b, superconducting wall-energy parameter δ and f_L a numerical function of which an explicit formulation, given in [114], was used.[4] For type-I superconductors, δ represents a measure of the superconducting surface energy between normalconducting and superconducting domains. In the IMS, it can be redefined to quantify the interface energy between mixed state and Meissner state domains [53] by connecting it to the cleavage energy or bond energy per unit length U_{bond} of a single bond [86] according to

$$\delta = \frac{2\mu_0\gamma}{B_{int}^2} \approx \frac{2\mu_0 U_{bond}}{B_{int}^2 a_{VL}}. \tag{4.11}$$

γ denotes the surface tension of an interface and shows a slight anisotropy due to the lattice nature of the VL. In a perfect hexagonal VL, this anisotropy was calculated to be 20% repeating with a 6-fold symmetry but can be approximated to be isotropic in a rough estimate [86].

To take into account the demagnetization effects due to the demagnetization factor D, the reduced field b has been adapted by [53] according to

$$b = \frac{B_{app} - (1 - D)B_{c1}}{DB_{int}}. \tag{4.12}$$

[4] We note, that in equation (7) of [53] the square root is missing. We present the correct version with the square root that is in agreement with, e.g., equation 3.23 of [114].

In the case of our samples and experiments, where the IMS covers the entire field range $0 < B_{app} < B^*$ and the Meissner state is not observed, a definition of b according to equation 4.12 is not applicable. We used a simplified version that can capture the entire range of the IMS, which is given by $b = \frac{B_{app}}{B_{int}}$. This choice is justified by the absence of the Meissner state in our measurements following the FC measurement procedure due to macroscopic flux trapping, also observed previously in magnetometry measurements on samples cut from the same single crystal [16]. Using the above modifications of Landau's theory, $m+d$ obtained from our modified Porod analysis can be fitted to extract a value of $\delta = 7.4 \pm 0.1$ Å with the error determined by the uncertainty of the fit. The fit is included as the solid orange line in figure 4.6 (c). Our value of δ compares well to the result of [53] giving a value of $\delta = 13 \pm 2$ Å from measurements on a Nb sample of different shape and purity. The sample thickness is accounted for in equation 4.10. However, it is harder to quantify the influence of the sample purity on δ. Nevertheless, the comparison with our results demonstrates that our analytical approach produces the same order of magnitude.

Simple Model of the field dependence of d and m

Without further assumptions, the individual field dependences of the Meissner length m and mixed state length d can't be extracted from the repetition length $m + d$. Based on the symmetric shape of $m + d$ around $b = 0.5$, we propose a purely phenomenological model that incorporates the asymptotic b-dependence of the Meissner length m and the mixed state length d

$$m(b) = \frac{m_0}{b} \tag{4.13}$$

$$d(b) = \frac{d_0}{1-b}, \tag{4.14}$$

where m_0 and d_0 are constant factors.

As only the length $m + d$ is extracted, a model function is needed to connect our Ansatz from equations 4.13 and 4.14 to $\frac{S}{V}\big|_{spec,corr}$. The symmetric shape of $\frac{S}{V}\big|_{spec,corr}$ closely resembles a parabola of the form

$$\left.\frac{S}{V}\right|_{spec,corr} = \frac{4}{L_0} \cdot b(1-b) = \frac{2}{m+d} \tag{4.15}$$

where L_0 is a constant scaling factor with the dimension of a length following from equation 4.7. Inverting equation 4.15 and inserting the Ansatz from equations 4.13 and 4.14 allows to deduce explicit forms of $m(b)$ and $d(b)$:

$$\frac{L_0}{2}\frac{1}{b(1-b)} = m(b) + d(b) = \frac{m_0}{b} + \frac{d_0}{1-b} \tag{4.16}$$

To fulfill the last equation, the parameters have to be of equal magnitude $m_0 = d_0$. Furthermore we deduce $m_0 = d_0 = 0.5L_0$.

An intuitive explanation can be obtained considering the symmetric shape of $\frac{S}{V}\big|_{spec,corr}$ around $b = B_{app}/B_{int} = 0.5$: for a volume filling fraction of 50% the mixed state length $d(b)$ is equal the Meissner state length $m(b)$.

Putting everything together yields

$$m(b) = \frac{L_0}{2b}, \tag{4.17}$$

$$d(b) = \frac{L_0}{2(1-b)}, \tag{4.18}$$

with L_0, the only free parameter.

Equation 4.15 was fitted to $\frac{S}{V}\big|_{spec,corr}$ to extract L_0. The result is included as the solid purple line in figure 4.6 (a) with the fitted value of $L_0 = (2.9 \pm 0.1)$ μm, where the error is determined by the fit. The functional dependence of m and d can be plotted using the fitted value of L_0 according to equations 4.17 and 4.18 and are plotted as dotted lines in figure 4.6 (c).

In general, there is an overall qualitative agreement of $d(b)$ extracted using the modified Porod analysis and the simple model of m and d and the value of d_{rad} from the Bragg peak width. Both methods yield an increasing mixed state size when approaching B^* and a constant value for low fields. However, an exact quantitative agreement can't be observed, which is partially explained by the fact that the correlation length only yields an estimate of the mixed state domain size, as discussed above.

Limitations of the Analysis Approach

This section concludes with a short discussion of some limitations of the proposed analysis approach. The mixed state domain size is extracted from both the Bragg peak widths as well as the low-q Porod scattering. The analysis of the Porod scattering is based on a simple modification of the well-known Porod law. The modification takes into account the alignment of the scattering surfaces along the direction of the direct beam, introducing a correction factor α_{orient} to extract the correct specific surface area from the slope of the radial curves $I(q)$ in absolute units of the low-q scattering pattern. The repetition length $m + d$ is then connected via simple geometry to the correct specific surface area.

Some uncertainties in the data reduction introduced by the choice of, e.g., the sector size in the calculation of the normalization and calibration constants, such as the transmission, direct beam flux, etc., can impact the extracted specific surface area and hence $m + d$. Other sources that influence the extracted value of $m + d$ are the choice of the correction factor α_{orient} and the simple assumption of a virtual rearrangement in the calculation of $m+d$ from $\frac{S}{V}\big|_{spec,corr}$. Additionally, our Ansatz presented in equations equations 4.17 and 4.18 might be too simplistic to capture the exact field dependence of m and d as suggested by the deviations between the experimental data and the fit shown in figure 4.6. The correlation lengths were extracted from the Bragg peak widths to estimate the contribution of the finite size broadening due to the actual size of the mixed state domains. In the analysis, it was assumed that the finite lattice perfection is independent of the mixed state domain size. Additionally, the Bragg peak width and d_{rad} only contain the projected size of the mixed state domains along the direction of q.

Nevertheless, we are confident that both approaches yield the correct order of magnitude for the extracted length scales. This is supported by the qualitative agreement of the two analysis approaches, the overall agreement with previous works [53], and the agreement with Landa's theory of superconducting domains [66].

4.5 Summary

We presented an analysis approach based on a modification of the well-known Porod law that allows the extension of the accessible length scales in a classical SANS experiment up to 40 μm. Our analysis method is based on the alignment of the two-phase domain structure along the beam direction. The degree of alignment is directly measured through a rocking scan, which is then used to calculate the corrected specific surface area and determine the mean repetition length, $m+d$. In principle, this approach can be applied to any degree of alignment along the beam direction. In the case of isotropically distributed surfaces, this then yields the conventional Porod law. We would like to mention that even in the case of the conventional Porod law, the specific surface area can be connected to an interparticle distance. However, this requires detailed information on the particle dimensions. In the special case of an aligned structure where the domain surfaces extend continuously through the sample, we have shown that the specific surface area is directly related to the mean intersurface distance.

The analysis approach is applied to the two-phase domain structure found in the IMS, which consists of mixed state and Meissner state domains. The domain boundaries between the mixed state and Meissner state domains are aligned along the direction of the incoming neutron beam. Using the presented analysis approach, we extract the repetition length $m + d$ over the entire field range. Our results agree with previous attempts to derive this length scale from USANS [53], Landau's theory of superconducting domains [66], and with the method of extracting correlation lengths from Bragg peak widths [99, 95, 98] from which the finite size of the VL domains can be extracted.

The overall agreement highlights the effectiveness of our analysis approach in extending the accessible lengths scales from 1 μm by almost two orders of magnitude to up to 40 μm using a conventional SANS setup without compromising the experiment by long counting times. Our study serves as a proof-of-concept for applying this technique to other systems that exhibit alignment along the beam direction with continuous surfaces extending throughout the sample.

5 AC Susceptibility and Transport Measurements of the Vortex Matter in Nb

The contents of this chapter are currently prepared for publication.

Usually, among the first measurements conducted on a newly discovered superconductor are AC susceptibility measurements and electrical transport measurements. These methods give access to the sample's magnetic and electrical properties and are usually crucial to establish whether a material is indeed a superconductor or just a fraud, as the recent claims of near-ambient superconductivity in N-doped lutetium hydride [33, 34, 115].

AC susceptibility is also a standard tool for constructing phase diagrams of magnetic samples and can be used to verify the studied point in phase space at specific experimental parameters such as temperature and magnetic field. During neutron experiments, it is essential to precisely know the necessary experimental parameters to sit within the phase-space corresponding to the state of interest, for example, the small skyrmion pocket in the chiral magnet MnSi [97]. A false calibration of the cryomagnets magnetic field or sample thermometer can lead to many hours of lost beamtime to find these parameters before any meaningful measurements are conducted. Motivated by this, we have implemented a custom-built AC susceptometer into an SANS cryomagnet that allows for *in-situ* measurements of AC susceptibility during neutron measurements. At the same time, the system was designed to also allow for simultaneous transport measurements. This way, we were able to characterize our samples in offline characterization measurements without neutrons and prepare for upcoming neutron beamtimes. Furthermore, our measurements revealed a subtle feature in the AC susceptibility and voltage response in current scans corresponding to the onset of the IMS field range. This is remarkable as no such feature is observed in temperature scans of the magnetization or the AC susceptibility.

In the following, we present the experimental setup and design of the AC susceptometer and transport measurement setup in section 5.1. We then show the results from our combined AC susceptibility and transport measurement study on superconducting vortex matter in section 5.2, first focusing on temperature scans with zero current before turning to the measurement with applied current. The results are discussed in section 5.3 comparing it to recent works studying the effect of vortex clustering and pinning in superconductors. The chapter is concluded in section 5.4 summarizing the main results of our lab-based characterization of the magnetic and electronic properties of vortex matter in the intertype superconductor niobium.

5.1 Experimental Setup

The measurements were performed using a combined transport measurement and AC susceptibility setup, consisting of a custom-built AC susceptometer mounted inside a cryomagnet with a transport measurement option. The setup made use of the 8T horizontal SANS cryomagnet of the ILL (alias "Blue Charly") to also allow the setup to be used during a neutron beamtime. The reduced sample space with a diameter of $d = 20$ mm and the need to minimize parasitic background scattering from the susceptometer in neutron

experiments were significant constraints leading to a non-standard AC susceptometer design. A photo and a schematic drawing of the custom-built AC susceptometer are depicted in figure 5.1 showing the driving coil (marked in blue), pick-up coil (marked in red), the orientation of the sample, the driving field B_{AC}, static magnetic field B_{app} and current direction I. In the chosen coil geometry, incoming and scattered neutrons do not pass through any additional material of the susceptometer, therefore minimizing the scattering background. The pick-up coils consist of two identical, counter-wound coils connected in series. This way, signals originating from the AC driving field or other external sources are minimized, and the measured voltage of the pick-up coils is dominated by the magnetic response of the sample. An additional DC magnetic field co-linear to the AC driving field is provided by the SANS cryomagnet. In standard AC susceptibility measurements, the sample is placed at the center of one of the pick-up coils.

In our measurements, given the sample dimensions ($15 \times 1 \times 0.1$ mm^3) and the constraint that the static field is applied parallel to the normal vector of the large sample face, the sample was positioned on top of the bottom pick-up coil. This way, the current was applied orthogonal to the applied AC driving field and the DC magnetic field. To provide stability, the sample was glued to a small silicon plate. As previously [17], the sample stick was equipped with normal-conducting copper current leads in the upper part transitioning to superconducting NbSn current leads spot welded to the sample in the lower part to reduce the effect of ohmic heating due to the applied current. Thin copper voltage leads were connected to the sample using silver conducting paint with a distance between the voltage contacts of $d \approx 5$ mm. Due to the geometric constraints of the cryostat, the superconducting current leads partially crossed the susceptometer. Therefore, they provided an additional magnetic background. However, the background showed no apparent temperature and field dependence in the scanned field and temperature ranges. It was treated as a background signal that was measured above the transition temperature of our sample and subsequently subtracted. The induced voltage of the pick-up coil was measured using a dual-phase lock-in amplifier of the type SR830 from Stanford Research Instruments. The built-in frequency generator of the SR830 was used both as the input signal for the transconductance amplifier (Model 1620A Ballantine Laboratories) of the driving coil and as the reference signal to detect the in-phase and out-of-phase voltage signal of the induced voltage signal. A programmable DC power supply of the type Genesys 60-55 from TDK Lambda acted as the DC current source for the transport measurements. The sample voltage was detected using a Keithley Model 2701 digital multimeter. The setup was installed on the SANS diffractometer D22 at the Institut Laue-Langevin, which made use of the ILL sample environment and instrument control software nomad.

We performed two types of parameter scans: (i) temperature scans and (ii) current scans. For current scans, Helium was allowed to condense in the sample space, completely covering the sample to efficiently take away heat created by the applied current. All current scans were performed after field cooling (FC) the sample in the applied field from $T = 10$ K above its transition temperature to $T = 4$ K. Temperature stability of $\Delta T = \pm 0.01$ K during each current scan was reached by carefully adapting the setpoint temperature as a function of current to counteract heat radiating from the normal conducting wires in the upper part of the sample stick to the sample position. In order to minimize the time and helium consumption for each field change, we installed a small resistor in the vicinity of the sample. This way, the heat needed to warm up the sample above the

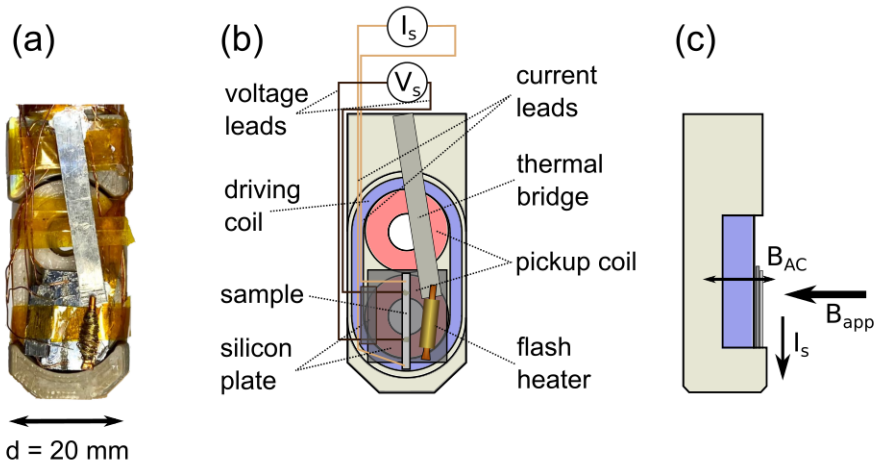

Figure 5.1: Custom-built AC susceptometer with mounted Nb strip sample: (a) Photo of the susceptometer. (b) Schematic drawing of the susceptometer setup with labels of the individual components. (c) Side-view of the susceptometer indicating the direction of the driving field B_{AC}, the static field B_{app} of the cryomagnet, and the current direction.

transition temperature could be applied in proximity to the sample position as opposed to completely warming up the entire sample space via the standard heater located close to the heat exchanger.

As the susceptometer holder was made from plastic, there was a reduced thermal connection of the sample to the sample thermometer positioned just above the susceptometer as compared to standard sample holders made from, e.g., copper. To increase the thermal connection, the silicon plate was thermally connected to the sample thermometer via a small aluminum strip acting as a thermal heat bridge. The amplitude of the drive field and the frequency were set to $B_{ac} \approx 1$ mT and $f = 28.26$ Hz at the beginning of the experiment which resulted in a good signal-to-noise ratio. If not specified otherwise, these values stayed fixed for all experiments. Measurements were performed using stepped sweeps with a variable recording time of $\Delta t = 120 - 180$ s per parameter step. The individual scans were then extracted after the measurement using a Python script to determine the mean value and standard deviation of each recorded parameter during a parameter step. Examples of raw data and further details about the data reduction and the analysis of the AC susceptibility signal are included in the appendix in section A.1.

We used the thin strip-shaped Nb single crystal sample Nb-4 in this study. The sample was cut by spark erosion from the same single crystal used in previous neutron scattering studies [16, 17]. The transition temperature was determined to be $T_c = 9.2$ K with a transition width of $\Delta T = 0.1$ K from AC susceptibility measurements with $B_{app} = 0$ mT using our custom-built setup. The corresponding data is included in figure 5.2 in the results section of this chapter. For more details on the sample, we refer the reader to section 3.5.

5.2 Results

We conducted a systematic study of the magnetic and electrical response of Nb-4 as a function of temperature, field, and current. We first focus on the magnetic response in AC susceptibility measurements in zero current before we turn our attention to combined AC susceptibility and transport measurements in different applied fields.

Temperature Scans in Constant B_{app}

Figure 5.2 depicts $\chi'(T)$ and $\chi''(T)$ for different applied magnetic fields B_{app} in field-cooled (FC, marked by solid circles) temperature scans and the subsequent measurement during field-heating (FH, marked by crosses). There is no observable difference between FC and FH measurements, except for the measurements at 0 mT, where we observe a small peak in χ'' for the FC measurement, whereas the FH measurement stays close to zero over the entire temperature range. The small peak is most likely connected to some remanent magnetic field due to the earth's magnetic field expelled by the superconductor during field cooling. As there is no observable difference in the signal, we don't distinguish between FC and FH measurements in the following description. The temperature dependence of the data measured in different fields is qualitatively similar. At high temperatures, both χ' and χ'' are close to zero. With decreasing temperature, we observe a sharp drop for χ' and a leveling off to a constant value of χ'' for lower temperatures. At the same time, χ'' exhibits a peak at the temperature corresponding to the temperature of the steepest decrease in χ'. For lower temperatures, χ'' approaches zero. The temperature of the onset of the drop in χ' and the peak position of χ'' decreases with increasing B_{app}. The width of the decrease in χ' and the peak width of χ'' increases with increasing B_{app}

Current Scans in Constant B_{app}

Figure 5.3 depicts current scans in selected values of B_{app} covering both the field range of the IMS and the pure mixed state, as well as the current scan in zero applied field. Shown is the DC sample voltage (panel (a)) and the AC susceptometer signal χ' (panel (b)) and χ'' (panel (c)) as a function of current. The background and phase-corrected AC susceptometer signal, as well as the voltage, were obtained according to the data reduction procedure presented in section A.1. The horizontal line at $B_{app} \approx 75$ mT in the color bar on the right-hand side marks the transition from the conventional mixed state to the IMS measured by SANS. The voltage critical depinning current I_{cV} as well as the susceptibility critical depinning current $I_{c\chi'}$ are extracted according to the procedure presented in A.1 and included as vertical dashed and dotted lines, respectively.

We first focus on the DC voltage response shown in figure 5.3 (a). We observe the characteristic I-V curves of a superconducting sample in values of B_{app}. For low currents up to the critical depinning current I_{cV}, the measurements show no measurable voltage. For $I > I_{cV}$, the voltage response appears close to linear (Ohmic), with a slope that is increasing with increasing B_{app} consistent with a flux flow resistance being proportional to B_{int}. In the vicinity of I_{cV}, we observe a slight curvature that is more pronounced for

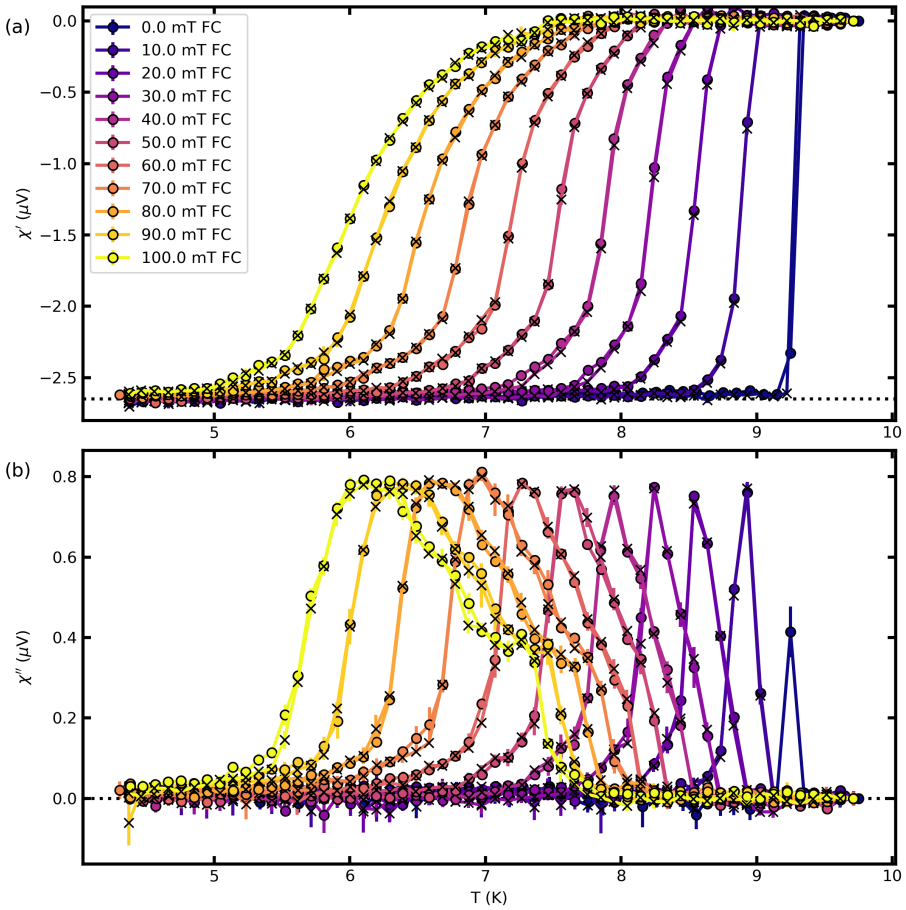

Figure 5.2: χ' and χ'' in FC (marked by solid circles) and FH (marked by crosses) temperature scans for different values of the applied magnetic field B_{app}. The solid lines are a guide to the eyes.

lower applied fields. The extracted values of I_{cV} increase with increasing B_{app}. For zero applied field, no voltage was measured over the entire current range.

We now turn our attention to the AC susceptometer signal. The qualitative shape of the AC susceptibility signal is similar to the shape observed in a temperature scan, showing a drop in the inductive channel χ' and a peak in the resistive channel χ''. In analogy to I_{cV}, we defined $I_{c\chi'}$ as the current where χ' significantly exceeds the zero-current noise background (details in A.1). We observe a negative value of χ'' for low currents below $I_{c\chi'}$. After the sharp rise, χ' approaches a constant value close to 0.

χ'' exhibits a close-to-constant value for both low currents and high currents. A peak can be observed at intermediate currents in the vicinity of I_{cV}. For zero applied field, both χ' and χ'' are close to constant with a slight downward or upward trend, respectively, with increasing current.

More data from measurements for additional values of B_{app} are included in figure 5.4 to point to some trends and additional features that are not seen in figure 5.3 showing only a small selection of measured fields. The different panels depict again the DC voltage response and the AC susceptometer signal as a function of current. The color bar on the right indicates the color of the markers corresponding to the data measured in B_{app}. We now focus on the additional features and trends.

The DC voltage data shows a slight kink in the I-V-curves for B_{app} in the range of 75 mT to 110 mT at currents well above I_{cV}. In general, the curvature in the vicinity of I_{cV} appears more pronounced for decreasing field. In the AC susceptibility signal, we observe several trends when considering the extended field range. χ' for low currents $I > I_{c\chi'}$ in $B_{app} >$ 130 mT exhibits a slightly smaller drop to negative values as the corresponding low current values at lower fields. Similarly, χ'' exhibits a larger, positive value for $B_{app} > 130$ mT at low currents. The high current value of χ'' for these fields is smaller than the low current value and negative. This is in contrast to the data measured in $B_{app} < 130$ mT, where the low current value of χ'' is smaller or equal to the high current value. Additionally, the peak height of χ'' is higher for high fields and decreases with decreasing field in the field range of 180 mT to approximately 90 mT.

Interestingly, we observe a changing behavior in the AC susceptibility signal for fields in the vicinity of $B_{app} \approx 75$ mT, the field which marks the transition between the IMS and the conventional mixed state: χ' exhibits a peak in the high current value at $B_{app} \approx 75$ mT. This is accompanied by an increase in the high current value of χ'' in the vicinity of $B_{app} \approx 75$ mT.

To further explore the DC voltage response as a function of applied current, we computed the differential resistance for a selection of fields covering the entire range of probed fields shown in figure 5.5. Figure 5.5 (a) includes the sample voltage and figure 5.5 (b) shows the differential resistance $\Delta V/\Delta I$. The color bar on the right indicates the color of the markers corresponding to the data measured in B_{app}. The differential resistance is calculated using two consecutive data points smoothed using a moving average filter of window size 5. The general trend of a higher slope of the I-V-curves in higher fields is reflected in higher values of the differential resistance. While the voltage response in panel (a) appears to be linear, the differential resistance in panel (b) reveals that over the probed current range no linear

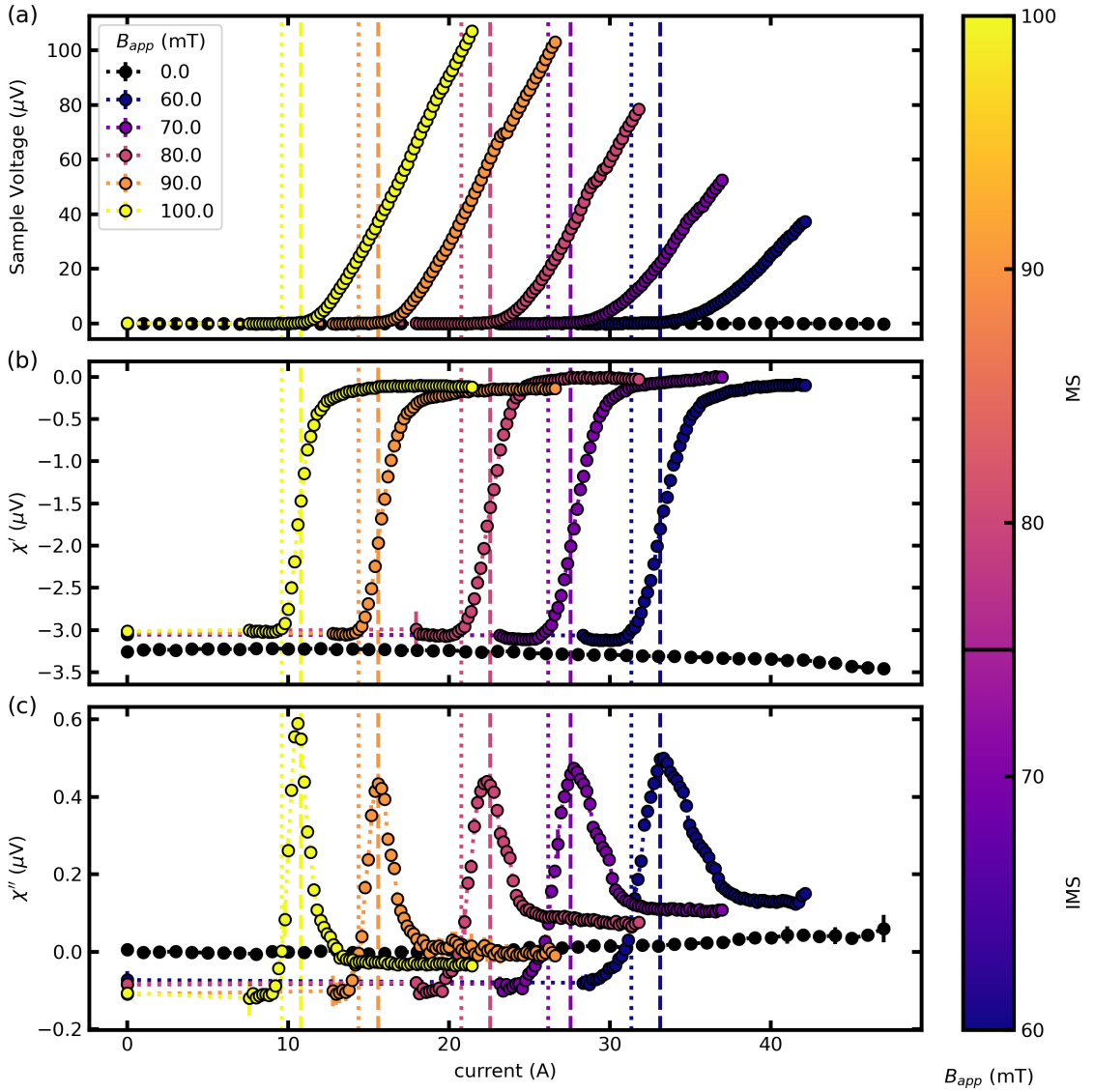

Figure 5.3: Current scans in selected B_{app}. (a) Sample voltage, (b) χ', and (c) χ'', and (d) sample temperature. The voltage critical depinning current I_{cV} as well as the susceptibility critical depinning current $I_{c\chi'}$ are included as vertical dashed and dotted lines, respectively.

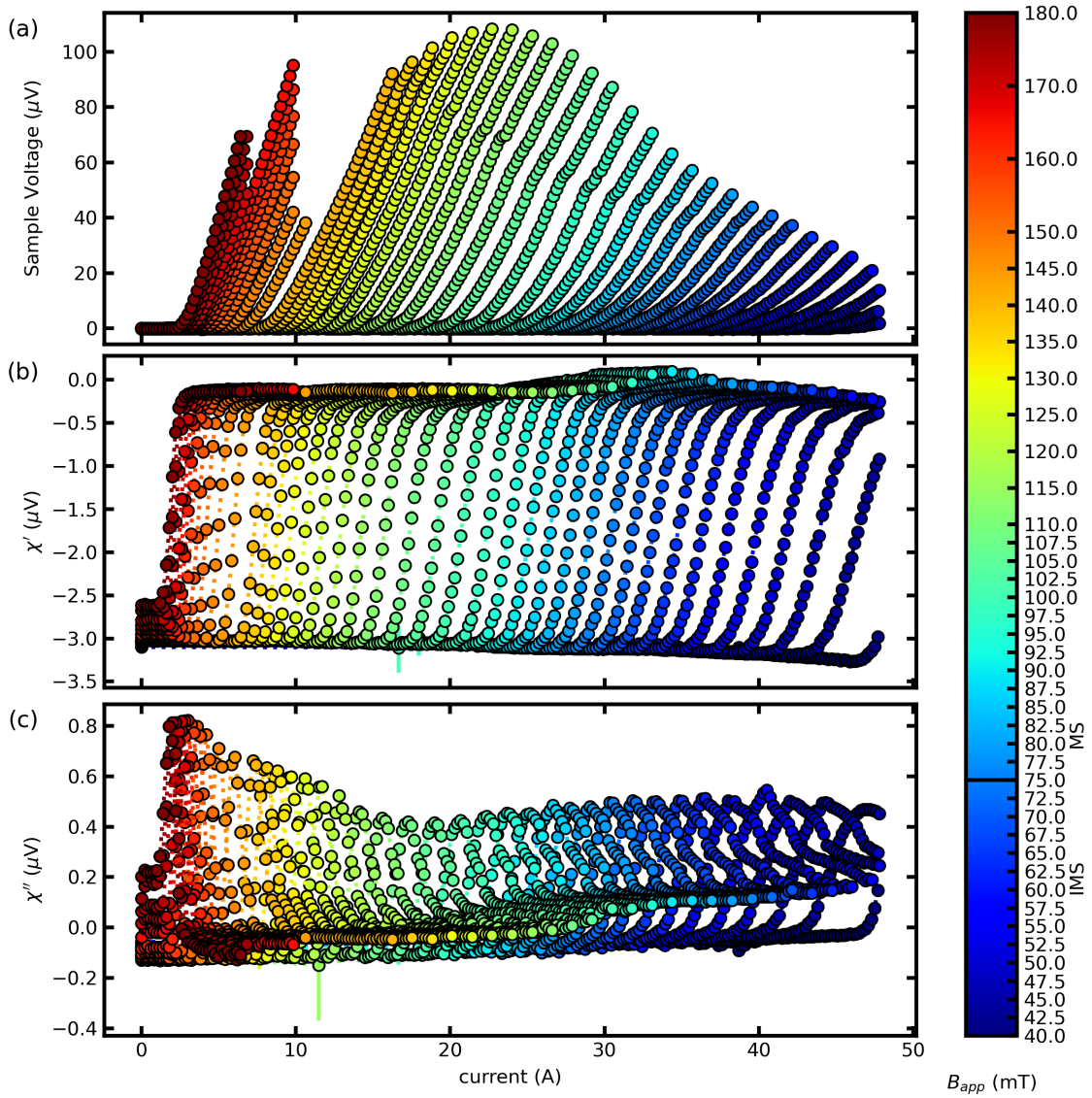

Figure 5.4: Current scans covering a wider range of B_{app}. (a) Sample voltage, (b) χ', and (c) χ''.

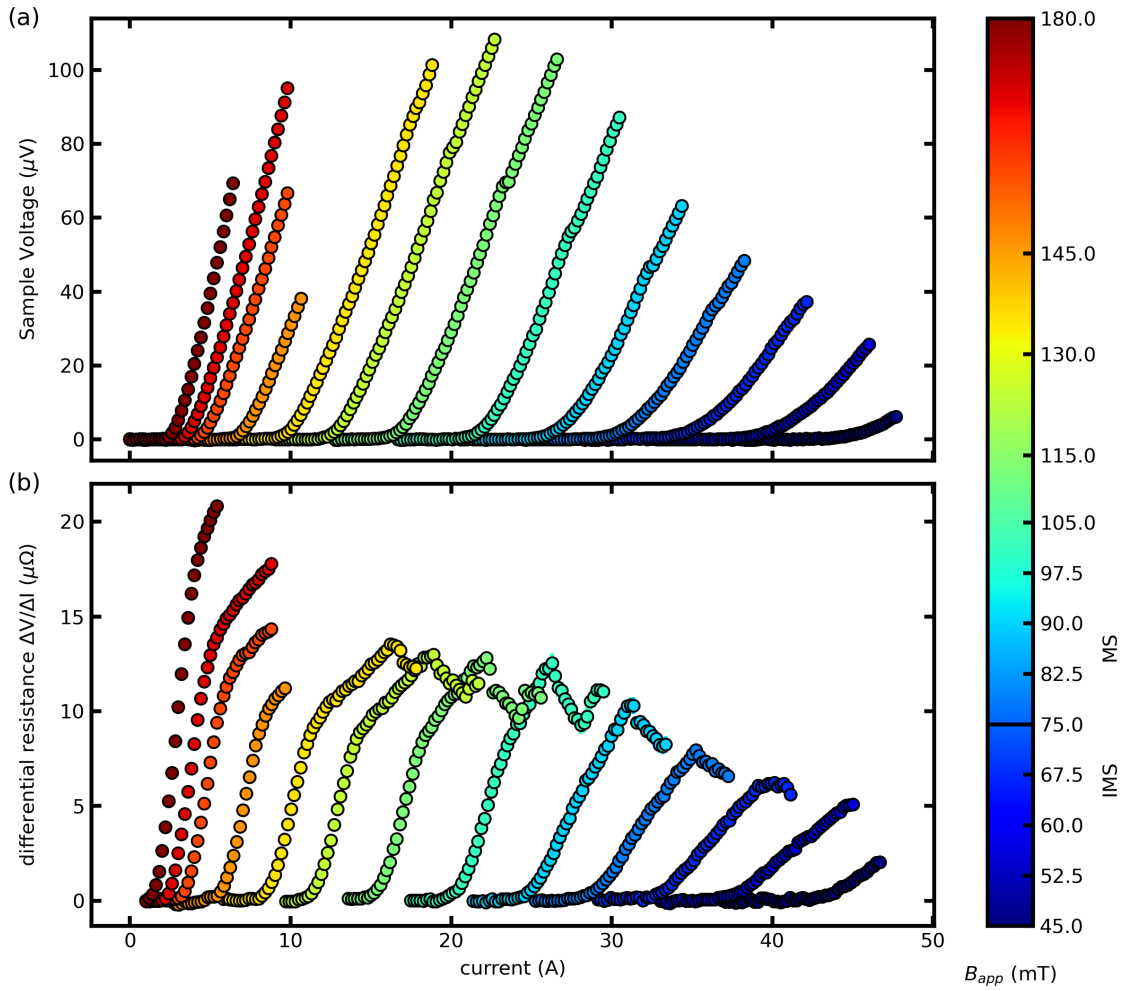

Figure 5.5: Current scans in selected B_{app}. (a) Sample voltage, and (b) differential resistance $\Delta V/\Delta I$.

flux flow regime is reached, where the differential resistance is approaching a constant value. Instead, the differential resistance reveals a non-monotonous voltage response with current showing a changing slope and the appearance of peaks and local minima.

To further analyze the field dependence of the voltage and AC susceptometer signal, we show in figure 5.6 the critical depinning currents $I_{c\chi'}$ and I_{cV} as a function of B_{app} in panel (a), and in panel (b) $\Delta\chi'(\mathrm{I}) = \chi'(I_{max}) - \chi'(0\mathrm{A})$ and $\Delta\chi'(\mathrm{T}) = \chi'(10\mathrm{K}) - \chi'(4\mathrm{K})$ as a function of B_{app} quantifying the range of the χ' signal in temperature and current scans.

We observe in figure 5.6 (a) that over the entire field range the value of $I_{c\chi'}$ is approximately 1-2 A smaller than the value of I_{cV} extracted from measurements in the same B_{app}. The qualitative behavior of I_{cV} and $I_{c\chi'}$ are identical, showing a decreasing critical depinning current with increasing field, with a slight kink at $B_{app} \approx 75$ mT. To better visualize the kink and the different behavior below and above B^*, a power law of the form $I_{cV} = m\,(B_{app})^n$ with the two fitting parameters m and n was fitted to the two field ranges of I_{cV} (see figure 5.6 (c)), as well as a fit of the same function over the entire field range ((see figure 5.6 (d))). This power law nicely fits the two field ranges, but a fit to the entire field range doesn't yield a good agreement with the data and, hence, is not further discussed. For the field range $B_{app} < B^*$, we extract an exponent $n = -1.00 \pm 0.01$, whereas in the field range $B_{app} > B^*$, the fitted exponent is $n = -3.43 \pm 0.03$. However, the low number of points in the low field range renders it difficult to accurately determine the goodness of the fit. A linear fit of the form $I_{cV} = a * B_{app} + I_{c0}$, with the two fit parameters $a = -0.63 \pm 0.01$ and $I_{c0} = 71.23 \pm 0.41$ of the low field range also yields a good agreement with the data and is included in figure 5.6 (e).

We now turn our attention to figure 5.6 (b). The signal range of χ' in temperature scans shows a slowly decreasing behavior for low fields $B_{app} < 100$ mT. For higher fields $\Delta\chi'(\mathrm{T})$ decreases more rapidly. In contrast to that, $\Delta\chi(\mathrm{I})$ shows a non-trivial field-dependence with a peak around $B_{app} \approx 75$ mT, as already observed in figure 5.4 (b). At the high field range for $B_{app} > 135$ mT, we observe a decrease with field of $\Delta\chi(\mathrm{I})$, with a similar slope as observed for $\Delta\chi(\mathrm{T})$.

5.3 Discussion

We summarize the main results presented in the previous sections before we discuss our results further. The measured signal from the custom-built AC susceptometer shows the expected behavior in temperature scans exhibiting a sharp decrease of χ' and a peak in χ''. However, similarly to magnetization measurements in previous studies [16, 53], no sign of the transition to the IMS was observed in temperature scans. The I-V curves obtained from simultaneous electrical transport and AC susceptibility measurements show the typical shape and field dependence, showing a decreasing critical depinning current and increasing slope in the depinned state with increasing field. The slight curvature in the vicinity of I_{cV} is indicative of a plastic depinning transition. The observed kinks in the I-V-curves point in a similar direction and could be caused by transitions between different flow states [70]. The AC susceptibility signal in current scans is qualitatively similar to the response observed in a temperature scan exhibiting a drop in the inductive

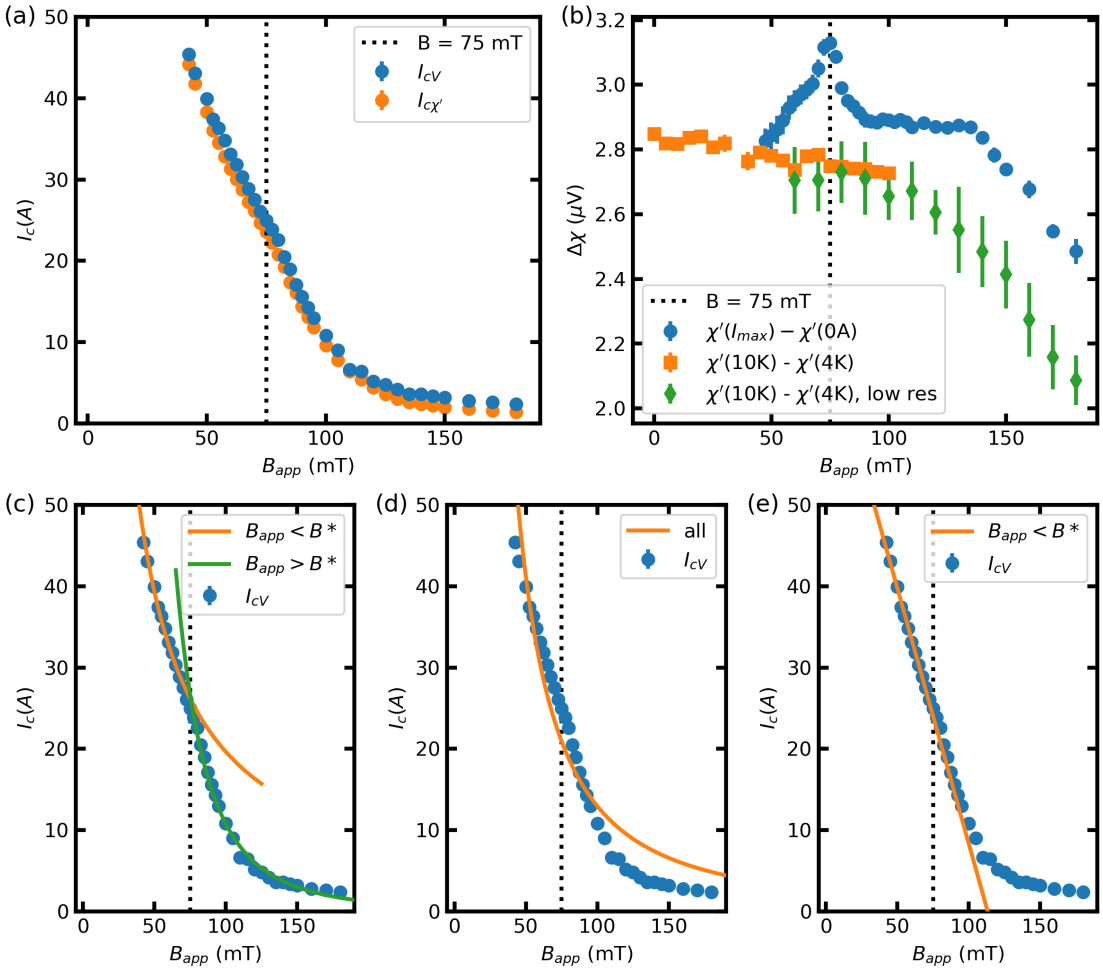

Figure 5.6: (a) Critical depinning current $I_{c\chi'}$ and I_{cV} as a function of B_{app}. We observe a change in behavior around $B_{app} = 75$ mT corresponding to the field, where the transition from the mixed state to the IMS is observed in SANS measurements. (b) $\Delta\chi'(\mathrm{I}) = \chi'(I_{max}) - \chi'(0\mathrm{A})$ and $\Delta\chi'(\mathrm{T}) = \chi'(10\mathrm{K}) - \chi'(4\mathrm{K})$ as a function of B_{app} extracted from current scans (5.4) and temperature scans (see 5.2). The field dependence of $\Delta\chi'(\mathrm{I})$ and $\Delta\chi'(\mathrm{T})$ is similar for high fields but significantly differs at $B_{app} \approx 75$ mT, where $\Delta\chi'(\mathrm{I})$ exhibits an additional peak. (c) The field dependence of I_{cV} above and below $B_{app} = 75$ mT is fitted by a power law of the form $I_c = mB_{app}^n$ with the two paramters m and n and shown by solid lines. (e) Fit of a power law to the entire field range of I_{cV}. (d) Fit of a linear line to I_{cV} for fields below $B_{app} = 75$ mT.

channel and a peak in the resistive channel. Interestingly, we observe features in both the AC susceptibility signal as well as in the voltage response in the vicinity to the field $B_{app} \approx B^* = 75$ mT marking the transition to the IMS at $T = 4$ K and which was extracted from SANS (see chapter 4). Both the voltage critical depinning current I_{cV} and the susceptibility critical depinning current $I_{c\chi'}$ exhibit a kink in the vicinity to B^*. At the same time, the signal range of the inductive signal $\Delta\chi'$(I) shows a peak at the same field.

General Interpretation of the AC Susceptibility Signal

Before we discuss the results further, we comment on the interpretation of the general AC susceptometer signal in temperature scans and current scans. The latter is a non-standard measurement setup, and little material is found in the literature explaining the general shape of the AC susceptibility signal as a function of applied current. An in-depth treatment of the AC susceptibility signal requires modeling of the pinning landscape and the influence of the AC drive field and the transport current on the depinning characteristic of the vortex structures. This would also allow us to properly understand more subtle features such as the change of $\Delta\chi'(I)$ in the vicinity of $B_{app} = 75$ mT and the change in the peak height of χ'' in current scans. However, such a theoretical treatment is beyond the scope of this work, and we focus on a general qualitative explanation of the AC susceptibility signal with current. As pointed out above, the qualitative shape of χ' and χ'' in current scans is very similar to the shape observed in temperature scans. In temperature scans, the drop in the inductive channel corresponds to the screening of the AC magnetic field, marking the transition to the superconducting state, while the peak in the resistive channel corresponds to the temperature where the AC field enters the center of the sample [79]. The AC susceptibility signal can be understood considering Bean's critical state model, where χ' and χ'' are governed by the ratio of the driving field amplitude B_{AC} and the critical depinning current density J_c (see section 3.1). As in our measurements B_{AC} is kept constant, the behavior of χ' and χ'' in temperature scans is directly determined by the field and temperature dependence of J_c. For a given field, J_c is small close to T_c and increases with decreasing temperature. This results in the characteristic shape of the AC susceptibility in temperature scans showing $\chi'' \to -1$ and $\chi'' \to 0$ for decreasing temperatures with a peak at intermediate temperatures corresponding to the point where the Lorentz force induced by the drive field is comparable to the pinning force quantified by the critical depinning current J_c. This is in analogy to the behavior shown in figure 3.2 (b).

We now turn our attention to the AC susceptibility signal in simultaneous transport measurements. At zero current, the scenario is identical to the low-temperature scan, and the AC drive field is unable to penetrate the sample due to the high critical depinning current. For increasing current, the pinning potential of the vortices is partially counteracted due to the Lorentz force induced by the applied current. If the combined action of the transport current and the drive field is sufficient to depin vortices, we observe a change in the AC susceptibility signal. In the vicinity of I_{cV}, the AC drive field can partially penetrate the sample with the peak of χ'' corresponding to the point where the AC drive field reaches the sample in analogy to the AC susceptibility in temperature scans. For higher applied currents, the vortices are depinned and start moving orthogonal to the applied current.

The movement of vortices is dominated by the action of the transport current, which is much larger than the action corresponding to the AC drive field.

In a simpler way, χ'' corresponds to the volume of the sample, into which the AC field penetrates, and a gradient of B_{int} is formed due to the local critical current density J_c counteracting the drive field according to Bean's critical state model. At the same time, this results in a reduction of the diamagnetic signal as now the magnetic field is no longer screened, and χ' is increasing and approaching zero. For increasing current, the area filled with the gradient increases until the vortices are depinned by the transport current. The current, where we observe the peak in χ'', corresponds to the point where the gradient and, with it, the AC field reaches the center. For higher currents, vortices are moving due to the transport current, and no gradient due to the AC field is formed, resulting in a decrease in χ''. However, as the AC field is no longer shielded and penetrates the sample, the diamagnetic moment approaches zero, and the sample appears no longer superconducting based on the AC susceptibility signal.

Field Dependence of I_{cV}

After we have commented on the general AC susceptibility signal in simultaneous transport measurements, we turn our attention to the field dependence of the critical depinning current I_{cV} and the appearance of the kink in the I_{cV} at $B_{app} = B^* = 75$ mT. In general, the critical depinning current marks the point where the Lorentz force overcomes the pinning force. This point is determined by the interaction of the underlying pinning landscape with the VL.

We consider two scenarios based on simplistic geometric arguments depicted in figure 5.7, where the sample splits into stripes of mixed state and Meissner state domains. Both scenarios schematically show the same filling fraction, which is assumed to scale as $f = B_{app}/B^*$. In the first scenario, shown in figure 5.7 (a), the mixed state domains are oriented perpendicular to the current direction, whereas in the second scenario, shown in figure 5.7 (b), the mixed state domains are oriented in the direction parallel to the current direction. As a result, assuming that the current density within the mixed state domains is homogeneous and the current doesn't penetrate the Meissner state domain, except for a thin surface layer of a thickness given by the London penetration depth λ_L, the local current densities inside the mixed state domains of these two scenarios are inherently different, and show a different field dependence. In the first scenario (panel (a)), the current distributes homogeneously in the areas of the mixed state domains and occupies the entire sample cross section independent of the applied field. As a result, the local current density inside the mixed state domains is independent of the applied field. However, the current distribution is heterogeneous in the direction of the current.

In the second scenario (panel (b)), the current distribution is homogeneous along the direction of the applied current, but is heterogeneously distributed in the sample cross section orthogonally to the current direction. As now, the available sample cross section for the current is given as the total mixed state cross section, the local current density is determined by the field dependent filling fraction.

In both scenarios, the elastic moduli of the VL within the mixed stayed domains and the interaction of the VL with the pinning landscape is independent of the applied field and the only known changing parameter of the domain structure as a function of field is the mixed state filling fraction $f = B_{app}/B^*$ determining the thickness of the mixed state domains. Under these assumptions, the *local* critical depinning current density inside the mixed state domains stays unchanged in both scenarios. Therefore, in the scenario shown in figure 5.7 (a), the critical depinning current of the sample should be identical to the depinning current of an individual strip, which should not depend on its width. As the influence of the field is only a change in the width of the mixed state domains, the *macroscopic* critical depinning current measured in experiments should be constant as a function of the field based on these assumptions and is included in the bottom of figure 5.7 (a).

In the second scenario shown in figure 5.7 (b), the *local* current density inside a mixed state domain is larger than the macroscopic current density. It scales inversely with the mixed state volume fraction given as B_{app}/B^*. Again, under the assumption that the *local* critical depinning current density inside the mixed state domains stays unchanged for decreasing B_{app}, the *macroscopic* critical depinning current decreases as $I_c \propto B_{app}/B^*$ for decreasing B_{app} and is included in a schematic drawing in the bottom of panel (b). [5]

In contrast to the results of these simplistic considerations, we observe an increasing depinning current with decreasing field inside the IMS. Only a subtle change in behavior appears at the onset of the IMS, and we extract a different power law for the field range above and below $B^* = 75$ mT. Comparing the fitted exponents of $n = -1.05 \pm 0.01$ below B^* and $n = -3.43 \pm 0.03$ for fields $B_{app} > B^*$ to the theoretical exponents included in table 3.1 suggests a change in the pinning characteristics from collective pinning ($n = -3$) to strong pinning ($n = -1$) [10] at the transition from the homogeneous mixed state to the IMS. Collective pinning is characterized by a large number of pinning sites with a weak individual pinning strength. In the strong pinning regime, the individual pinning strength is large, but the number of pinning sites is reduced. It is not clear how the pinning strength or pinning density is influenced by the breaking up of the mixed state into a domain structure with domain sizes on the order of several to tens of micrometers with $< 10^4$ vortices per domain.

A possible explanation could be given by the additional degree of freedom provided by the Meissner domains acting as voids between the mixed state domains. Due to these voids, vortices at the edge of mixed state domains might be more effectively pinned due to the decreased number of neighboring vortices and the increased freedom to accommodate a pin. This could lead to strongly pinned individual vortices at the edge of the mixed state domains, explaining the transition to the strong pinning regime. Furthermore, it is unclear how the decrease in the connectivity from a homogeneous VL to the domain structure influences the current path and its influence on the depinning mechanism.

A recent work by Wang *et al.* [116] studied the pinning effects of quenched vortex clusters in type 1.5 superconductors using molecular dynamic simulations. Their results suggest

[5] We note that the DC voltage is given as the (time)-averaged measured voltage between the voltage taps. Therefore, the measured voltage scales with the mixed state volume fraction $f = B_{app}/B^*$ and both scenarios still show a field-dependent flux flow resistivity consistent with $\rho_{ff} \propto B_{app}/B_{c2}$.

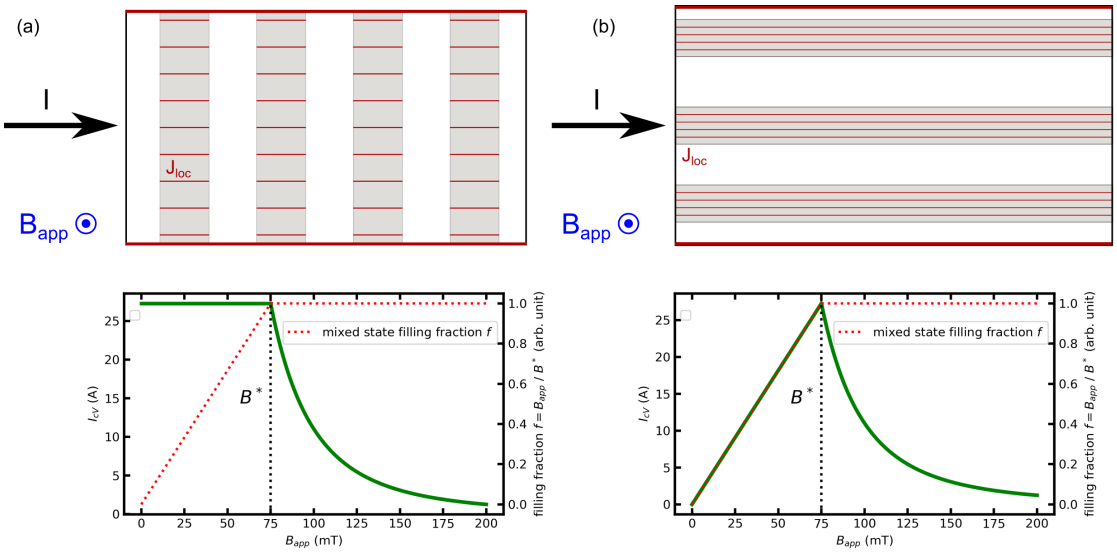

Figure 5.7: Scheme of two simple geometric scenarios of the domain structure. The local current density J_{loc} is represented by the density of the red lines. Assuming that the pinning landscape is identical in both scenarios and that the filling fraction scales as $f = B_{app}/B^*$ the macroscopic critical current I_c should be constant and independent of B_{app} for the first scenario in panel (a) but decrease as $I_c \propto B_{app}/B^*$ in the second scenario shown in panel (b). The bottom graph of each panel depicts the expected field dependence of I_{cV}, where for $B_{app} > B^* = 75$ mT the field-dependence of the power-law fit of figure 5.6 is shown. The filling fraction of the mixed state domains is included as a red dotted line in both panels. More details are found in the main text.

that the pinning mechanism of cluster-forming systems differs from the one encountered in conventional type-II vortices. Comparing a vortex clustering system to a non-clustering system while adapting the pinning characteristics to match the length scales of the two systems, they find that the clustering system has a significantly higher critical depinning threshold than the non-clustering system. A possible explanation of this change could be connected to the vortex interaction showing also many-body character in the intertype regime according to [56]. As individual vortices are no longer the elementary particles of the mixed state, as is the case in classical type-II superconductors, this could be responsible for the more effective pinning of vortex clusters. In addition to the more effective pinning, Wang *et al.* [116] found that cluster-forming systems exhibit a pronounced plastic depinning transition, as is also observed in our system from the increased curvature around I_{cV} for lower fields and the non-monotonous differential resistance in figure 5.5. However, the above study focuses on very dilute systems, where the number of vortices per vortex cluster $N_{vortices}$ is $N_{vortices} = 2 - 4$. This is opposed to our measurements, where we cover the field range of the IMS for fields $B > 0.5B^*$ where $N_{vortices} \gg 4$

An explanation of the change in behavior might be connected to the ability of the transport current to penetrate into the bulk prior to the flux flow regime. The scenario is comparable to the shown schematic drawing in figure 5.9 (a) depicting a plate connected to two current leads, A and B. The current density as a function of increasing distance y from the current leads decreases and is a function of the width of the plate [117]. Similarly, one expects the current density penetrating into a mixed state domain to be influenced by the width along the current direction as schematically shown in figure 5.9 (b). At the applied current,

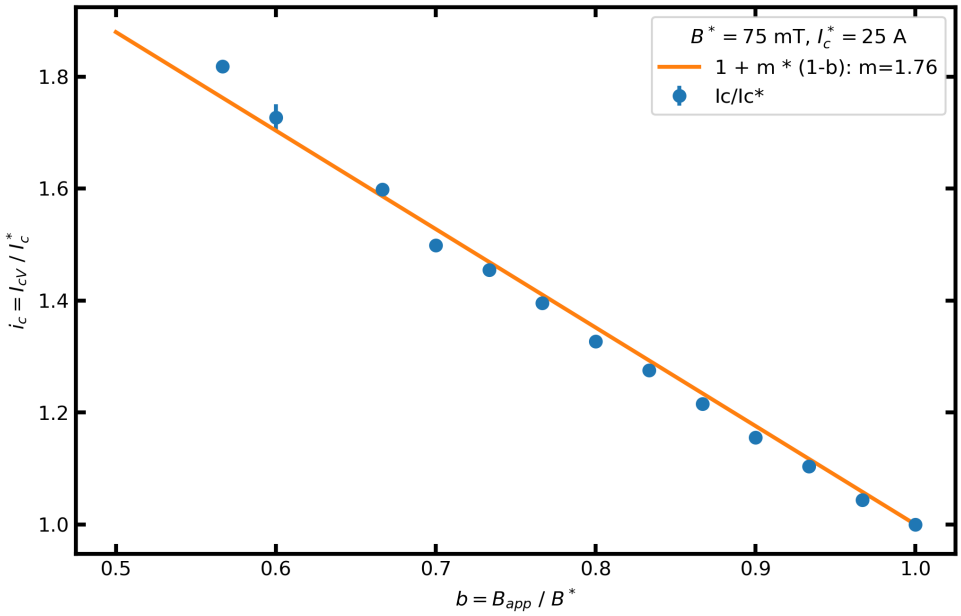

Figure 5.8: Reduced critical current i_c as a function of the reduced field b. The solid line represents a fit of the function $i_c = 1 + m(1 - b)$.

where the current density at the center of the strip exceeds the critical current density, vortices are depinned and start moving, inducing the flux flow resistance. The local critical depinning current density is independent of the applied field inside the IMS field range. However, in contrast to the simplistic scenario depicted in figure 5.7, in the scenario shown in figure 5.9, the local current density at the central point of each strip is reduced and depends on the relative size of the strip thickness compared to the strip length. Therefore, we expect the observed macroscopic critical current to increase with decreasing field as now a higher current has to be applied in order for J_{loc} to exceed the critical current density at the center of the strip.

We can express the critical current in the IMS as a sum of the critical current I_c^* at B^* and the additional term ΔI_c caused by the dilution of the local current density at the strip center due to the field-dependent strip thickness according to

$$I_c(b) = I_c^* + \Delta I_c(b), \tag{5.1}$$

where the field dependence is expressed in terms of the reduced field $b = B_{app}/B^*$. This can be normalized to I_c^*, which yields the reduced critical current i_c

$$i_c = I_c(b)/I_c^* = 1 + \Delta I_c(b)/I_c^* \tag{5.2}$$

Plotting the normalized critical current as a function of the reduced field $b = B_{app}/B^*$ yields a linear regime in the IMS and is shown in figure 5.8. The linear slope was fitted using a function of the form $i_c = 1 + const(1 - b)$, where $const$ is a constant fitting parameter. Comparing the functional dependence of i_c to the extracted field dependence of $d(b)$ from chapter 4 suggests that $\Delta I_c(b)$ is proportional to the thickness $d(b)$.

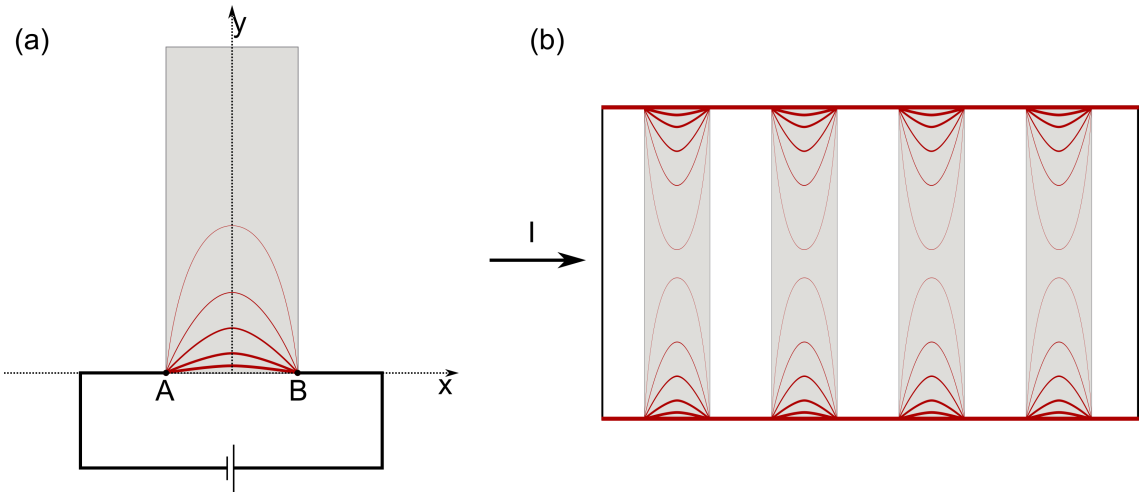

Figure 5.9: (a) Schematic drawing of the current distribution in a current-carrying plate, where the current is injected between points A and B. (b) Schematic drawing of the transport current penetrating into the bulk of the mixed state domains before flux flow is established.

To derive a simple, functional form, we consider the following boundary conditions to determine the current density at the center of the strip. Due to the symmetric shape of the strip, the current density has to be symmetric with respect to its width and length. In areas of the Meissner strips, the current density is constrained to a thin surface layer of the size of the London penetration depth λ_L. Therefore, the current density is expected to have a maximum at the corner of the mixed state strip, where it joins the Meissner region. A simple assumption is that the current density scales inversely with the distance from the corner of the strip. It should be dependent on the length L of the strip as well as on the strip thickness d and show a minimum at the strip center.

Therefore, one of the simplest forms of modeling the local current density at the center of the strip and fulfilling the above criteria is given by

$$J_{loc,center}(b) \propto \frac{d(b)}{L}. \tag{5.3}$$

If we assume d to scale according to equation 4.18 then we get for the field dependence of $J_{loc,center}$

$$J_{loc,center}(b) \propto \frac{1}{1-b}, \tag{5.4}$$

where we dropped the constant factor L and L_0 from equation 5.3 and equation 4.17, respectively. Based on the proposed functional form of $J_{loc,center}$, the critical current increases below $B_{app} = B^*$ in a linear fashion due to the additional dilution of the local current density in the center of the strip.

5.4 Summary

We have presented a detailed study of the AC susceptibility and DC voltage response of Nb-4 in temperature and current scans using a custom-built AC susceptometer and transport measurement setup in a standard SANS cryomagnet. The measurements gave us a detailed map of the magnetic and electrical properties of the sample as a function of temperature, current, and applied field, providing valuable information in preparation for the neutron experiments presented in the following chapter. Furthermore, the field dependence of the critical depinning current reveals a subtle feature at the onset of the IMS, acting as a macroscopic signal of the IMS. This is remarkable as, for example, in temperature scans, the transition to the IMS remains hidden.

At the same time, this study can act as a proof-of-concept implementing an *in-situ* AC susceptibility system for SANS measurements. Although configured in a non-standard geometry, the AC susceptometer allowed to observe the expected temperature dependence of χ' and χ'' of our superconducting sample and highlights that our system can be used to identify phase transitions. At the same time, this non-standard geometry allows to measure *in-situ* with neutron experiments, without having any additional material in the beam. The possibility of performing AC susceptibility measurements *in-situ* during SANS could be very helpful to verify that one is measuring at the correct temperature and field range corresponding to the phase of interest, such as, for example, the small skyrmion pocket in the chiral magnet MnSi [97].

6 Local Reorganization of the Intermediate Mixed State in Nb below the Critical Depinning Current

The contents of this chapter are submitted as a research article to Superconductor Science and Technology. The manuscript is currently under review. The neutron data of this chapter is available on the data platform of the Institut Laue-Langevin [118, 119, 120].

After having elucidated the field dependence of the IMS domain structure in chapter 4 as well as the field dependence of the critical depinning current in chapter 5, this next chapter deals with the main part of this thesis studying the rearrangement of the IMS with current. Using a combined transport and SANS setup, the IMS, under the influence of current, was studied in two Nb single crystal samples in different fields covering a large range of the IMS phase diagram. As a main result, the IMS is found to rearrange over a wide range of the IMS, confirming our previous results of a rearranged stripe structure in the flux flow regime. Interestingly, this rearrangement occurs for currents well below the critical depinning current I_{cV} and can be linked to the interplay of the pinning landscape with the domain structure governed by the intricate physics of the IMS.

In section 6.1, the experimental setup is presented. Section 6.2 summarizes the steps in the SANS data analysis. The results are presented in section 6.3, focusing first on the measurements in a single field to highlight the quantitative current-induced changes in the voltage response, IMS scattering, and VL morphology. We then present a summary of the current-induced changes observed over a wide range of fields in the IMS. Section 6.4 discusses the results further, first summarizing the main observations of the results section and providing a qualitative explanation of the rearrangement process governed by the interplay between the pinning landscape and IMS domain structure. The chapter is concluded in section 6.5, where the main results are summarized.

6.1 Experimental Setup

The experimental setup consisted of a combined transport and SANS setup installed on the small angle neutron diffractometer D33 at the Institut Laue-Langevin [94] to investigate two niobium single crystal samples, Nb-1 and Nb-2. The experimental geometry mirrored that of our previous study [17] and is illustrated in figure 6.1 (a) showing the sample orientation, DC current direction I, direction of the applied magnetic field B_{app}, and the coordinate system referred to from now on. We used a dedicated sample stick, depicted schematically in figure 6.1 (b). The upper portion of the stick featured normal-conducting copper current leads, while the lower portion had superconducting current leads spot-welded to the sample, enabling the application of high currents with minimal Ohmic heating effects near the sample. Helium was allowed to condense in the sample chamber at $T = 4$K, fully immersing the sample to efficiently remove any heat generated by flux flow. During the current scans of Nb-1, the temperature stability was $\Delta T = 0.1$ K. For the measurements on Nb-2, temperature stability was improved to $\Delta T = 0.01$ K over

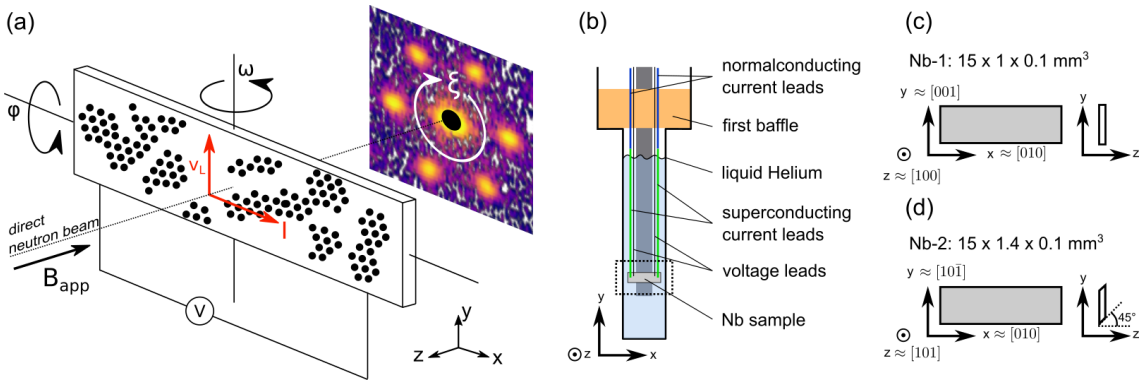

Figure 6.1: (a) Schematic of the scattering geometry. The magnetic field was aligned parallel to the incoming neutron beam. The current direction was in the horizontal plane perpendicular to the applied field, leading to vortex movement in the vertical direction. The scattered neutrons were recorded using a position-sensitive 2D detector placed behind the sample. (b) Schematic cut-view of the cryostats sample tube at the sample position. The sample mounted on the dedicated sample stick is shown inside the dashed rectangle. The lower part of the sample tube was filled with liquid Helium (represented in light blue) close up to the height of the first baffle of the sample stick (shown in orange) coupled to the heat exchanger (not shown). Current leads in the vicinity of the sample were superconducting (shown in green) and transitioned to normal conducting copper wires (shown in blue) in proximity to the first baffle. The voltage leads are presented in black. The crystal orientation with respect to the coordinate system and the sample cross sections of Nb-1 and Nb-2 are included in panels (c) and (d), respectively. Panel (a) is adapted from [17] under the Creative Commons Attribution 4.0 license. Note that the schematics are not to scale.

the duration of the combined SANS and current scans (lasting more than 12 hours) with applied currents up to $I = 45$ A. This improvement was achieved by extending the superconducting current leads and carefully adjusting the cryostat setpoint temperature with increasing current, counteracting Ohmic heating from the normal-conducting wires in the upper section radiating towards the sample. Thin normal-conducting copper voltage leads, necessary for recording characteristic I-V curves, were attached to the sample with silver conducting paint, with a distance of approximately $d = 8$ mm between the voltage taps.

The strip-shaped Nb single crystal samples, Nb-1 and Nb-2, were cut from the same crystal as those used in earlier studies [16, 17, 100]. Their respective crystal orientations and dimensions are shown in the schematic drawings in figure 6.1 (c,d). The crystallographic orientations were confirmed using either neutron or X-ray Laue diffraction. Both samples had rectangular cross-sections, though Nb-2 had beveled edges, leading to a slightly lower critical depinning current density. In previous experiments [17], and for measurements on Nb-1, the applied field B_{app} was aligned nearly parallel to the [100] crystal axis, which caused two degenerate VL orientations due to non-local effects and the shape of the Fermi surface [14, 40]. Since analyzing the SANS pattern of these coexisting VL orientations and their current-induced changes was challenging, Nb-2 was prepared such that B_{app} was aligned nearly parallel to a [101] crystallographic direction. This crystal direction favors a single VL orientation, simplifying the SANS pattern. Additionally, the sample's orientation relative to the current direction was set so that one set of Bragg peaks was aligned roughly parallel to the transport current axis. As a result, minimal to no current-

induced VL rotation was expected [76], making data analysis easier. However, unlike the isotropic low-q scattering observed in measurements on Nb-1 and previous experiments [17], SANS measurements on Nb-2 showed slightly anisotropic low-q scattering even at zero current, rendering the quantitative comparison between the samples challenging. Further details on the sample characteristics are provided in section 3.5.

The samples were positioned in the neutron beam with their long dimension aligned along the x-axis, and the large sample face was oriented perpendicular to the magnetic field. This resulted in a large demagnetizing factor, which extends the phase space for the IMS in the field-temperature phase diagram. The DC current I was applied in the x-direction, corresponding to the [010] crystallographic direction of the samples, and was perpendicular to the applied magnetic field B_{app}. Initially, B_{app} was aligned parallel to the incoming neutron beam, but the setup, including the sample inside the cryostat and the magnet, could be rotated by an angle φ around the y-axis and by an angle ω around the x-axis, referred to as rocking scans. Neutron-absorbing sheets made of cadmium or borated material were used to mask the voltage and current leads. A detailed summary of the instrument configurations and sample environment of the different neutron beamtimes with the experiment numbers 5-31-2911 [118], 5-31-2951 [119], and 5-42-573 [120] can be found in table 3.4.

High-field scans in the normal state, used for background subtraction and transmission correction, were conducted at fields above the upper critical field, $B_{c2}(4\text{ K}) \approx 270$ mT, at a temperature of $T = 4$ K and with zero applied current. All measurements followed a field-cooling (FC) protocol, where the sample was cooled from the normal state above the transition temperature, $T_c = 9.25$ K, down to $T = 4$ K in the presence of B_{app} and no applied current. Subsequently, rocking scans were performed either at zero current or after the DC current, supplied by a Genesys 60-55 power supply from TDK Lambda, was increased in incremental steps. Simultaneously, the DC voltage response was monitored using a Keithley Model 2701 digital multimeter.

6.2 Data Analysis

The typical SANS contributions and their analysis in zero currents have already been discussed in section 4.2. Here, we focus on the analysis of the current-induced changes in the IMS. To quantify the effect of the current on the IMS, we tracked changes in the voltage response, the IMS scattering, and the Bragg peak scattering as a function of the current building on the data analysis presented in [17]. First, we outline the key steps in determining the critical depinning currents from the voltage measurements. Next, we discuss qualitative changes observed in the 2D SANS detector images with increasing current. Subsequently, we develop analysis tools to quantify the degree of the current-induced anisotropy in the low-q IMS scattering related to the current-driven rearrangement. The current-induced changes in Bragg peak scattering are analyzed similarly to the field-dependent Bragg peak behavior discussed in the previous section. For further details on the Bragg peak scattering analysis, we refer the reader to section 4.2.

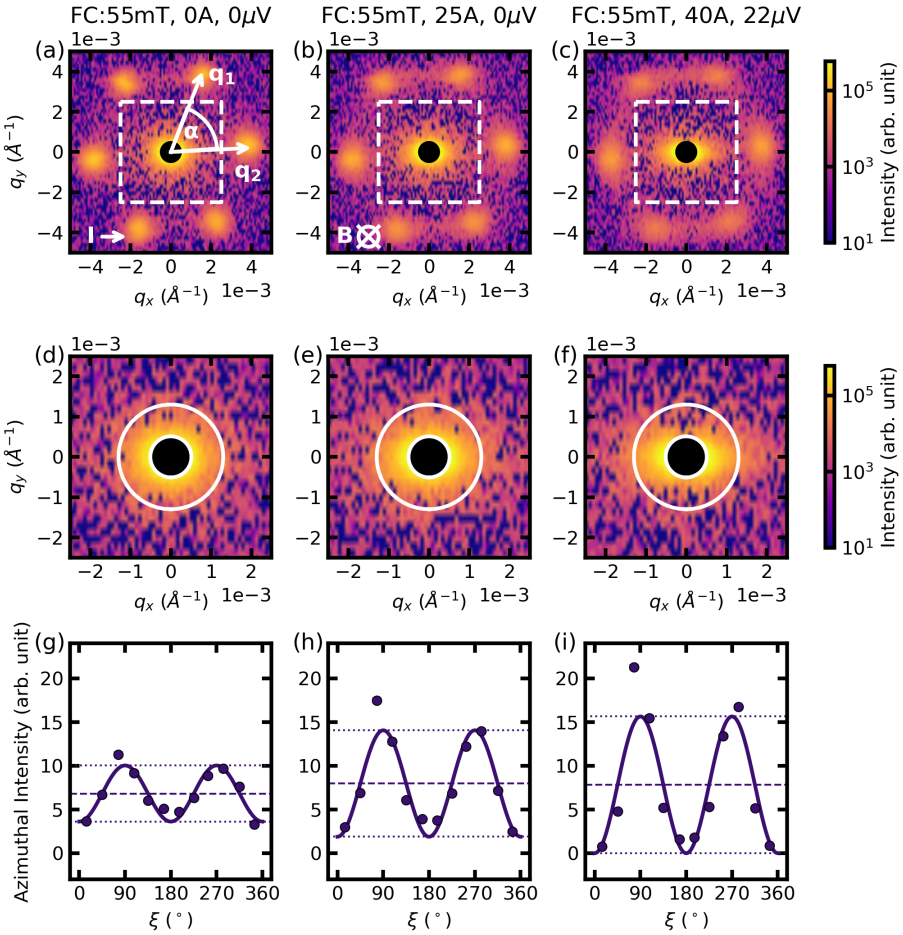

Figure 6.2: Examples of 2D SANS detector images and quantitative analysis of the current-induced IMS anisotropy on the example of Nb-2 measured in $B_{app} = 55$ mT at $T = 4$ K. (a-c) Transmission and background corrected 2D SANS detector images of the Bragg peak scattering and the IMS intensity. Shown is the sum of the rocking scans with a blacked-out direct beam. (d-f) Corresponding zoomed-in 2D SANS detector images of the data inside the dashed square of the first row focusing on the IMS intensity. (g-i) Azimuthal curves of the IMS intensity inside the sector marked between white circles in panels (d-f). The error bars are smaller than the marker size. The solid lines are fits of $I_0 \cdot \sin^2(\xi) + y_0$. The direction of the applied current and the magnetic field are indicated at the bottom of panels (a,b). The Bragg peak positions q_i of two adjacent Bragg peaks and the angle α between them are included in panel (a). The values of B_{app}, I, and V are included above each column.

DC Voltage

During the neutron experiments, the DC voltage was recorded with a sampling period of 2 seconds. The voltage values used to construct the I-V curve were averaged for each current. For Nb-1, voltage measurements during neutron beamtimes were only taken for currents that were also probed with neutrons. To increase the current point density, additional offline characterization measurements were performed, with data recorded at an average sampling period of 10 seconds. These offline measurements aligned closely with the I-V curve obtained during neutron experiments. As a result, the I-V curves used to extract I_{cV} for Nb-1 were based on these offline characterization data. For Nb-2, voltage measurements were also performed for additional currents, filling in the gaps between the currents probed by neutrons. This enabled the construction of I-V curves sufficient for extracting I_{cV}. In both samples, I_{cV} values were derived from the I-V curves using a $3\sigma = 0.35$ μV voltage criterion, where σ represents the standard deviation of the zero-current voltage. This voltage criterion corresponds to an electric field of $E = 0.5$ μV/cm, calculated using the distance $d \approx 8$ mm between the voltage taps. It aligns well with the commonly used electric field criterion of 1 μV/cm used in the literature [10].

SANS Data Analysis

Figure 6.2(a-c) presents examples of 2D SANS detector images of the IMS. Panel (a) corresponds to the pristine field-cooled (FC) state, panel (b) shows the state measured at a current just below $I < I_{cV}$, and panel (c) illustrates the SANS image for $I > I_{cV}$. As the current increases, the Bragg peaks broaden both azimuthally and radially. Additionally, the low-q IMS intensity near the blacked-out direct beam (see zoomed-in views in figure 6.2 (d-f)) develops a significant anisotropy in the horizontal direction parallel to the current.

The degree of low-q anisotropy was quantified through azimuthal scattering curves, $I(\xi)$, integrated over the radial direction. The azimuthal angle ξ is defined on the detector plane, with the q_y-axis corresponding to $\xi = 0°$. These azimuthal curves were derived from 2D scattering data, summed over rocking angles φ and ω, and restricted to data within the sector outlined by white circles in figures 6.2 (d-f). Figures 6.2 (g-i) show examples of the resulting azimuthal scattering data $I(\xi)$ with a bin size of $\Delta\xi = 30°$.

The azimuthal data, $I(\xi)$, was fitted using the function $I(\xi) = I_0 \cdot \sin^2(\xi) + y_0$, shown as solid lines in figures 6.2 (g-i). We note that while this phenomenological function provides a simple fit, unlike a sum of Gaussian functions, it does not account for any changes in peak width along the azimuthal direction. There is no fundamental reason the peak shape should remain unchanged, but factors such as the limited azimuthal resolution near the direct beam made it difficult to detect any significant changes in the peak width. This choice of fitting function offers a consistent and reliable method to quantify the anisotropy of the low-q IMS scattering across the field and current range with a minimal number of parameters. To take into account the field-dependent variation in scattering intensity (see

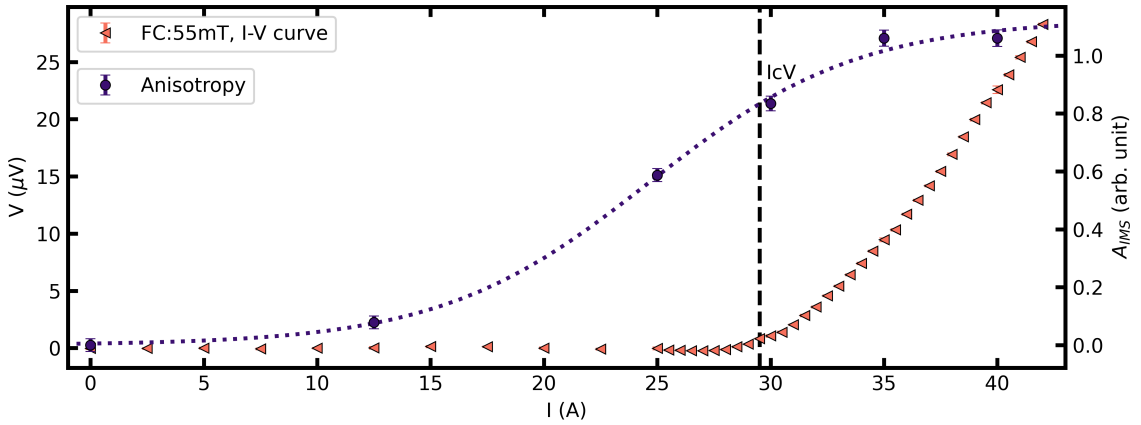

Figure 6.3: I-V-curve (orange solid triangles, left y-axis) and the current-induced relative IMS anisotropy A_{IMS} (purple solid dots, right y-axis) on the example of Nb-2 measured in $B_{app} = 55$ mT, $T = 4$ K. The critical depinning current inferred from the transport measurements is marked by the vertical dashed line. The transition of A_{IMS} was fitted with a phenomenological s-shaped function of the form $a/(1 + e^{-(I-b)/c})$ with the fitting parameters a, b, c. The fit result is plotted as a dotted purple line.

[100]), the normalized anisotropy, $I_{0,norm}$, was calculated by dividing the fitted I_0 by the mean intensity derived from the fit parameters according to

$$I_{0,norm} = I_0/(0.5 \cdot I_0 + y_0). \tag{6.1}$$

The parameter y_0 in the fitting function was constrained to $y_0 \geq 0$, resulting in the normalized anisotropy $I_{0,norm}$ ranging from 0 for no anisotropy to 2 for maximum anisotropy. To extract the effect of current on the anisotropy, the current-induced relative IMS anisotropy, A_{IMS}, was calculated for each current and field by subtracting the constant low-current value of the normalized anisotropy at the same field.

6.3 Results

We investigated the voltage response and the changes in the SANS pattern for currents ranging from 0 A to 50 A across six magnetic fields, from 30 mT to 62 mT, to cover a broad portion of the IMS phase at $T = 4$ K. We first focus on measurements on Nb-2 in $B_{app} = 55$ mT and $T = 4$ K, which serves as an example to highlight the quantitative effects of the current-induced rearrangement, as observed through the macroscopic voltage response and the IMS anisotropy.

Voltage Response and IMS Anisotropy

Figure 6.3 presents both the I-V curve and the corresponding values of A_{IMS}. Focusing first on the voltage response, we see that for low currents, the voltage remains zero, as expected for a superconductor with a pinned VL. Once the current exceeds the critical depinning current $I_{cV} = (29.5 \pm 0.5)$ A, the I-V curve transitions into a nearly linear

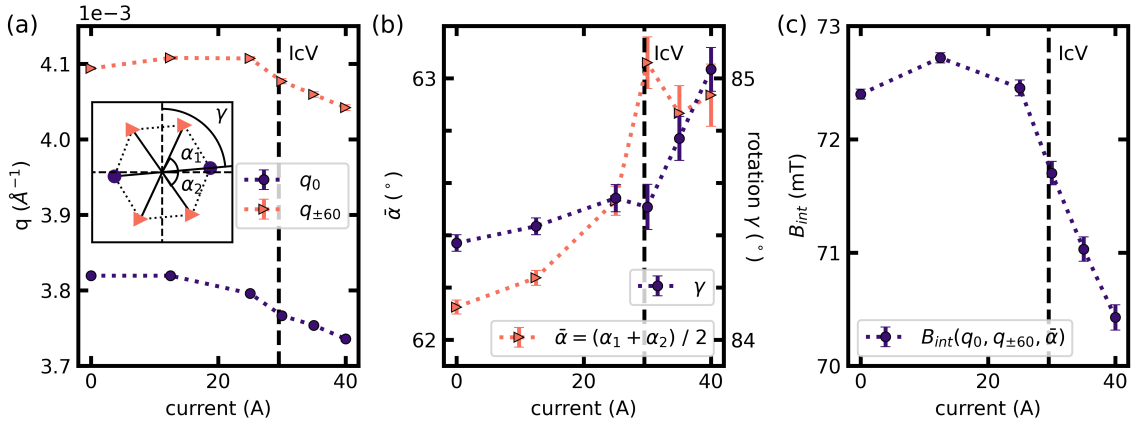

Figure 6.4: VL morphology as a function of applied current on the example of Nb-2 measured in $B_{app} = 55$ mT, $T = 4$ K.(a) Average peak position in q, (b) average angle between the Bragg peaks $\bar{\alpha}$ and the VL rotation γ, (c) the derived internal magnetic field B_{int}. Shown is the average value of equivalent Bragg peaks close to parallel to the axis of the applied current (q_0 marked by purple solid dots) and of equivalent peaks located at approximately $\pm 60°$ with respect to the applied current direction ($q_{\pm 60}$ or $\pm 60°$ marked by orange solid triangles). The definition of Bragg peaks and the angles are also included in the inset of panel (a) using the same color code. The vertical dashed line in each panel marks the critical depinning current inferred from transport measurements (see figure 6.3). The dotted lines are a guide to the eye.

behavior, with a slight curvature near I_{cV}. Shifting to the low-q anisotropy, A_{IMS} remains nearly constant for low currents but then increases in an S-shaped manner as the current rises. At high currents, the A_{IMS} curve levels off, approaching a constant value. A comparison of the I-V curve and A_{IMS} reveals that the anisotropy in the low-q scattering pattern begins to increase before a continuous vortex flow marked by the appearance of a non-zero voltage is observed.

Vortex Lattice Morphology

A similar trend can be observed from the analysis of the VL Bragg peak scattering for the same current scan, as shown in figure 6.4. Figure 6.4 (a) depicts the peak positions in q of the first-order Bragg peaks, averaged over sets of equivalent Bragg peaks: peaks close to the current axis (referred to as q_0) and peaks located at approximately $\pm 60°$ with respect to the axis of the applied current (referred to as $q_{\pm 60}$). At low currents, both sets of Bragg peaks maintain a constant value, but as the current increases, a slight decrease in q is observed.

Changes in the VL rotational angle γ (relative to the vertical axis) and the average angle between adjacent Bragg peaks $\bar{\alpha}$ are shown in igure 6.4 (b). The angle $\bar{\alpha}$ increases by nearly 1° as the current rises up to approximately 30 A, after which it remains stable with an average value of $\bar{\alpha} = (63.0 \pm 0.1)°$. The VL rotation angle γ remains nearly constant with a slight upward trend for currents up to 30 A. For higher currents exceeding 30 A, a sharp increase in γ is observed.

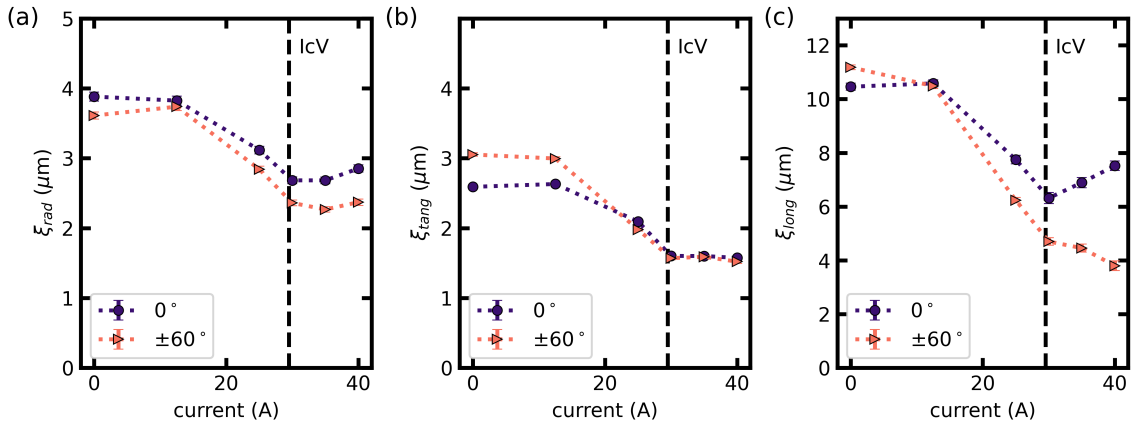

Figure 6.5: VL correlation lengths in (a) radial, (b) tangential, and (c) longitudinal direction as a function of current on the example of the same scan as depicted in figure 6.4. Shown is the average value of equivalent Bragg peaks (0° marked by purple solid dots and ±60° marked by orange solid triangles). The definition of the Bragg peaks is included in the caption and the inset of figure 6.4 (a) using the same color code. The vertical dashed line in each panel marks the critical depinning current inferred from transport measurements (see figure 6.3). The dotted lines are a guide to the eye.

The average Bragg peak positions and the average angle $\bar{\alpha}$ between them can be used to calculate the internal magnetic field B_{int} according to equation 3.46, where $q_1 = q_{\pm 60}$, $q_2 = q_0$ and $\alpha = \bar{\alpha}$. The results are presented in figure 6.4 (c). At low currents, we observe an average internal magnetic field of $B_{int} = (72.50 \pm 0.05)$ mT. As the current increases, B_{int} begins to decrease at approximately $I \approx 30$ A. At $I = 40$ A, the calculated value is $B_{int} = (70.75 \pm 0.15)$ mT.

Vortex Lattice Correlation Lengths

Next, we focus on the correlation lengths ξ_i in the radial, tangential, and longitudinal directions as depicted in figure 6.5. The radial (ξ_{rad}) and tangential (ξ_{tang}) correlation lengths are both found within the plane perpendicular to the direction of the applied current, while the longitudinal correlation length (ξ_{long}) describes the correlation along the field direction. The correlation lengths are calculated individually for each Bragg peak and then averaged over equivalent peaks. In analogy to the data presented in figure 6.4, we distinguish between Bragg peaks close to the current axis (labeled as 0°) and peaks located at approximately ±60° with respect to the axis of the applied current (labeled as ±60°).

The correlation lengths ξ_i exhibit a similar trend across all three spatial directions. Initially, at low currents, ξ_i remains constant before we observe a decrease for $I > 12.5$ A well before reaching the critical depinning current $I_{cV} = (29.5 \pm 0.5)$ A. For $I \geq I_{cV}$, ξ_{rad} and ξ_{tang} stabilize at nearly constant values. In contrast to that, ξ_{long} displays a different behavior depending on the Bragg peak orientation: For peaks aligned at 0°, ξ_{long} exhibits a slight increase with increasing current, whereas for peaks at ±60°, ξ_{long} continues to decrease as the current rises.

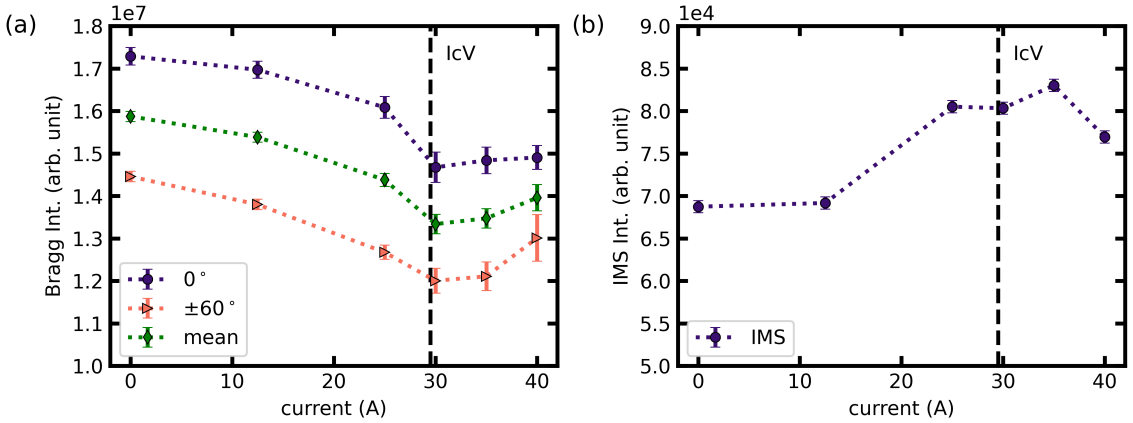

Figure 6.6: Integrated Bragg peak intensity and integrated IMS intensity as a function of applied current corresponding to the same scan as shown in figure 6.4 and figure 6.5. Shown is the mean intensity of equivalent Bragg spot (0° marked by purple solid dots and ±60° marked by orange solid triangles) and the mean intensity of all first-order Bragg peaks (marked by green solid diamonds). The definition of the Bragg peaks is included in the caption and the inset of figure 6.4 (a) using the same color code. The vertical dashed line in each panel marks the critical depinning current inferred from transport measurements (see figure 6.3). The dotted lines are a guide to the eye.

Integrated Bragg and IMS Intensity

Lastly, we examine the current dependence of both Bragg peak intensity and IMS intensity, as depicted in figure 6.6. Figure 6.6 (a) shows the averaged integrated Bragg peak intensity extracted from rocking curves of peaks along the current axis (0°) and peaks located at approximately ±60° with respect to the current axis. It also includes the mean integrated intensity of all first-order Bragg peaks. The data reveal a decrease in intensity with increasing current for $I \geq 12.5$ A. For currents $I \geq 30$ A, the intensity remains nearly constant for peaks along the current axis, whereas peaks at ±60° exhibit a slight increase. The mean intensity for high currents $I \geq 30$ A is $\approx 10 - 15\%$ lower than the integrated Bragg peak intensity at zero current.

The IMS intensity, derived from the integrated intensity of the azimuthal curves, is presented in figure 6.6 (b). We observe a slight increase with increasing current of $\approx 15\%$ for $I > 12.5$ A, which stabilizes to a nearly constant value for currents $I \geq 25$ A.

We quickly summarize the main features extracted from the current scan of Nb-2 in $B_{app} = 55$ mT at $T = 4$ K. From the I-V-curve a critical depinning current of $I_{cV} = (29.5 \pm 0.5)$ A was extracted. Significant changes were observed for currents well below I_{cV} in both the low-q anisotropy, quantified by A_{IMS} (see figure 6.3), and the VL morphology derived from the Bragg peak scattering (see figure 6.4 and figure 6.5). These observations indicate that a rearrangement of the VL occurs well before a continuous flow of vortices, as marked by a non-zero voltage, is observed. Current-induced changes in the SANS pattern for currents well below I_{cV} were observed across a wide range of fields B_{app} within the IMS. However, measurements for fields above B^* within the pure mixed state did not show any measurable changes in the Bragg peak widths before a voltage signal appeared. Once a voltage was detected for fields $B_{app} > B^*$, the rocking curves exhibited a broadening

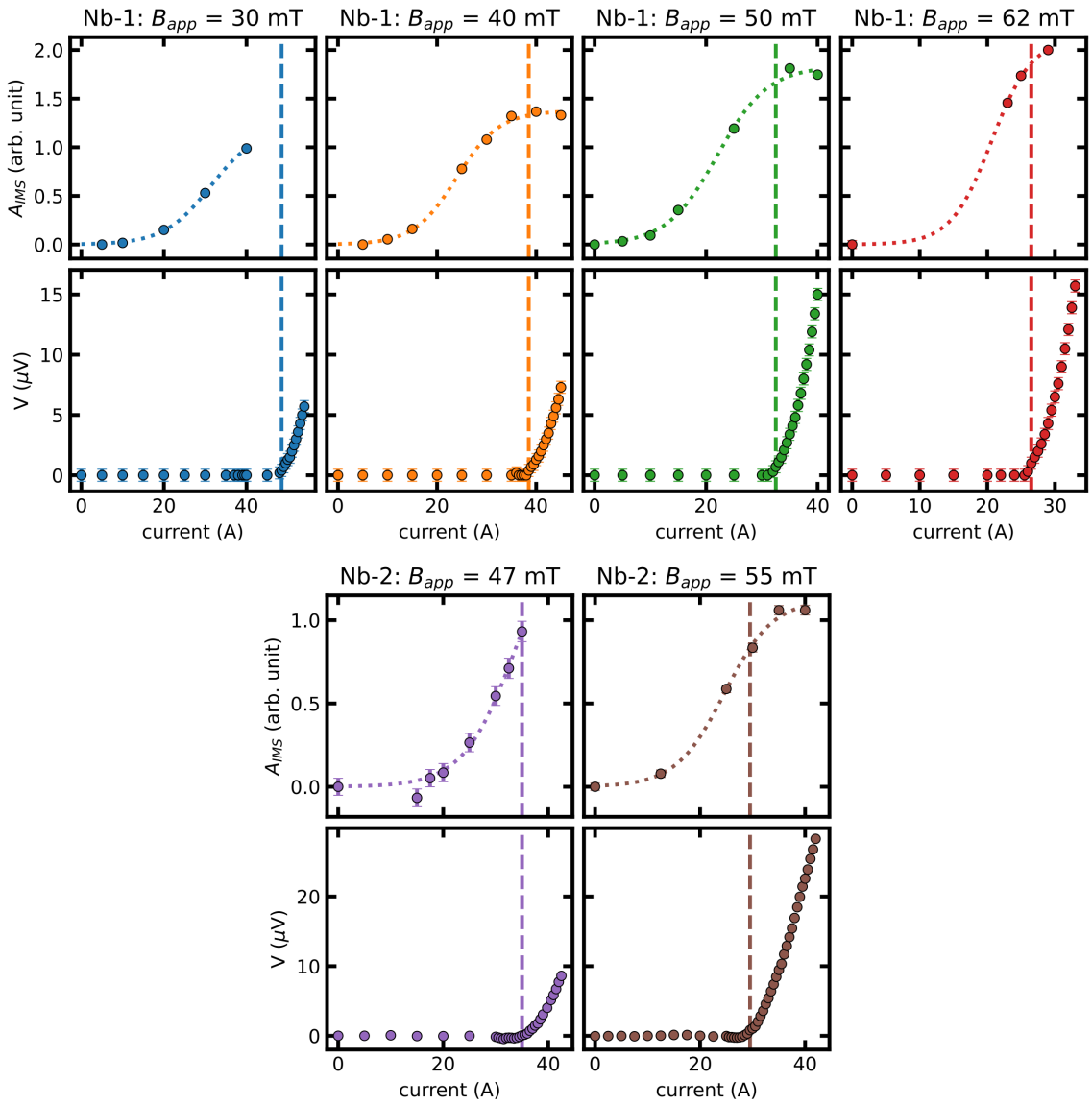

Figure 6.7: Comparison of the current dependence of the relative induced IMS anisotropy A_{IMS} (first row) and the sample voltage V (second row) in different B_{app}. The used sample is indicated above each column. The critical depinning current I_{cV} obtained from the voltage criterion $V > 0.35$ μV is included as a vertical dashed line in each panel. The transitions of A_{IMS} were fitted individually for each field with the same phenomenological s-shaped function as included in figure 6.3 and are shown as dotted lines.

consistent with the self-field caused by the excess current $(I - I_{cV})$ entering the bulk. This thesis focuses on current-induced phenomena within the IMS field range, which will be the subject of the following analysis.

Voltage Response and IMS anisotropy for Various Applied Fields

Figure 6.7 illustrates the extracted values of A_{IMS} as a function of current, along with the corresponding I-V curves for various values of B_{app}. Measurements on Nb-1 are shown in the first double row, while measurements on Nb-2 are included in the second double row. The critical depinning current I_{cV} for each field is marked as a dashed vertical line in both panels of each column. The individual I-V curves show a similar current-dependent behavior to the one presented in figure 6.3, with zero voltage for $I < I_{cV}$ and a nearly linear response for $I > I_{cV}$. Again, a slight curvature is observed around I_{cV}.

The qualitative behavior of A_{IMS} across all studied fields and samples follows a pattern similar to that shown in figure 6.3. As the current increases, A_{IMS} rises, eventually flattening and reaching a saturation point at higher currents. In some cases, time constraints prevented measurements over the full current range necessary to capture the complete saturation value. When only comparing measurements on Nb-1, a trend seems to emerge: the saturation value of A_{IMS} appears to increase with the applied magnetic field. For Nb-2, a similar trend is not observed due to the insufficient number of probed fields and limited current range during neutron measurements.

6.4 Discussion

After presenting the results in the previous section, we now summarize and discuss the key findings, focusing on the rearrangement process of the VL based on measurements from Nb-2 in an applied magnetic field of $B_{app} = 55$ mT at a temperature of $T = 4$ K (see figures 6.3-6.6).

Considering only the voltage response of the sample, the IMS domain structure appears pinned for currents below the critical depinning current, $I < I_{cV}$, and begins to move orthogonally to the applied current at values near I_{cV}. However, a detailed analysis of the SANS data reveals that the IMS domain structure undergoes a rearrangement at currents significantly lower than I_{cV}, where no voltage is detected.[6] The SANS measurements revealed distinct changes in both the low-q IMS scattering and the Bragg peak scattering for currents well below I_{cV}, indicating a rearrangement of the IMS domain structure. Interestingly, no such precursor was observed in the Bragg peak scattering for fields $B_{app} > B^* = 75$ mT within the pure mixed state. Within the IMS, this rearrangement for currents $I < I_{cV}$ occurs across a broad range of fields.

[6] It is important to note that any movement of vortices, including transient or localized motions, produces a voltage response. However, with the voltage measurement setup used in this study (see section 6.2), only the DC voltage associated with continuous vortex flow can be detected.

The low-q anisotropy clearly reveals the current-induced formation of parallel stripes aligned with the direction of flux flow. This observation confirms our previous findings [17] on a similar sample and extends the range of fields where the current-induced rearrangement of the IMS is observed. The rearrangement mechanism has been attributed to the combined effects of the current-induced Lorentz force, vortex viscosity, and attractive intervortex interactions and was previously observed to coincide with the onset of flux flow indicated by a finite voltage [17]. Here, by increasing the sampling density of currents below I_{cV} in our SANS measurements, we observe a clear anisotropy even before a non-zero voltage signal appears.

We conducted offline characterization measurements at different temperatures around $T = 4$ K to rule out the possibility that the difference between I_{cV} and the current at which the first changes in the SANS pattern appear could be attributed to the finite temperature stability. A temperature variation of $\Delta T = \pm 0.1$K (matching the temperature stability of measurements on Nb-1) resulted in an I_{cV} variation of $\Delta I_{cV} = \pm 1.5$ A for measurements at $B_{app} = 50$ mT. This is much smaller than the observed difference of 10-20 A between I_{cV} and the current at which the extracted quantities of the SANS pattern first changed.

To investigate the possibility that the stripe structure forms via mixed state "fingers" extending from the sample edges, the sample height was scanned in the direction parallel to the movement of vortices using a reduced aperture size of $a_x \times a_y = (5 \times 0.15)$ mm^2 at an intermediate current. No significant variation in the current-induced IMS anisotropy was observed across the six different scanned positions, which spanned the full height of the sample (see section A.2). These results suggest that the rearrangement mechanism is uniform across the sample and independent of its height, ruling out that the stripes are penetrating from the sample edges.

In the following, we discuss our results in greater detail by proposing a potential scenario for the rearrangement process occurring for currents below I_{cV}, taking into account previous works and our comprehensive study of the VL morphology and the anisotropy of the low-q IMS scattering.

Previous Results on Pinning and the Current Distribution

We first summarize the results of recent works focusing on the influence of pinning on the domain formation and the local current distribution in the IMS. These act as main ingredients in the following proposed rearrangement mechanism. A recent publication employing molecular dynamics simulations investigated the impact of pinning on the formation of IMS domains during FC temperature scans [54]. The study revealed that the IMS transition is notably robust against pinning, and the resulting domain structure remains qualitatively similar despite variations in pinning characteristics. The research indicated that, regardless of the specific pinning landscape, pinning centers reduce vortex mobility and introduce defects into the initially homogeneous VL above the IMS. These defects act as disruption points within the VL and serve as nucleation sites for the development of mixed-state domains during the IMS formation.

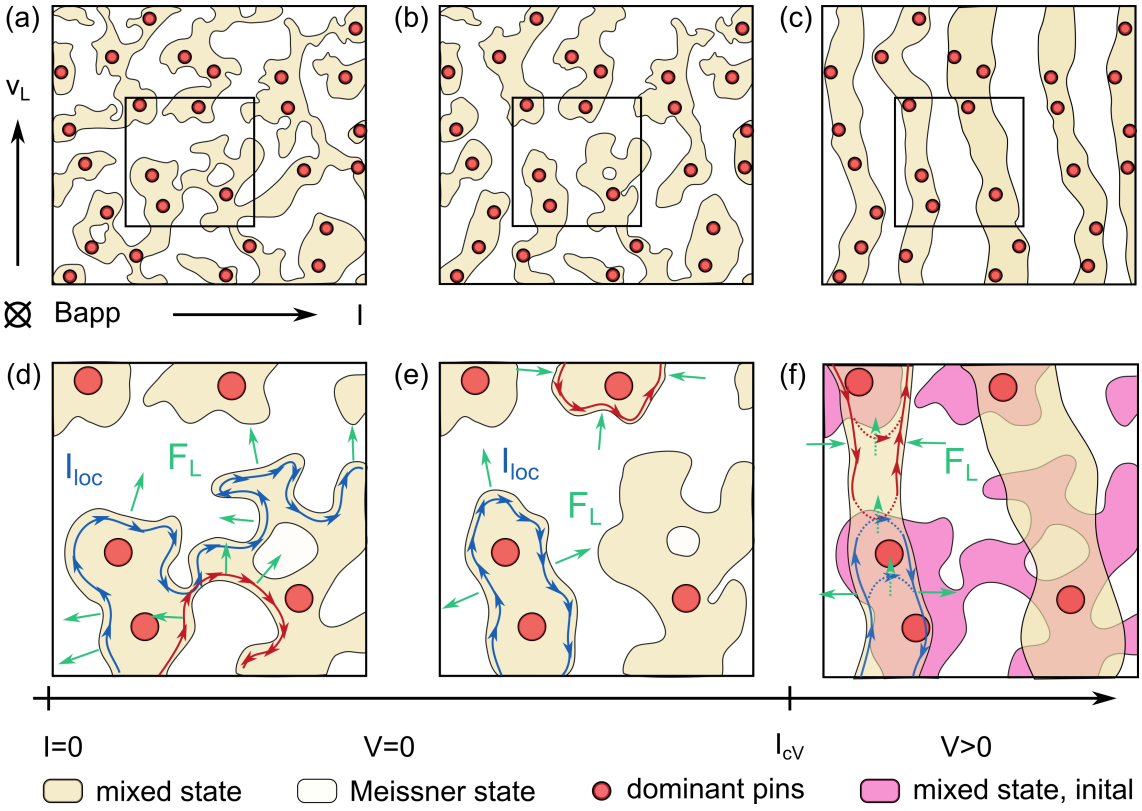

Figure 6.8: Schematic representation of the rearrangement process. (a) Pristine state for zero applied current: The domain structure is formed around strong pinning sites (represented as red dots). (b) Gradual rearrangement of the domain structure for currents $I < I_{cV}$, where no continuous voltage is detected. (c) Domain structure in the flux flow state. Mixed state domains are depinned from the strong pinning sites, and the continuous flow of vortices induces a finite voltage response $V > 0$. (d-f) Zoom in on the domain structure within the black square shown in the first row. The local current path I_{loc} (blue and red lines) and the resulting Lorentz force F_L are schematically included. We distinguish local current paths leading to a Lorentz force pointing into the mixed state domains (red) and outside the mixed state domains (blue). The directions of the current I, applied field B_{app} and movement of vortices v_L are indicated in panel (a).

The domain structure of the IMS significantly affects the local distribution of the transport current. In numerical simulations employing a system of coupled time-dependent Ginzburg-Landau equations as a qualitative model for the IMS, it was observed that the current density tends to concentrate at the interfaces between mixed-state and Meissner-state domains in the direction of vortex movement [17]. This phenomenon can be intuitively understood as a result of the superposition of the clockwise-circulating superconducting currents of individual vortices and the applied transport current. At the leading edge of a mixed-state domain parallel to the direction of the vortex movement, the combined effect of these currents results in an increase in the total current density. Analogously, at the rear edge of the domain, the superposition leads to a lower current density.

Local Rearrangement Mechanism

Based on these findings and our results presented in section 6.3, we propose a possible elongation process, which is schematically depicted in figure 6.8. Figure 6.8 (a) depicts the pinned state of the IMS after an FC at low currents. In this state, the IMS domains are unchanged, and no voltage is observed. Figure 6.8 (b) illustrates the quasi-pinned state at an intermediate current $0 < I < I_{cV}$. Although no voltage is detected, there are clear changes in the SANS pattern, indicating that the IMS domain structure undergoes rearrangement. Figure 6.8 (c) shows the fully depinned state at a current in the flux flow regime $I > I_{cV}$, where a finite voltage $V > 0$ is observed, indicating a continuous vortex flow. A zoom-in of each state is provided in the bottom row (figures 6.8 (d-f)), highlighting the detailed changes in the IMS structure and current distribution as the current is increased.

Our proposed rearrangement mechanism assumes that the initial domain structure is shaped by a pinning landscape dominated by strong pinning sites, which are spaced at a length scale comparable to the VL correlation length. This pinning landscape would lead to the formation of mixed state domains composed of multiple grains or patches, similar to the domain structures observed in molecular dynamic simulations [54]. The strong pinning sites lead to the pinning of individual vortices within the patches, while the remaining vortices are only weakly pinned. The weakly pinned vortices are immobilized by their attractive interactions with the strongly pinned vortices, which leads to a constant intervortex distance.

When a transport current is applied, it generates the Lorentz force, F_L (indicated by green arrows), which acts against the pinning force. Examples of the schematic local current path, I_{loc}, are included in the schematic drawings of figure 6.8 (d-f). A current path that results in a Lorentz force, F_L, pulling outward from the mixed state domain is marked in blue, while a current path that leads to an inward push on the domain is marked in red. Due to the concentrated current density at the front of the mixed state domain, as discussed in [17], the Lorentz force predominantly exerts a pulling force at the front of the domain.

For low currents, the resulting Lorentz force, F_L, is insufficient to depin any vortices. As a result, the vortex arrangement remains essentially identical to the pristine domain structure depicted in figure 6.8(a,d). This behavior is also observed through the nearly constant values of the quantities extracted to evaluate the VL morphology, as shown in figures 6.4 and 6.5, and the low-q anisotropy A_{IMS}, as demonstrated in figure 6.3 and figure 6.7.

At higher currents $I < I_{cV}$, although no voltage is detected, clear changes are observed in the SANS pattern. The increased anisotropy, as seen in figure 6.3, and the reduction of the correlation lengths, as shown in figure 6.5, with increasing current, are consistent with a local rearrangement of mixed state domains. In this scenario, individual domains become elongated, and disorder is introduced due to the shear forces between the VL patches within each domain. Locally, the Lorentz force F_L is strong enough to overcome the pinning of the weakly pinned vortices but still insufficient to unpin the strongly pinned vortices. However, due to their attractive interactions, the weakly pinned vortices are not

completely removed from a VL patch but are instead only able to rearrange. As a result, weakly pinned, vertically aligned sections of mixed state domains move upward and are eventually absorbed in the upper extent of a domain pinned by strong pinning sites, leading to a gradual elongation of mixed state domains. This rearrangement goes unnoticed in voltage measurements since it does not generate a measurable voltage within the timescales probed. Given that the net current flows horizontally, the resulting net Lorentz force and subsequent rearrangement causes the individual VL domains to elongate vertically, as schematically illustrated in figure 6.8 (b,e).

For higher currents $I > I_{cV}$, a measurable voltage appears while both A_{IMS} and the correlation lengths across the three spatial directions remain nearly constant (see figure 6.3 and figure 6.5). In the proposed mechanism, this behavior aligns with F_L surpassing the pinning strength of the strong pinning sites, resulting in a fully depinned state. The vortices move vertically, producing the observed voltage, as schematically depicted in figure 6.8 (c,f).

The proposed mechanism is also compatible with the field dependence of I_{cV} presented in the previous chapter (see chapter 5). The gradual rearrangement for $I < I_{cV}$ of the weakly pinned vortices is predominantly driven by the current density at the domain boundary. Once, the stripe structure is formed, the ability for the current to penetrate into the center and depin all vortices is determined by the field-dependent geometry of the mixed state domains as outlined in section 5.3.

The near-constant values of all three correlation lengths further supports the local rearrangement mechanism for $I < I_{cV}$. In the fully depinned state, where vortices within a domain move at a similar speed, minimal shear between individual VL patches within the mixed state domains is expected. The slight increase in ξ_{long} for Bragg peaks at 0° (see figure 6.5) aligns with a current-induced dynamic reordering, consistent with findings from [76]. The observed decrease in ξ_{long} for Bragg peaks at ±60° can be attributed to the excess current $(I - I_{cV})$ penetrating into the bulk of the mixed state domains, creating an additional magnetic self field B_{self}. This additional field causes vortices to bend continuously in the z-y plane, resulting in broadened rocking curves and reduced ξ_{long} values for Bragg peaks at ±60°, in line with results from previous studies [17, 74]. Examples of the schematic local current paths, I_{loc}, bridging a mixed state domain are shown as dotted lines in figure 6.8(f). The excess current penetrating the bulk may also explain the slight decrease in B_{int} with increasing current observed for $I > I_{cV}$ (see figure6.4). The Lorentz force, which predominantly acts as a pulling force on the front of the mixed state domains, could stretch the VL and consequently reduce B_{int}. Additionally, a detailed analysis of the Bragg peak and IMS intensity suggests that the current drives the sample closer to its equilibrium state, decreasing the macroscopic flux trapped during the FC measurement procedure (see appendix A.3 for a detailed analysis).

In the depinned state, we also observe a slight rotation of the VL towards the energetically favorable orientation, aligning with the direction of vortex movement (see figure 6.4). This

agrees with the aforementioned study [76] also reporting a current-induced rotation of the VL. [7]

The local rearrangement process observed below the critical depinning current can be attributed to the complex interplay between the pinning landscape and the VL domain structure, as determined by the physics of the IMS. In the quasi-pinned state, the IMS's inherent heterogeneity allows individual vortices greater freedom to rearrange themselves, thereby seeking a lower energy configuration. This contrasts sharply with the homogeneous mixed state in type-II superconductors, where vortices interact purely repulsively. In this scenario, weakly pinned vortices are constrained by their interactions with neighboring vortices and cannot rearrange individually unless the entire lattice is depinned.

Numerical simulations indicate that the stripe structure can form due to the current even in the absence of pinning [17], demonstrating that pinning is not a fundamental requirement for the self-organization of the IMS into stripes. However, our findings suggest that pinning enables the observation of an intermediate regime where, although no voltage is detected, significant changes in the SANS pattern reveal a transition to a stripe structure. This rearrangement is evident across a broad range of fields. The increasing saturation value of A_{IMS} with higher fields implies that the stripes become straighter as the field increases, potentially due to the field-dependent variation in the width of mixed state domains (see appendix A.4 for more details).

Before concluding this section, we address the apparent paradox to the current path in the depinned IMS. In a perfect stripe structure, there is no continuous path of mixed state domains aligned with the direction of the applied current, which raises the question of how the current flows through the depinned IMS. The idea of a connected path through mixed state "bridges" between vertical mixed state strips can be ruled out. Such bridges would create an additional central vertical streak in the SANS pattern, leading to a low-q cross pattern, which is not observed. The absence of this feature, combined with the aligned stripe structure of the IMS, implies that the current path likely involves joining the sample surfaces in the regions occupied by Meissner state strips. The current then penetrates the bulk of the sample primarily within the mixed state domains, resulting in a highly heterogeneous current path that remains to be fully understood.

6.5 Summary

In this chapter, we explored the influence of a transport current on the intermediate mixed state in two Nb single crystal samples using a combined transport and SANS setup. We have confirmed our earlier observation of a current-induced rearrangement of the IMS into parallel stripes aligned with the vortex flow direction [17]. As a main result, we observe, thanks to an increased density of currents below I_{cV}, an intermediate regime where the stripe formation takes place at currents well below I_{cV} over a wide range of fields. Through a comprehensive analysis of the current dependence of the low-q IMS domain scattering, the VL morphology, and voltage response, we propose a coherent mechanism for this

[7] We note that the experimental setup in [76], more specifically the current axis, is rotated by 90° with respect to our study, leading to a SANS pattern with Bragg peaks aligned on the vertical q_y-axis in the depinned state.

rearrangement. This mechanism is linked to the interplay between the underlying pinning landscape and the IMS domain structure governed by the rich physics of the IMS. Our findings underscore that the IMS under the influence of a transport current provides a fascinating model system for exploring complex ordering and non-equilibrium phase transitions in two-phase systems.

7 Conclusion and Outlook

This work has applied small-angle neutron scattering (SANS) in combination with lab-based characterization tools to study the properties of the intertype superconductor Nb as a function of field, temperature, and current. This chapter summarizes the main findings of this thesis and sheds light on future perspectives of the study of vortex matter transport phenomena in intertype superconductors.

Chapter 2 reviewed the main superconducting material classes and provided a background on previous works studying superconducting vortex matter with a focus on the intermediate mixed state and current-induced vortex matter states. In Chapter 3, the theoretical foundations of the experimental methods of this thesis were presented, first focusing on lab-based characterization tools before shedding light on neutron scattering methods to study superconducting vortex matter, more specifically SANS. The three main experimental contributions were presented in chapters 4 - 6 and are summarized in the following.

In chapter 4 results from SANS were presented, to follow the IMS domain formation as a function of the applied field in a bulk Nb single crystal sample. SANS, being sensitive to structures with length scales ranging from 1-1000 nm, allowed for the probing of the VL morphology and tracing the transition of the IMS via the position and widths of the VL Bragg peaks. For fields below the critical value $B^* = 75$ mT, the homogeneous mixed state breaks up into VL domains and Meissner state domains, which is clearly visible in the Bragg peak scattering and its extracted quantities such as constant local internal field B_{int} acting as a well-known hallmark of the IMS [15, 16, 17]. At the same time, the domain structure leads to an additional scattering contribution in the SANS pattern at low-q. However, the correlation peak connected to the micrometer-sized IMS domain structure [53] lays outside the accessible q-range of a standard SANS setup. Therefore, only its high-q tail appearing as a power-law scattering at the low-q end of the SANS regime, was observed in the presented SANS data. This diffuse IMS power-law scattering was analyzed in chapter 4 using a newly developed approach based on the well-known Porod law [92]. The modified Porod analysis takes into account the degree of alignment to extract a corrected value of the specific surface area of the IMS domain structure, which can be used to derive the repetition length of the IMS domain structure. The presented results agreed well with previous studies extracting this length scale from USANS measurements [53] and Landau's theory of domains in superconductors [66]. Furthermore, the extracted values of the repetition length exceed the theoretical SANS upper length-scale limit by almost two orders of magnitude, highlighting the power of the presented analysis approach in extending the accessible length scales of a standard SANS instrument. In principle, this approach could also be adapted to other systems, and the specific surface area can be connected to the length scales of the individual scattering objects.

After characterizing the IMS domain structure and VL morphology as a function of field, chapter 5 showed results from a detailed lab-based characterization campaign of the electrical and magnetic properties of stripe-shaped Nb single crystal samples as a function of field, temperature, and current. The measurements were performed using a custom-built AC susceptometer and transport measurement setup inside a SANS cryomagnet that was

implemented within the scope of this thesis and allows for *in-situ* measurements during neutron scattering experiments.

The presented data, taking into consideration that a SANS cryomagnet is not optimized to host such a system, is of remarkably good quality and acts as a proof-of-concept of the possibility of performing *in-situ* AC susceptibility and transport measurements during neutron experiments. It furthermore allowed for the detection of a subtle feature in the macroscopic electronic and magnetic response at the onset of the IMS. This could allow to test for the existence of the IMS prior to expensive neutron measurements.

Consistent with previous works [16, 53], no signs of the IMS transition were observed in temperature scans of the magnetic properties of the Nb single crystal samples. Combined transport and AC susceptibility measurements in different applied fields revealed that a subtle change in the field dependence of the critical depinning current occurs in the vicinity of B^* extracted from the SANS characterization presented in chapter 4. The field dependence for applied fields below B^*, where the internal structure of individual mixed state domains and the local critical depinning current density stay unchanged, was connected to the field dependence of the size of the mixed state domains obtained from the SANS measurements presented in chapter 4. This suggests that the critical depinning current in the IMS is determined by geometrical constraints given by the spatial distribution and size of the mixed state domains, which is the only thing that is changing with the applied magnetic field in the IMS.

Finally, results from systematic SANS and transport measurements presented in chapter 6 revealed that a current robustly rearranges the IMS domains into parallel stripes oriented orthogonal to the applied current and parallel to the moving vortices. The rearrangement was observed over a wide range of fields, which confirms and extends previous results of the current-induced self-organization of the IMS [17]. While previously [17], this rearrangement was observed in the vicinity of the critical depinning current I_{cV}, the detailed, quantitative study of the VL morphology and diffuse IMS scattering paints a different picture. Both the VL correlation lengths and the current-induced IMS anisotropy show distinct changes for currents well below I_{cV}. No such precursors are observed in the field range of the canonical mixed state. The rearrangement can be connected to the intricate interplay of the IMS domain structure with the underlying pinning landscape and reveals that the IMS under the influence of a transport current can be used for a model system to study non-equilibrium phases.

Overall, this work underlines that the IMS represents a remarkable realization of a pattern-forming model system that can be tuned via temperature, field, and, as highlighted by this work, a transport current. While this thesis presented new methods to study and further elucidate the intricate physics of the IMS, especially focusing on the effect of a transport current, there are several new directions and unsolved mysteries to explore. Here, several new ideas will be presented concerning the experimental setup and the sample geometry with respect to the applied current.

The current investigations have focused on quasi-steady-state scenarios, where the data acquisition time scales (seconds to minutes) far exceed the relaxation times observed in dynamic vortex matter studies, which are on the order of 10-100 milliseconds [121]. Recent studies have demonstrated that driven vortex matter exhibits a reversible-to-irreversible

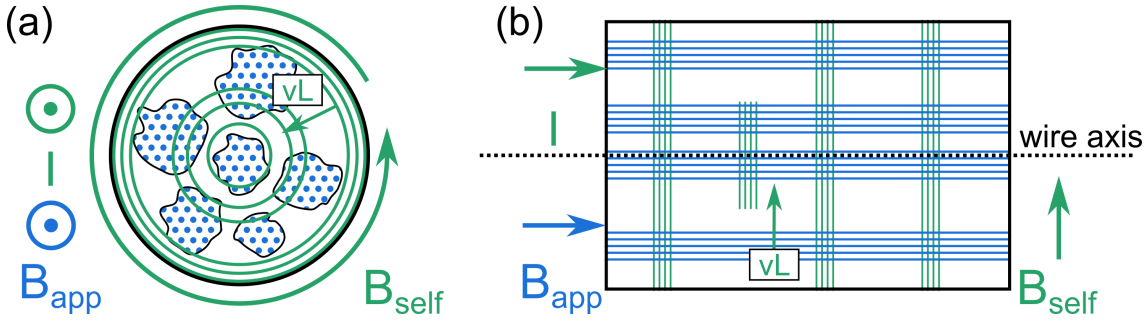

Figure 7.1: Schematic drawing of the "force-free" flux flow configuration in the IMS. The current-induced self field B_{self} nucleates an additional set of circular vortex loops that move to the central wire in addition to the dominant axial vortices caused by B_{app}.

flow transition (RIT) [122, 123, 124, 125]. Investigating the time evolution of the voltage response in the IMS could reveal whether the attractive vortex interaction and the presence of multiple length scales in the IMS alter the RIT. This aspect has not been explored in systems with non-monotonic particle interactions, characterized by an attractive and repulsive term, such as is the case in the IMS [126]. Additionally, recent theoretical and experimental works have explored the voltage response of a homogeneous mixed state under the influence of two mutually perpendicular alternating current drives [127, 128]. It would be interesting to conduct similar experiments on the IMS to understand how the current-induced stripe structure affects the current and vortex flow in the orthogonal direction.

The measurements of this thesis involving a transport current have been performed in the conventional flux-flow geometry, where the field and the current are applied orthogonal to each other. It would be interesting to study the IMS in the so-called 'force-free' configuration, where the current is applied parallel to the applied field, as already mentioned in the introduction. The data of experiments performed on Nb in the canonical mixed state [75] suggest that vortex loops corresponding to the current-induced self field move to the wire axis, resulting in dissipation.

It is not clear how the attractive vortex interaction leading to a domain structure consisting of mixed state and Meissner state domains influences this movement of vortex loops, which also experience an attractive vortex interaction. The flux-free space – due to the Meissner domains –could potentially lead to an increased critical depinning current as opposed to the canonical mixed state of identical local flux induction B_{int} inside the mixed state domains of the IMS. The 'force-free' configuration is sketched in figure 7.1. So far, it was not achieved to prepare a sample that both shows the IMS and a low enough critical current to exceed the vortex pinning in the 'force-free' configuration.

Similarly, the Corbino disk geometry offers an additional interesting experimental geometry to study the effect of a current on vortex matter, both in the canonical mixed state and in the IMS. In a Corbino disk, the current is injected at the center of a disk-shaped sample and collected at the outer radius of the disk, leading to a radially decreasing current density. If the current exceeds the critical current density everywhere in the sample, all vortices are moving in a meta-vortex around the disk center. By fine-tuning the applied current, one can reach an interesting scenario, where vortices in the central region with

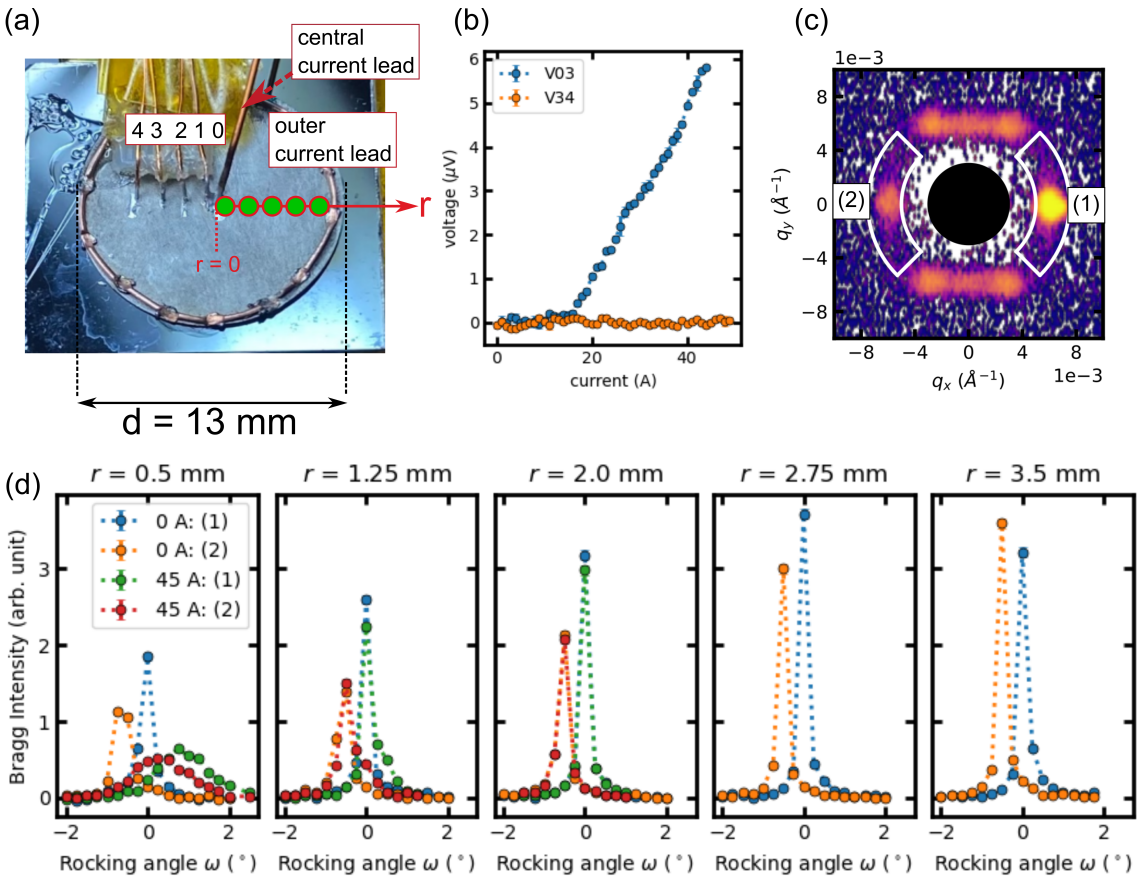

Figure 7.2: Preliminary results from a thin Nb Corbino disk sample in $B_{app} = 200$ mT for zero current and $I = 45$ A. (a) Photo of the sample with an indication of the measured sample areas (marked in green with the spot size to scale) and the numbering of the voltage taps (note that the voltage tap 0 in the vicinity of the central current lead was added after the photo was taken). (b) The voltage between the different voltage taps indicated in the photo. (c) 2D SANS detector image for $B_{app} = 200$ mT, $I = 0$, $r = 0.5$ mm with the sector definition of the rocking curves. (d) Bragg peak intensity of the left (1) and right (2) Bragg peaks in ω rocking scans for the different measured positions indicated above each plot. No difference is observed for $r \geq 2.0$mm.

radius $r < r_c$ below a critical radius r_c are depinned and start moving in a circular motion around the wire center, whereas vortices for $r > r_c$ remain pinned. In direct proximity of r_c, interesting phenomena are expected due to the influence of shear between the moving and pinned VL. The region of moving vortices and pinned vortices could be directly determined using an array of voltage taps in a radial direction and identifying areas of non-zero voltage between two adjacent voltage taps as pinned and small but finite voltage as moving. Again, the influence of the attractive interaction on this geometry offers an even wider area of rich physics to explore.

Figure 7.2 shows preliminary results of a Corbino disk study in a sample cut from the same single crystal as all the samples of this work. Experimentally, the Corbino disk geometry revealed itself as challenging. So far, it was not possible to prepare disk-shaped single crystal samples thinner than ≈ 120 μm, which allowed to induce flux flow within a radius of $r \leq 1.5$mm in a field of $B_{app} = 200$ mT. The minimal feasible beam size

is limited to $d = 1$ mm due to the decreased countrate with decreasing aperture size. As the central current lead also has a finite size covering the central region of radius $r \leq 0.5$mm, this left only a minimal area and a number of points to explore the current-induced changes of the vortex matter using spatially resolved SANS. Furthermore, the influence of demagnetization effects already led to a change in the Bragg peak intensity as a function of position even in the region $r > r_c$, where the VL remained pinned (see panel (d)). Overall, this made it challenging to firstly realize experimental conditions where an increased sample area with current-induced changes can be studied and, secondly, untangle the different effects due to the current-induced movement of vortices as well as due to the changing demagnetization factor for different spatial positions in the sample. Nevertheless, current-induced changes are observed in the rocking curve in the central measured spot at $r = 0.5$ mm as well as a slight shoulder in the rocking curve at $r = 1.25$ mm. The broadened rocking curve is consistent with a moving VL, whereas the shoulder at $r = 1.25$ mm indicates that a fraction of the VL at the probed position was moving, whereas the majority remained pinned. However, no significant difference is observed for $r \geq 2.0$mm. The analysis is ongoing but complicated due to the degeneracy of the two VL orientations if the field is applied along a [100] direction (see the twelve Bragg spots in figure 7.2 (c)) as also reported in our previous study [17].

From an experimental technique point of view, it would be interesting to include scattering and imaging techniques that expand the accessible length scales of SANS and yield further insight into the IMS under the influence of current in the same experimental geometry as studied in this thesis using a strip-shaped Nb sample. Previously, techniques such as ultra small-angle neutron scattering using a Bonse-Hart camera or neutron grating interferometry based on the Talbot-Lau interference effect allowed to directly probe the IMS domain structure on the micrometer and millimeter-scale as a function of field and temperature [15, 53, 16]. It would be interesting to perform similar experiments under the influence of the transport current. However, the studied sample volumes are by a factor of ≈ 100 smaller than the ones studied in the above works, which renders the aforementioned experiments challenging. The use of stroboscopic SANS techniques [121] could be employed to observe the time evolution of the domain structure rearrangement using pulsed currents. Similarly, the large sample volumes required for neutron experiments necessitate a significant reduction in the critical depinning current to achieve the high current densities and short rise times needed to study the system's time evolution effectively.

Overall, many of the proposed experiments would benefit enormously from a sample with a lower critical depinning current density. This would allow to either use larger sample volumes, significantly reducing the counting times or also use larger current densities, potentially observing different non-equilibrium phase transitions, such as current-induced reordering in the flux flow regime. A systematic study of the critical depinning current of samples with different surface and bulk treatments, such as different combinations of polishing and annealing, could yield valuable information on the ideal sample preparation technique and should be a priority of future studies on the IMS with current.

Acknowledgements

Doing science is only possible through teamwork. This goes beyond the mere sharing of scientific understanding and technical know-how of how to do research, but also includes the social endeavor that science represents. This is especially true for the wonderful but challenging experience of a PhD that filled the last few years of my life. There are many people, who supported me during my PhD journey, both on the technical side as well on the social side, and made it possible for me to write these lines today. In the following, I would like to take a moment and thank some of them in particular.

- **Sebastian Mühlbauer** Lieber Basti, vielen Dank, dass du mich seit meiner Bachelorarbeit in die Neutronenstreuung, Supraleitung, und das Wissenschaftliche Arbeiten einführst. Man könnte meinen, das ist eine lange Zeit und irgendwann sollte man alles verstanden haben, aber auch nach mehr als 7 Jahren, kann ich immer noch viel von dir lernen. Danke, dass du das Vertrauen hattest, mir den Doktor "remote" in Grenoble zu ermöglichen, dass du stets ein offenes Ohr hattest, auch schnell mal *ad hoc* einen Abstract oder Ähnliches korrigierst, und insgesamt immer erreichbar bist, trotz der räumlichen Distanz zwischen Grenoble und München.

- **Robert Cubitt** Dear Bob, thank you for teaching me about superconductivity and neutron scattering, and on how to do do science and fill in a small gap in the map of scientific knowledge. Thank you also for always providing me with a cold cryostat when I arrive at work and being the supervisor who could be sometimes confused as the students private, technical assistant. All this while giving me the freedom to structure my project and working day the way it suits me.

- **The Institut Laue-Langevin and the Heinz Maier-Leibnitz Zentrum** Thank you for providing funding, beamtime, and instrumentation for my PhD project and allowing me to become part of the scientific communities at both institutes.

- **LSS group at the ILL** Thank you for providing a scientific community, where I could discuss science on a daily basis, get help when I'm stuck with some data analysis, or go for lunch runs in the beautiful mountains surrounding the ILL to clear my thoughts.

- **F. Marchal, F. Lapeyre, M. Bonnaud, C. Cocho, S. Turc, Y. Le Goc, A. Elaazzouzi** Thank you for your help with the sample preparation and for your support with the experiments.

- **Alex Backs & Tommy Reimann** Vielen Dank für eure Erklärungen und eure Vorarbeit zum IMS in Nb ohne die mein Projekt so nicht möglich gewesen wäre.

- **TUM/MLZ scientists** Thank you to all the people helping me with the admin things at TUM and MLZ, the organization of tutorials, and for just being there for a quick lunch or coffee break during my visits in Munich. Special shout out to Michał, Johanna, Laura, Lukas, Julian, Peter and many more for being a fun crew at several conferences all around the world.

- **Café 326 and the ILL student community** In random order and ~~probably~~ definitely incomplete: Erik, Sam, Martha, Moritz, Peter, Chakib, Kamaldeep, Tong, Wenke, Beatrice, Anna, Jason, Marta,... Thank you for the nice time at the ILL and Grenoble. It fills me with joy to look back at all the good times we shared over the daily lunch and coffee breaks, but also the time outside of the ILL exploring the bars and the surroundings of Grenoble. Thank you for your friendship and for your support during the last few years!

- **Studienkollegen München** In beliebiger Reihenfolge: Valentin, Martin, Florian, Stefan, Leon, Phillip,... Danke für die gemeinsame Zeit während des Studiums und eure Freundschaft darüber hinaus. Ich freue mich immer euch bei meinen Besuchen in München zu sehen, oder wenn ihr nach Grenoble zu Besuch kommt. Vielen Dank auch für die ein oder andere Couch, deren Bequemlichkeit ich bei meinen Besuchen in München testen und bestätigen konnte! Besonderen Dank an Florian, dafür dass du Teile meiner Arbeit Korrektur gelesen hast.

- **Les gentils grelous, qui sont bien plus que de simples grelous.** Hugo, Pierre, Noelie, Guillaume, Fiona, Robin, Eymeric, Mathias, et beaucoup plus. Merci pour toutes les activités sportives, mais aussi pour les fêtes, les sorties au cinéma et les beaux moments et conversations autour d'un verre ou d'un bon repas.

- **Meine Familie** Liebe Mama, lieber Papa sowie meine lieben fünf Geschwister mit Partnern und Kindern: ganz herzlichen Dank euch allen, dass ich auf euch zählen kann. Danke, dass ihr mir sowohl finanziell als auch emotional immer unterstützend zur Seite stand und ein offenes Ohr für mich hattet auf meinem bisherigen Lebensweg, der mich zu dem gemacht hat, der ich heute bin.

- **Elodie** Le meilleur pour la fin: Chère Elodie, merci d'être la pour moi, de me soutenir, de me faire rire, de me comprendre et de me supporter comme je suis, avec tous mes atouts et surtout mes défauts. J'ai bien hâte de voir ce que l'avenir nous réserve. Je t'aime!

List of Publications

- **Pushing the limits of accessible length scales via a modified Porod analysis in small-angle neutron scattering on ordered systems**
  X. S. Brems, S. Mühlbauer, R. Cubitt
  Journal of Applied Crystallography, 57(5): 1358–1372, 2024

- **Local reorganisation of the intermediate mixed state in niobium below the critical depinning current**
  X. S. Brems, S. Mühlbauer, R. Cubitt
  Superconductor Science and Technology, 38(2): 025004 (15pp), 2025

- **AC susceptibility and transport measurements of the vortex matter in Nb**
  X. S. Brems, S. Mühlbauer, R. Cubitt
  in preparation

The following publication has been published during the duration of the PhD project. However, the results have been obtained during the preceding Master project, which has been the basis of this PhD project.

- **Current-induced self-organisation of mixed superconducting states**
  X. S. Brems, S. Mühlbauer, W. Y. Córdoba-Camacho, A. A. Shanenko, A. Vagov, J. A. Aguir, R. Cubitt
  Superconductor Science and Technology, 35(3): 035003 (15pp), 2022

A Appendix

A.1 Data Reduction from Raw Data and Phase Determination of the AC Susceptibility and Transport Measurement Data

The raw data of the AC susceptibility setup consists of timestamped data of the different parameters (sample voltage, sample current, AC susceptometer voltage, etc.). An example of this is depicted in figure A.1 showing the recorded values of the sample current, the sample voltage, the voltage of the Lock-In amplifier in the X channel and the Y channel, the sample temperature, and the magnetic field. To extract the reduced data from the raw data, in this case I-V-curves measured in different magnetic fields, the data for each parameter step (here current step) is averaged over the duration of the parameter step using a Python script (here $\Delta t = 12$ s) to yield the mean value and its standard deviation during a parameter step (see figure A.2). The Python script splits the raw data into individual files corresponding to a current scan, temperature scan, or magnetic field scan. Figure A.3 depicts the extracted sample voltage along the extracted values of the sample temperature and the two channels of the dual-phase lock-in amplifier as a function of sample current. The sample voltage showed a slight, slow drift voltage of < 1 μV that showed no regular time dependence. To counteract this, the I-V curves were shifted along the y-axis to result in a nominal zero voltage at low currents. from the I-V-curves the critical voltage depinning current I_{cV} was extracted using a $3\sigma = 0.35$ μV-voltage criterion, with σ the standard deviation of the zero current voltage. This can be converted to a field-criterion of $E \approx 0.5\mu$V/cm using the distance between the voltage taps $d \approx 8$ mm, which compares well to the commonly used value of $E \approx 1\mu$V/cm [10]. The low noise level and the sharp and consistent rise in χ' allow the use of a 0.1 μV voltage criterion to extract the χ' critical depinning $I_{c\chi'}$.

Phase Determination of the AC Susceptibility Signal

The two voltages X and Y of the dual-phase lock-in amplifier correspond to the two orthogonal voltage contributions given in equation (3.8) at the reference frequency $f_{ref} = \omega_{ref}/2\pi$. The two voltages are, therefore, directly related to the in-phase and out-of-phase components of the magnetic susceptibility χ' and χ'' with respect to the reference frequency of the AC drive field. An additional phase shift Θ caused by parasitic capacities and resistances of the susceptometer itself and other external sources is corrected by adapting the phase of the lock-in amplifier with respect to the reference frequency of the drive coil.

Background / offset voltages $v_{0,x/y}$ of the two voltage channels X and Y have to be subtracted to get the sample contribution to the voltage signal only. Temperature scans in high fields above B_{c2} showed that there is no temperature dependence of X and Y in the scanned temperature range from 3 to 10 K. Analogously, there was no field dependence of X and Y above T_c for magnetic fields from 0 to 400 mT. Therefore, offset voltages $v_{0,x/y}$ were determined just above the transition temperature T_c and subtracted from the lock-in amplifier signals X and Y. The phase shift Θ was determined using a tempera-

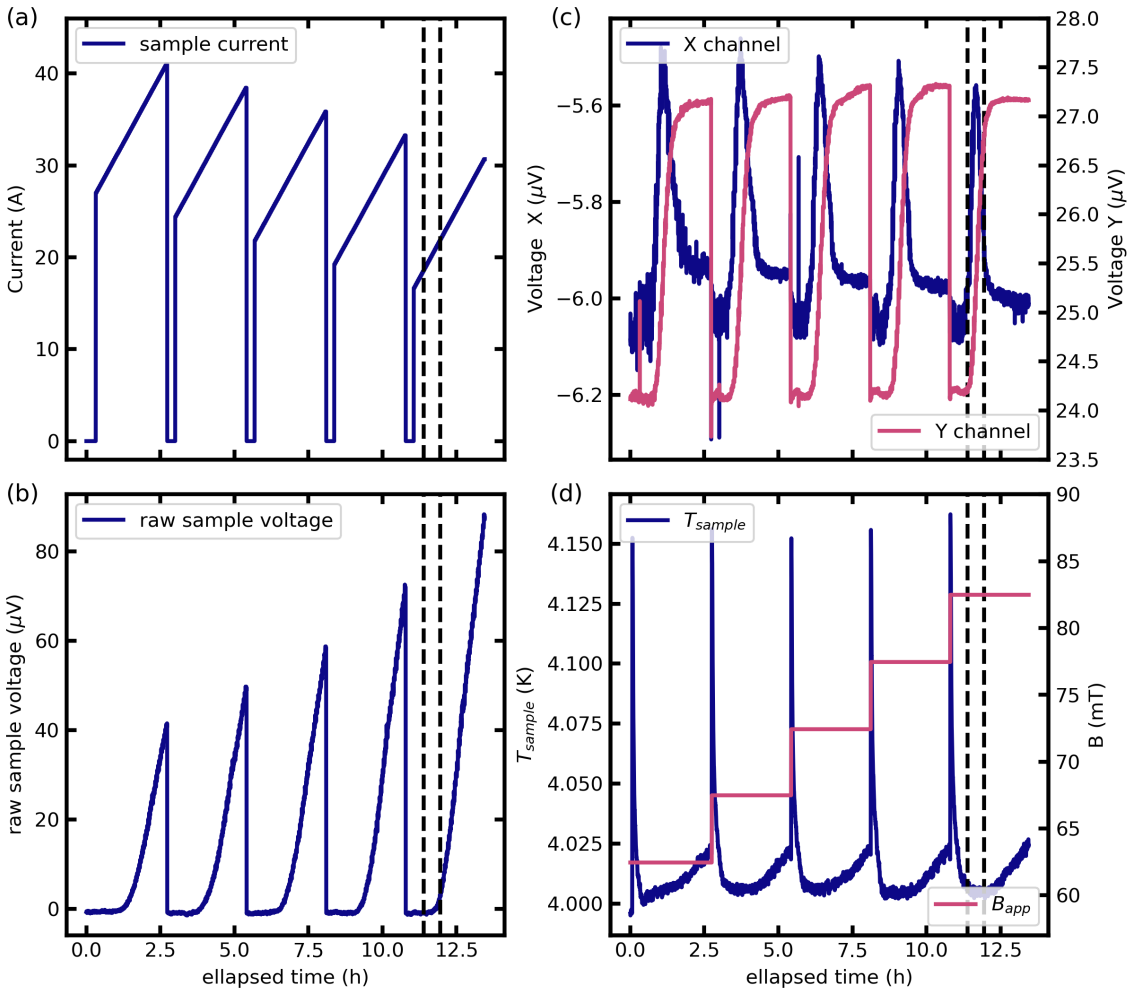

Figure A.1: Raw data of current scans in different applied magnetic fields showing (a) the sample current, (b) the sample voltage, (c) the lock-in amplifier signal, and (d) the sample temperature and the applied magnetic field.

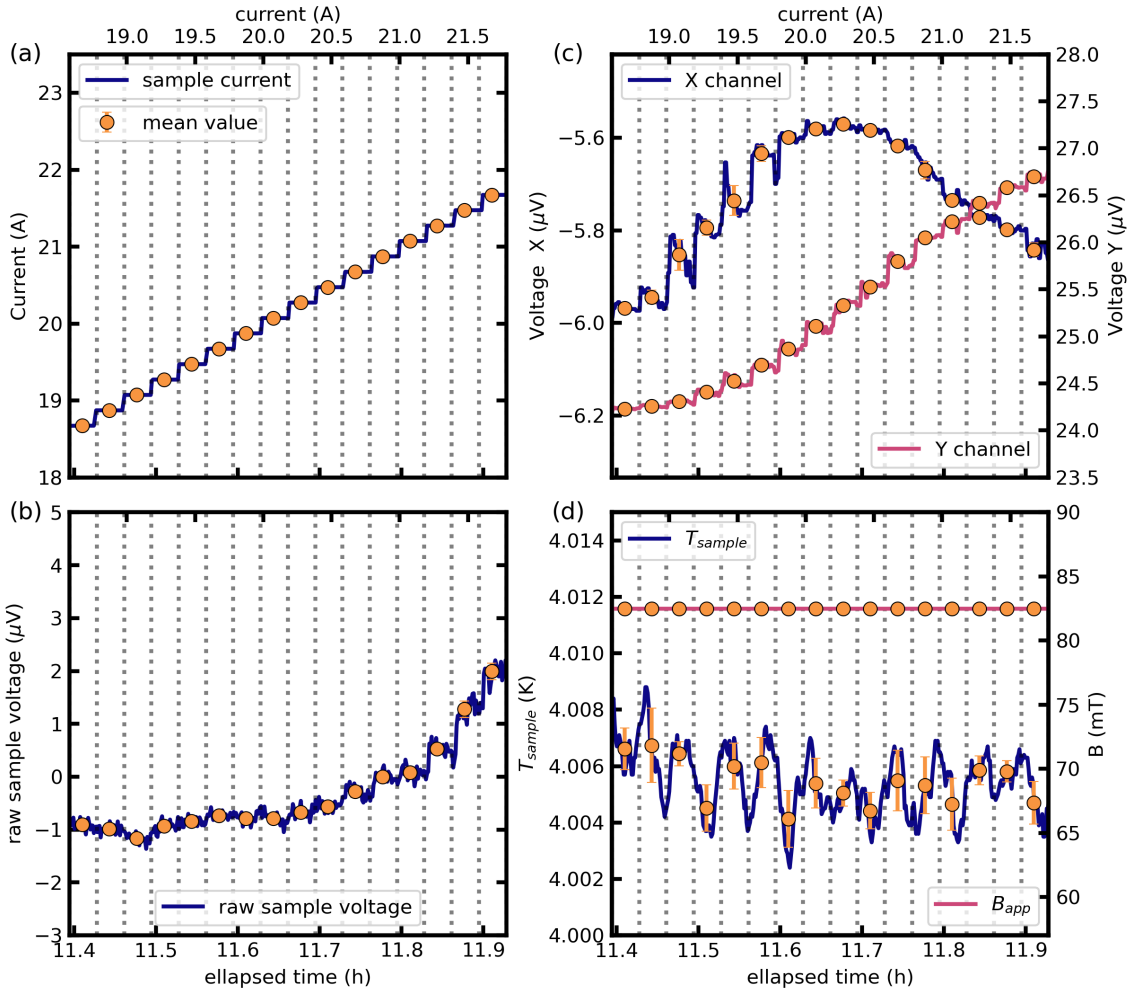

Figure A.2: Zoom in on the raw data and the averaged mean values obtained for each parameter step of the data shown in figure A.1 in between dashed vertical lines showing (a) the sample current, (b) the sample voltage, (c) the lock-in amplifier signal, and (d) the sample temperature and the applied magnetic field. The boundaries of the parameter steps of duration $\Delta t = 120$ s are indicated by dotted vertical lines. The mean values are plotted as orange solid dots.

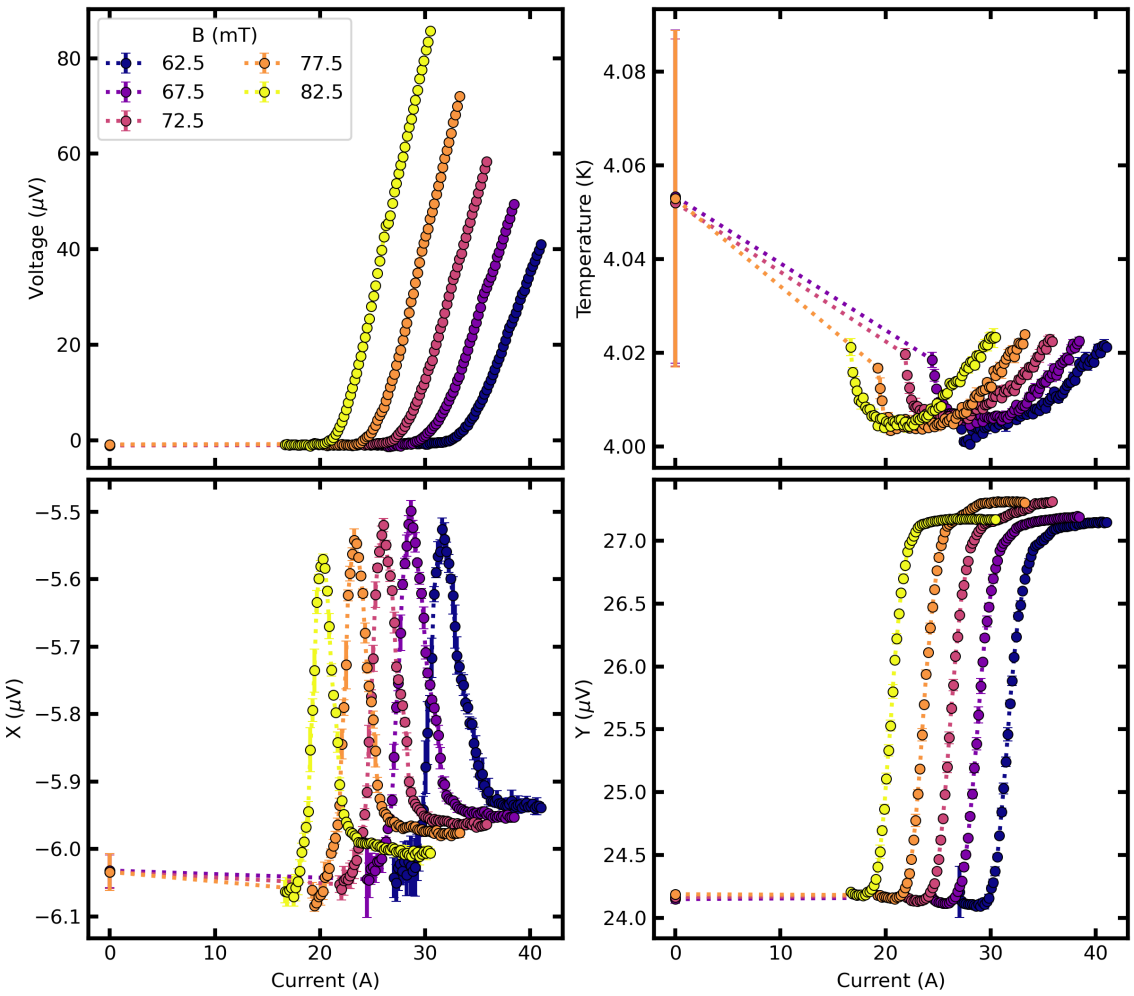

Figure A.3: Examples of reduced data after averaging. (a) the sample voltage, (b) the sample temperature, and (c,d) the X and Y channels of the lock-in amplifier as a function of the sample current in different applied fields. Note that the zero current value is averaged over temperature spike after the field cool and has a larger error bar (especially in the temperature).

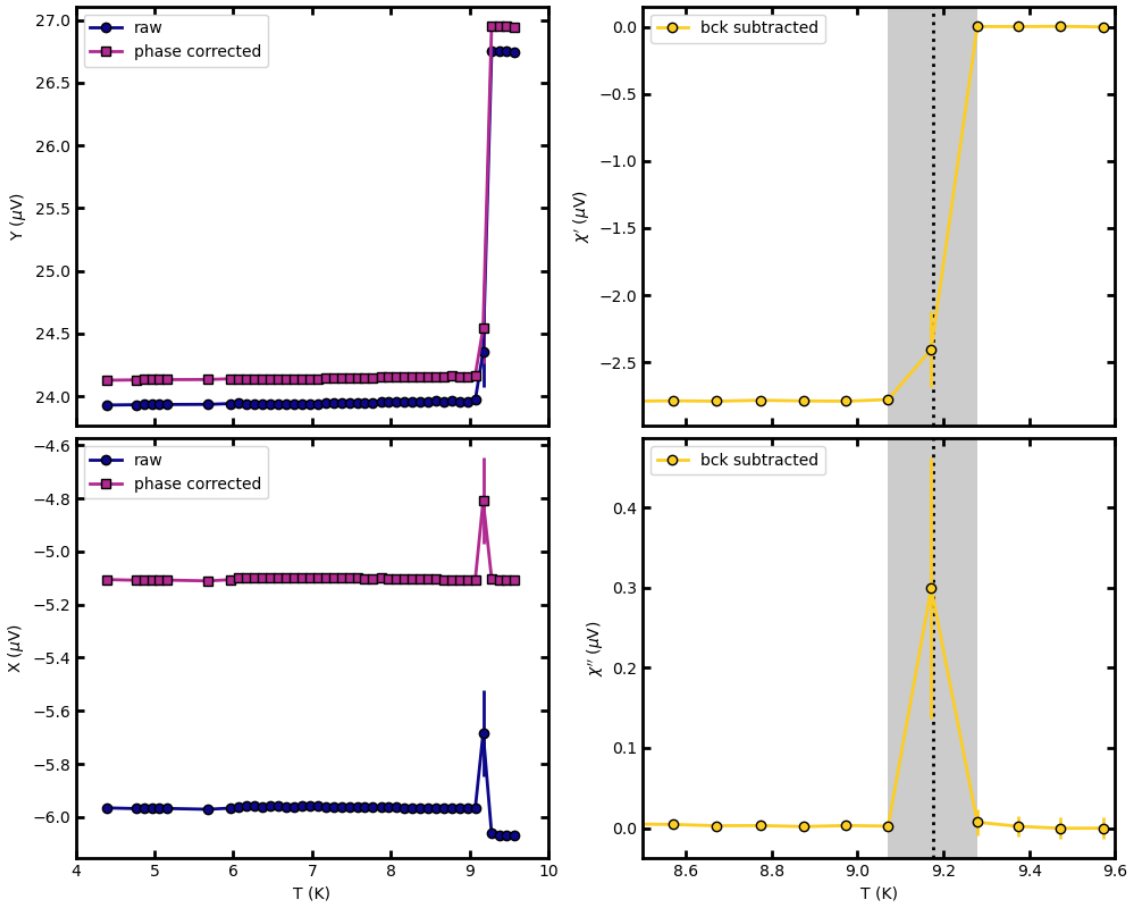

Figure A.4: Phase determination and data reduction to yield the χ' and χ'' from the voltage signal of the lock-in amplifier. Shown is the raw reduced data after averaging over the timestamped data of the two voltage channels along the phase corrected voltage values before background subtraction (first column). The second column depicts the background subtracted values which correspond to χ' and χ''.

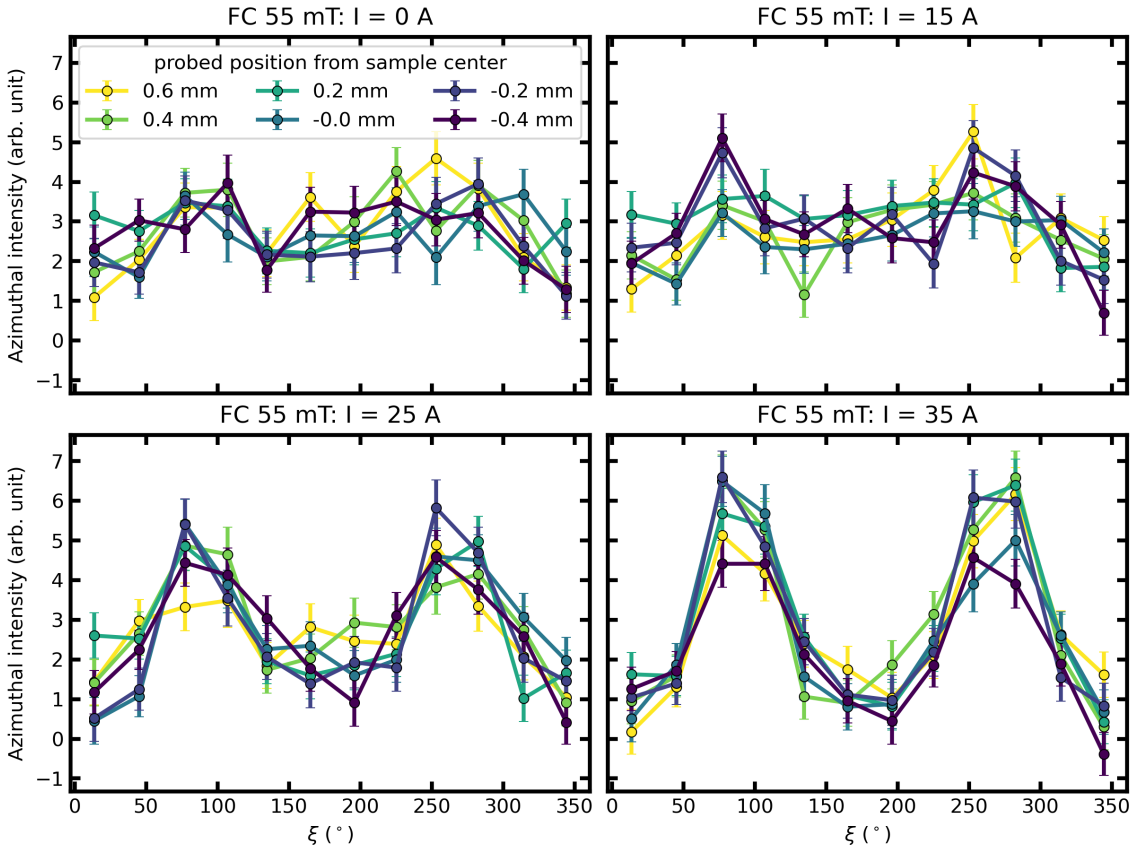

Figure A.5: Height dependence of the azimuthal intensity extracted from SANS patterns measured at six different positions in height with a reduced sample aperture at four different currents.

ture scan in zero field, where any additional resistive processes due to the movement of vortices in the superconducting state are negligible. Therefore, the resistive signal after phase adaption and background subtraction has to be adapted to be zero for $T < T_c$. The approximate phase shift was set at the beginning of the measurement campaign and then determined accurately in post-processing from the zero field temperature scan. All measurements were performed with a fixed phase shift and then adapted using the correct phase from the zero field temperature scan. Both the offset voltages and the phase shift showed slight variations depending on the exact position of the sample installed on the AC susceptometer. Therefore, these values had to be extracted every time the sample was re-positioned. An example of the data reduction and phase determination procedure is included in figure A.4.

A.2 Height Dependence of A_{IMS}

To investigate the possibility that the stripe structure forms via mixed state "fingers" extending from the sample edges, the sample height was scanned in the direction parallel to the movement of vortices using a reduced aperture size of $a_x \times a_y = (5 \times 0.15)$ mm^2 at an intermediate current. Due to the reduced count rate with reduced sample aperture, no

rocking scans were performed, and the azimuthal curves shown in figure A.5 were obtained from 2D SANS data measured at $\omega = \phi = 0$, where the intensity is maximal. The measured position is indicated with respect to the nominal sample center. No significant variation in the current-induced IMS anisotropy was observed across the six different scanned positions. These results suggest that the rearrangement mechanism is uniform across the sample and independent of its height, ruling out that the stripes are penetrating from the sample edges.

A.3 Extracting Lengths from the Bragg and IMS Intensity in Current Scans

In the following, we focus further on the current dependence of the Bragg peak and IMS intensities while proposing a connection between the mean widths of mixed state domains (d) and Meissner state domains (m) with these intensities. The Bragg peak intensity and IMS intensity have been associated with the volume fraction of mixed state domains [13] and the total interface area between mixed and Meissner state domains as presented in chapter 4, respectively.

In a simplified model, the volume fractions of both domain types, as well as their total interface area, can be directly related to the two lengths, m and d. Assuming that the domain structure over the entire current range can be modeled as alternating stripes of mixed and Meissner state domains, the mixed state volume fraction is straightforwardly expressed as $d/(m+d)$. Since the Bragg peak intensity is proportional to the mixed state volume fraction, it provides direct access to $d/(m+d)$.

The IMS intensity is proportional to the specific surface area, which corresponds to the total interface area between the mixed and Meissner state domains. In a simplified approach, assuming that the alternating stripe morphology is maintained across the entire current range, the extracted specific surface area becomes inversely proportional to the repetition length $m+d$ (see chapter 4).

Thus, under these assumptions, the integrated Bragg peak intensity I_{Bragg} and IMS intensity I_{IMS} at a given field, as functions of current, can be expressed as follows:

$$I_{\mathrm{Bragg}}(I) = c_{\mathrm{Bragg}} \frac{d(I)}{m(I)+d(I)} \tag{A.1}$$

$$I_{\mathrm{IMS}}(I) = c_{\mathrm{IMS}} \frac{1}{m(I)+d(I)}, \tag{A.2}$$

where c_{Bragg} and c_{IMS} are proportionality factors, which can be assumed to only depend on B_{app} and other constant factors. We can also extract the zero-current normalized intensities $\alpha(I)$ and $\beta(I)$

$$\alpha(I) = \frac{I_{\mathrm{Bragg}}(I)}{I_{\mathrm{Bragg}}(0A)} \tag{A.3}$$

$$\beta(I) = \frac{I_{\mathrm{IMS}}(I)}{I_{\mathrm{IMS}}(0A)}, \tag{A.4}$$

which eliminates the proportionality factors.

Combining equations A.1, A.2, A.3, and A.4 allows to extract the relative change of $d(I)$ relative to $d(0A)$ according to

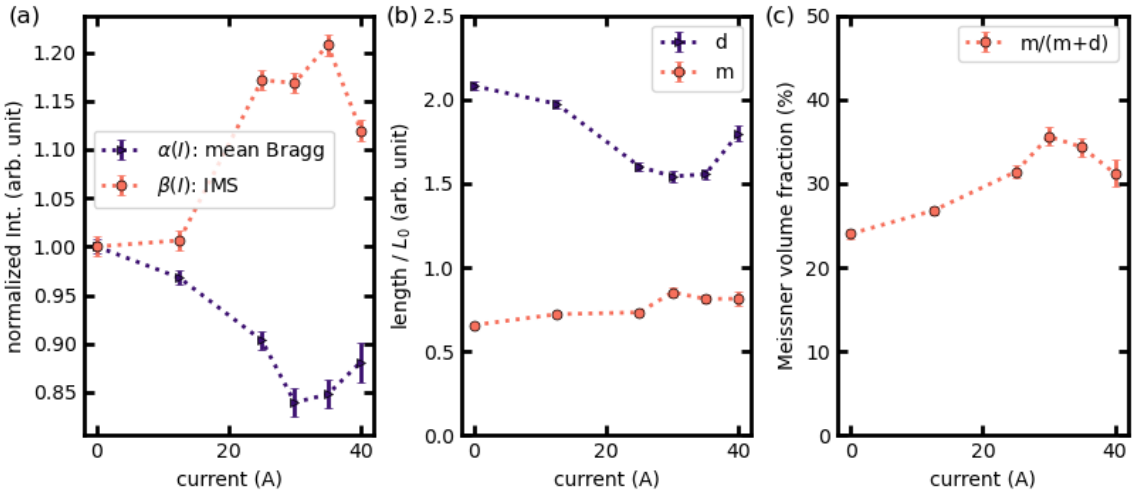

Figure A.6: Extraction of m and d from the Bragg peak and IMS intensity. (a) Normalized Bragg and IMS intensities $\alpha(I)$ and $\beta(I)$. (b) $m(I)$ and $d(I)$ in terms of L_0. (c) The volume fraction of the Meissner state calculated from $m(I)$ and $d(I)$.

$$d(I) = \frac{\alpha(I)}{\beta(I)} d(0A). \tag{A.5}$$

Similarly we can rewrite $m(I)$

$$m(I) = \frac{1}{\beta(I)} \left[m(0A) + (1 - \alpha(I))\, d(0A) \right]. \tag{A.6}$$

The above equation relates $m(I)$ to both $m(0A)$ and $d(0A)$, which are changing as a function of field, but doesn't allow to extract the relative change of $m(I)$ to $m(0A)$. However, it connects $m(0A)$ and $d(0A)$ to a single parameter L_0 using the proposed model of $m(b)$ and $d(b)$ presented in section 4.4. This simple phenomenological model qualitatively describes the field dependence for d and m and fits well the extracted length scale of the repetition length $m + d$ from the modified Porod analysis (see figure 4.6) The fitted value in section 4.4 was $L_0 = (2.9 \pm 0.1)\ \mu$m but is a sample-specific value as the width of the domains depends on the width of the sample. Due to the limited range of fields, L_0 could not be accurately determined for Nb-2, which is why we will express all values in multiples of L_0. Using the above model to express $m(0A)$ and $d(0A)$ we can extract the current and field dependence of m and d in multiples of L_0

$$d(I, b) = \frac{\alpha(I)}{\beta(I)} \frac{1}{1 - b} \frac{L_0}{2} \tag{A.7}$$

$$m(I, b) = \frac{1}{\beta(I)} \left(\frac{1}{b} + (1 - \alpha(I)) \frac{1}{1 - b} \right) \frac{L_0}{2} \tag{A.8}$$

The results are shown in figure A.6 on the example of the current scan of Nb-2 in $B_{app} = 55$ mT and $T = 4$ K. Figure A.6 (a) depicts the normalized intensities $\alpha(I)$ and $\beta(I)$ showing the same decrease and increase as the mean Bragg peak and IMS intensity, respectively, as expected (see figures 6.6 (a,b)). The current-dependence of m and d is included in figure A.6 (b) and calculated from the normalized intensities according to equations A.7 and A.8 as a function of L_0. We observe a decrease of d with increasing current, while m shows a slight increase with increasing current. From the current dependence of m and d, we can calculate the Meissner volume fraction as $m/(m+d)$ shown in figure A.6 (c). This reveals a gradual increase in the Meissner volume with increasing current. The Meissner volume fraction is proportional to the diamagnetic moment, which corresponds to the negative magnetization. In FC magnetization measurements conducted on samples cut from the same single crystal [87], the magnetization underwent a macroscopic flux freezing transition, where the magnetization slightly decreases close to T_c but stays constant for temperatures $T < T_f$ with T_f the flux freezing temperature. The formation of the IMS is unaffected by this macroscopic flux-freezing. However, the flux freezing preserves a state with a higher macroscopic flux down to lower temperatures [87, 53]. The observed increase in the Meissner volume fraction with current suggests that the current is expelling trapped flux, driving the system closer to its equilibrium state, which would have been achieved in the absence of pinning.

We would like to emphasize that the analysis approach presented here provides only an estimate of d and m. A more rigorous method to extract the repetition length $m+d$ would require obtaining the correct specific surface area from the low-q power-law scattering, as outlined in the modified Porod analysis presented in section 4. Here, where the current induces the stripe structure, the specific surface area derived from the Porod law would also need to be corrected for the current-dependent anisotropy observed in the azimuthally averaged scattering data. While we are able to quantitatively track the anisotropy A_{IMS} as a function of current, the limited azimuthal resolution near the direct beam makes it difficult to accurately determine the correction factor required to extract the true specific surface area in the case of the IMS. Moreover, the evolving structure of the IMS with current further complicates the extraction of a meaningful repetition length from the specific surface area. Nevertheless, the approach described above, combined with the assumption that the domain structure can be modeled as parallel stripes of mixed state and Meissner state domains over the full range of probed current, enables us to estimate $d(I)$ and $m(I)$. Furthermore, the interpretation that the current drives the system toward its equilibrium state aligns with one of the key findings of our previous study, which demonstrated that the current induces the stripe structure independent of the order of cooling or field application [17]. This highlights the ability of the current to overcome metastable states.

A.4 Field Dependence of A_{IMS}

We examine the trend of A_{IMS} in the depinned state as a function of increasing field. Comparing measurements on Nb-1 in 40 mT, 50 mT, and 62 mT, the saturation value of A_{IMS} in the depinned state tends to increase with field (see figure 6.7). This suggests that the current-induced IMS stripe structure becomes more aligned at higher values of

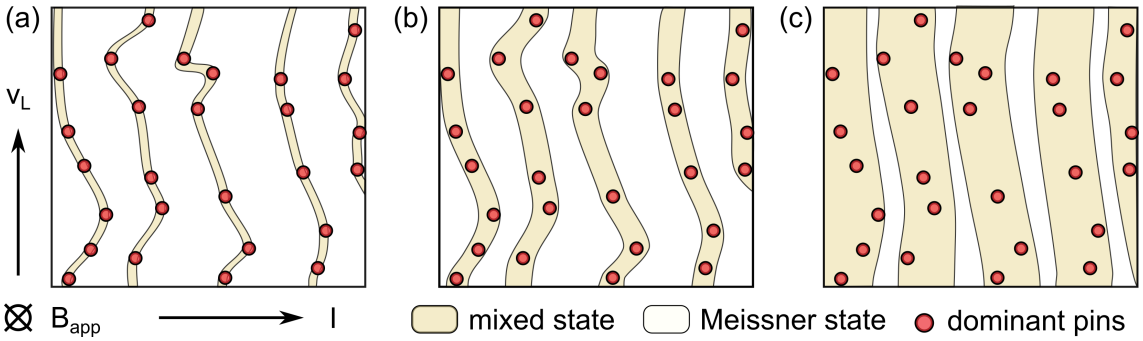

Figure A.7: Schematic of the field dependence of the stripe structure in the depinned state for $I > I_{cV}$ for three mixed state filling fractions. For increasing mixed state filling fractions, the interface is straighter between the mixed state and Meissner state domains, and the low-q anisotropy and with it A_{IMS} is larger in the depinned state.

B_{app}. A possible explanation for this could be the field-dependent size of the mixed state domains and its impact on the straightness of the stripe structure in the depinned state, which will be discussed in the following.

The influence of d on the straightness of the domains is schematically illustrated in figure A.7, which shows the depinned VL as a function of three different values of d using the same pinning landscape depicted in the schematics of figure 6.8. The size of the mixed state domains, d, increases with increasing field. While the previous section demonstrated that d decreases in the depinned state for a given field, we can reasonably assume that even in the depinned state, d still increases with increasing field. At lower values of B_{app}, the individual stripes are narrower, whereas the stripe width expands as B_{app} increases. Regardless of the width of the mixed state domains, the depinned vortices can be visualized as following the pinning centers, similar to stepping stones in a river, as proposed in a recent study [116]. As a result, a series of pinning sites can fit into a thick, straight stripe at higher fields, while at lower fields, the same pinning sites can only be connected by a winding path of mixed state domains. In the SANS pattern, this leads to an increase in anisotropy with increasing field due to the straighter mixed state domains and consequently higher values of A_{IMS}.

To use an analogy, the influence of d on the straightness of the mixed state domains can be visualized as connecting dots at fixed positions using pens of different line widths, with the constraint of minimizing the total path length. The width of the pen determines the level of detail that can be resolved. A thinner pen allows to capture finer details. In contrast, a thicker pen results in a straighter, less detailed path, smoothing out any potential curves or deviations.

B List of Figures

C List of Tables

References

[1] H. K. Onnes, "Further experiments with liquid helium c. on the change of electric resistance of pure metals at very low temperatures etc. iv. the resistance of pure mercury at helium temperatures," *Commun. Phys. Lab. Univ. Leiden*, vol. 120b, 1911.

[2] W. Meissner and R. Ochsenfeld, "Ein neuer Effekt bei Eintritt der Supraleitfähigkeit," *Naturwissenschaften*, vol. 21, pp. 787–788, Nov. 1933.

[3] J. Bardeen, L. N. Cooper, and J. R. Schrieffer, "Theory of superconductivity," *Phys. Rev.*, vol. 108, pp. 1175–1204, Dec 1957.

[4] V. Ginzburg and L. Landau, "On the theory of superconductivity," *Zh. Eksperiment. Teoret. Fiz.*, vol. 20, p. 1064, 1950.

[5] J. G. Bednorz and K. A. Müller, "Possible high T_c superconductivity in the Ba-La-Cu-O system," *Zeitschrift für Physik B Condensed Matter*, vol. 64, pp. 189–193, June 1986.

[6] M. K. Wu, J. R. Ashburn, C. J. Torng, P. H. Hor, R. L. Meng, L. Gao, Z. J. Huang, Y. Q. Wang, and C. W. Chu, "Superconductivity at 93 K in a new mixed-phase Y-Ba-Cu-O compound system at ambient pressure," *Phys. Rev. Lett.*, vol. 58, pp. 908–910, Mar 1987.

[7] H. Hosono, A. Yamamoto, H. Hiramatsu, and Y. Ma, "Recent advances in iron-based superconductors toward applications," *Mater. Today*, vol. 21, no. 3, pp. 278–302, 2018.

[8] M. Sato and Y. Ando, "Topological superconductors: a review," *Rep. Prog. Phys.*, vol. 80, p. 076501, may 2017.

[9] E. H. Brandt and M. P. Das, "Attractive vortex interaction and the intermediate-mixed state of superconductors," *J. Supercond. Novel Magn.*, vol. 24, pp. 57–67, Jan. 2011.

[10] W.-K. Kwok, U. Welp, A. Glatz, A. E. Koshelev, K. J. Kihlstrom, and G. W. Crabtree, "Vortices in high-performance high-temperature superconductors," *Rep. Prog. Phys.*, vol. 79, p. 116501, sep 2016.

[11] N. V. Sarma, "Transition from the flux lattice to the intermediate state structures in a lead-indium alloy," *The Philosophical Magazine: A Journal of Theoretical Experimental and Applied Physics*, vol. 18, no. 151, pp. 171–176, 1968.

[12] U. Krägeloh, "Der Zwischenzustand bei Supraleitern zweiter Art," *physica status solidi (b)*, vol. 42, no. 2, pp. 559–576, 1970.

[13] D. K. Christen, F. Tasset, S. Spooner, and H. A. Mook, "Study of the intermediate mixed state of niobium by small-angle neutron scattering," *Phys. Rev. B*, vol. 15, pp. 4506–4509, 5 1977.

[14] S. Mühlbauer, C. Pfleiderer, P. Böni, M. Laver, E. M. Forgan, D. Fort, U. Keiderling, and G. Behr, "Morphology of the superconducting vortex lattice in ultrapure niobium," *Phys. Rev. Lett.*, vol. 102, p. 136408, Apr 2009.

[15] T. Reimann, S. Mühlbauer, M. Schulz, B. Betz, A. Kaestner, V. Pipich, P. Böni, and C. Grünzweig, "Visualizing the morphology of vortex lattice domains in a bulk type-II superconductor," *Nat. Commun.*, vol. 6, p. 8813, Nov. 2015.

[16] A. Backs, M. Schulz, V. Pipich, M. Kleinhans, P. Böni, and S. Mühlbauer, "Universal behavior of the intermediate mixed state domain formation in superconducting niobium," *Phys. Rev. B*, vol. 100, p. 064503, Aug 2019.

[17] X. S. Brems, S. Mühlbauer, W. Y. Córdoba-Camacho, A. A. Shanenko, A. Vagov, J. A. Aguiar, and R. Cubitt, "Current-induced self-organisation of mixed superconducting states," *Supercond. Sci. Technol.*, vol. 35, p. 035003, jan 2022.

[18] X. S. Brems, "Current-induced self-organisation of mixed superconducting states," Master Thesis, Technische Universität München, 07 2021.

[19] C. A. Reynolds, B. Serin, W. H. Wright, and L. B. Nesbitt, "Superconductivity of isotopes of mercury," *Phys. Rev.*, vol. 78, pp. 487–487, May 1950.

[20] E. Maxwell, "Superconductivity of Sn^{124}," *Phys. Rev.*, vol. 79, pp. 173–173, Jul 1950.

[21] C. C. Tsuei and J. R. Kirtley, "Pairing symmetry in cuprate superconductors," *Rev. Mod. Phys.*, vol. 72, pp. 969–1016, Oct 2000.

[22] M. Yethiraj, H. A. Mook, G. D. Wignall, R. Cubitt, E. M. Forgan, S. L. Lee, D. M. Paul, and T. Armstrong, "Anisotropic vortex lattice in $YBa_2Cu_3O_7$," *Phys. Rev. Lett.*, vol. 71, pp. 3019–3022, Nov 1993.

[23] Y. Kamihara, H. Hiramatsu, M. Hirano, R. Kawamura, H. Yanagi, T. Kamiya, and H. Hosono, "Iron-based layered superconductor: LaOFeP," *J. Am. Chem. Soc.*, vol. 128, pp. 10012–10013, Aug. 2006.

[24] Y. Kamihara, T. Watanabe, M. Hirano, and H. Hosono, "Iron-based layered superconductor $La[O_{1-x}F_x]FeAs$ ($x = 0.05 - 0.12$) with $T_c = 26$ K," *J. Am. Chem. Soc.*, vol. 130, pp. 3296–3297, Mar. 2008.

[25] C. Pfleiderer, "Superconducting phases of f-electron compounds," *Rev. Mod. Phys.*, vol. 81, pp. 1551–1624, Nov 2009.

[26] E. Campillo, R. Riyat, S. Pollard, P. Jefferies, A. T. Holmes, R. Cubitt, J. S. White, J. Gavilano, Z. Huesges, O. Stockert, E. M. Forgan, and E. Blackburn, "Observations of the effect of strong pauli paramagnetism on the vortex lattice in superconducting $CeCu_2Si_2$," *Phys. Rev. B*, vol. 104, p. 184508, Nov 2021.

[27] M. R. Eskildsen, "Vortex lattices in type-II superconductors studied by small-angle neutron scattering," *Frontiers of Physics*, vol. 6, pp. 398–409, Dec. 2011.

[28] K. E. Avers, S. J. Kuhn, A. W. D. Leishman, W. J. Gannon, L. DeBeer-Schmitt, C. D. Dewhurst, D. Honecker, R. Cubitt, W. P. Halperin, and M. R. Eskildsen, "Reversible ordering and disordering of the vortex lattice in UPt_3," *Phys. Rev. B*, 2021.

[29] A. Huxley, P. Rodière, D. M. Paul, N. van Dijk, R. Cubitt, and J. Flouquet, "Realignment of the flux-line lattice by a change in the symmetry of superconductivity in UPt_3," *Nature*, vol. 406, pp. 160–164, July 2000.

[30] O. Gunnarsson, "Superconductivity in fullerides," *Rev. Mod. Phys.*, vol. 69, pp. 575–606, Apr 1997.

[31] C. J. Pickard, I. Errea, and M. I. Eremets, "Superconducting hydrides under pressure," *Annual Review of Condensed Matter Physics*, vol. 11, no. Volume 11, 2020, pp. 57–76, 2020.

[32] A. P. Drozdov, M. I. Eremets, I. A. Troyan, V. Ksenofontov, and S. I. Shylin, "Conventional superconductivity at 203 kelvin at high pressures in the sulfur hydride system," *Nature*, vol. 525, pp. 73–76, Sept. 2015.

[33] N. Dasenbrock-Gammon, E. Snider, R. McBride, H. Pasan, D. Durkee, N. Khalvashi-Sutter, S. Munasinghe, S. E. Dissanayake, K. V. Lawler, A. Salamat, and R. P. Dias, "Evidence of near-ambient superconductivity in a N-doped lutetium hydride," *Nature*, vol. 615, pp. 244–250, Mar. 2023.

[34] N. Dasenbrock-Gammon, E. Snider, R. McBride, H. Pasan, D. Durkee, N. Khalvashi-Sutter, S. Munasinghe, S. E. Dissanayake, K. V. Lawler, A. Salamat, and R. P. Dias, "Retraction note: Evidence of near-ambient superconductivity in a N-doped lutetium hydride," *Nature*, vol. 624, pp. 460–460, Dec. 2023.

[35] K. Chang, "11 scientists found a room-temperature superconductor. now 8 of them want a retraction.." Online, Sept. 2023. Retreived on 25.10.2024.

[36] R. Toft-Petersen, A. B. Abrahamsen, S. Balog, L. Porcar, and M. Laver, "Decomposing the Bragg glass and the peak effect in a type-II superconductor," *Nat. Commun.*, vol. 9, no. 1, p. 901, 2018.

[37] G. W. Crabtree and D. R. Nelson, "Vortex physics in high-temperature superconductors," *Phys. Today*, vol. 50, no. 4, pp. 38–45, 1997.

[38] E. H. Brandt, "The flux-line lattice in superconductors," *Rep. Prog. Phys.*, vol. 58, pp. 1465–1594, nov 1995.

[39] A. Huxley, *Neutron Scattering from Vortex Lattices in Superconductors*, pp. 301–320. Berlin, Heidelberg: Springer Berlin Heidelberg, 2002.

[40] M. Laver and E. M. Forgan, "Magnetic flux lines in type-II superconductors and the 'hairy ball' theorem," *Nat. Commun.*, vol. 1, p. 45, July 2010.

[41] T. Klein, I. Joumard, S. Blanchard, J. Marcus, R. Cubitt, T. Giamarchi, and P. Le Doussal, "A Bragg glass phase in the vortex lattice of a type ii superconductor," *Nature*, vol. 413, pp. 404–406, Sept. 2001.

[42] J.-Y. Ge, V. N. Gladilin, J. Tempere, V. S. Zharinov, J. Van de Vondel, J. T. Devreese, and V. V. Moshchalkov, "Direct visualization of vortex ice in a nanostructured superconductor," *Phys. Rev. B*, vol. 96, p. 134515, Oct 2017.

[43] R. Cubitt, E. M. Forgan, G. Yang, S. L. Lee, D. M. Paul, H. A. Mook, M. Yethiraj, P. H. Kes, T. W. Li, A. A. Menovsky, Z. Tarnawski, and K. Mortensen, "Direct observation of magnetic flux lattice melting and decomposition in the high-T_c superconductor $Bi_2.15Sr_1.95CaCu_2O_{8+x}$," *Nature*, vol. 365, pp. 407–411, Sept. 1993.

[44] V. Moshchalkov, M. Menghini, T. Nishio, Q. H. Chen, A. V. Silhanek, V. H. Dao, L. F. Chibotaru, N. D. Zhigadlo, and J. Karpinski, "Type-1.5 superconductivity," *Phys. Rev. Lett.*, vol. 102, p. 117001, Mar 2009.

[45] E. B. Bogomol'nyi and A. I. Vainshtein, "Stability of strings in gauge abelian theory," *Sov. J. Nucl. Phys. (Engl. Transl.); (United States)*, vol. 23:5, 5 1976.

[46] H. Träuble and U. Essmann, "Die Beobachtung magnetischer Strukturen von Supraleitern zweiter Art," *physica status solidi (b)*, vol. 20, no. 1, pp. 95–111, 1967.

[47] D. K. Christen, H. R. Kerchner, S. T. Sekula, and P. Thorel, "Equilibrium properties of the fluxoid lattice in single-crystal niobium. ii. small-angle neutron-diffraction measurements," *Phys. Rev. B*, vol. 21, pp. 102–117, Jan 1980.

[48] U. Klein, "Microscopic calculations on the vortex state of type II superconductors," *J. Low Temp. Phys.*, vol. 69, pp. 1–37, Oct. 1987.

[49] M. Laver, C. J. Bowell, E. M. Forgan, A. B. Abrahamsen, D. Fort, C. D. Dewhurst, S. Mühlbauer, D. K. Christen, J. Kohlbrecher, R. Cubitt, and S. Ramos, "Structure and degeneracy of vortex lattice domains in pure superconducting niobium: A small-angle neutron scattering study," *Phys. Rev. B*, vol. 79, p. 014518, Jan 2009.

[50] J.-Y. Ge, J. Gutierrez, A. Lyashchenko, V. Filipov, J. Li, and V. V. Moshchalkov, "Direct visualization of vortex pattern transition in ZrB_{12} with Ginzburg-Landau parameter close to the dual point," *Phys. Rev. B*, vol. 90, p. 184511, Nov 2014.

[51] E. Babaev, J. Carlström, and M. Speight, "Type-1.5 superconducting state from an intrinsic proximity effect in two-band superconductors," *Phys. Rev. Lett.*, vol. 105, p. 067003, Aug 2010.

[52] L. Komendová, M. V. Milošević, and F. M. Peeters, "Soft vortex matter in a type-I/type-II superconducting bilayer," *Phys. Rev. B*, vol. 88, p. 094515, Sep 2013.

[53] T. Reimann, M. Schulz, D. F. R. Mildner, M. Bleuel, A. Brûlet, R. P. Harti, G. Benka, A. Bauer, P. Böni, and S. Mühlbauer, "Domain formation in the type-II/1 superconductor niobium: Interplay of pinning, geometry, and attractive vortex-vortex interaction," *Phys. Rev. B*, vol. 96, p. 144506, 10 2017.

[54] A. Backs, A. Al-Falou, A. Vagov, P. Böni, and S. Mühlbauer, "Temperature-driven transition into vortex clusters in low-kappa intertype superconductors," *Phys. Rev. B*, vol. 107, p. 174527, May 2023.

[55] H. R. Kerchner, D. K. Christen, and S. T. Sekula, "Equilibrium properties of the fluxoid lattice in single-crystal niobium. i. magnetization measurements," *Phys. Rev. B*, vol. 21, pp. 86–101, Jan 1980.

[56] S. Wolf, A. Vagov, A. A. Shanenko, V. M. Axt, and J. A. Aguiar, "Vortex matter stabilized by many-body interactions," *Phys. Rev. B*, vol. 96, p. 144515, 10 2017.

[57] A. A. Shanenko, M. V. Milošević, F. M. Peeters, and A. V. Vagov, "Extended Ginzburg-Landau formalism for two-band superconductors," *Phys. Rev. Lett.*, vol. 106, p. 047005, Jan 2011.

[58] A. V. Vagov, A. A. Shanenko, M. V. Milošević, V. M. Axt, and F. M. Peeters, "Extended Ginzburg-Landau formalism: Systematic expansion in small deviation from the critical temperature," *Phys. Rev. B*, vol. 85, p. 014502, Jan 2012.

[59] A. Vagov, A. A. Shanenko, M. V. Milošević, V. M. Axt, V. M. Vinokur, J. A. Aguiar, and F. M. Peeters, "Superconductivity between standard types: Multiband versus single-band materials," *Phys. Rev. B*, vol. 93, p. 174503, May 2016.

[60] V. D. Neverov, A. E. Lukyanov, A. V. Krasavin, A. A. Shanenko, M. D. Croitoru, and A. Vagov, "Microscopic description of intermediate mixed state in superconductors between the first and second types," *Phys. Rev. B*, vol. 110, p. 054502, Aug 2024.

[61] A. Vagov, S. Wolf, M. D. Croitoru, and A. A. Shanenko, "Universal flux patterns and their interchange in superconductors between types I and II," *Communications Physics*, vol. 3, p. 58, Mar. 2020.

[62] U. Kumpf, "Magnetisierungskurven von Supraleitern zweiter Art mit kleinen Ginzburg-Landau-Parametern," *physica status solidi (b)*, vol. 44, no. 2, pp. 829–843, 1971.

[63] D. R. Aston, L. W. Dubeck, and F. Rothwarf, ""intermediate mixed" state of type-II superconductors," *Phys. Rev. B*, vol. 3, pp. 2231–2236, Apr 1971.

[64] S. Ooi, M. Tachiki, T. Konomi, T. Kubo, A. Kikuchi, S. Arisawa, H. Ito, and K. Umemori, "Observation of intermediate mixed state in high-purity cavity-grade Nb by magneto-optical imaging," *Phys. Rev. B*, vol. 104, p. 064504, Aug 2021.

[65] R. Prozorov, M. Zarea, and J. A. Sauls, "Niobium in the clean limit: An intrinsic type-I superconductor," *Phys. Rev. B*, vol. 106, p. L180505, Nov 2022.

[66] L. Landau, "On the theory of superconductivity," *JETP*, vol. 7, p. 371, 1937.

[67] R. N. Goren and M. Tinkham, "Patterns of magnetic flux penetration in superconducting films," *J. Low Temp. Phys.*, vol. 5, pp. 465–494, Oct. 1971.

[68] C. P. Bean, "Magnetization of high-field superconductors," *Rev. Mod. Phys.*, vol. 36, pp. 31–39, Jan 1964.

[69] A. I. Larkin and Y. N. Ovchinnikov, "Pinning in type II superconductors," *J. Low Temp. Phys.*, vol. 34, pp. 409–428, Feb. 1979.

[70] C. Reichhardt and C. J. O. Reichhardt, "Depinning and nonequilibrium dynamic phases of particle assemblies driven over random and ordered substrates: a review," *Rep. Prog. Phys.*, vol. 80, p. 026501, Feb. 2017.

[71] G. Ódor, "Universality classes in nonequilibrium lattice systems," *Rev. Mod. Phys.*, vol. 76, pp. 663–724, Aug 2004.

[72] U. Yaron, P. L. Gammel, D. A. Huse, R. N. Kleiman, C. S. Oglesby, E. Bucher, B. Batlogg, D. J. Bishop, K. Mortensen, and K. N. Clausen, "Structural evidence for a two-step process in the depinning of the superconducting flux-line lattice," *Nature*, vol. 376, pp. 753–755, Aug. 1995.

[73] U. Yaron, P. L. Gammel, D. A. Huse, R. N. Kleiman, C. S. Oglesby, E. Bucher, B. Batlogg, D. J. Bishop, K. Mortensen, K. Clausen, C. A. Bolle, and F. De La Cruz, "Neutron diffraction studies of flowing and pinned magnetic flux lattices in $2H - NbSe_2$," *Phys. Rev. Lett.*, vol. 73, pp. 2748–2751, Nov 1994.

[74] A. Pautrat, C. Goupil, C. Simon, D. Charalambous, E. Forgan, G. Lazard, P. Mathieu, and A. Brûlet, "Distribution of transport current in a type-II superconductor studied by small-angle neutron scattering," *Phys. Rev. Lett.*, vol. 90, p. 087002, Mar. 2003.

[75] R. Cubitt, A. S. Campbell, E. M. Forgan, C. D. Dewhurst, and G. Yang, "Investigation of vortex structures in a current-carrying Nb wire," *Supercond. Sci. Technol.*, vol. 22, p. 034014, 2 2009.

[76] E. M. Forgan, D. Charalambous, P. G. Kealey, P. J. C. King, R. Khasanov, and A. Amato, "Vortex motion in type II superconductors probed by muon spin rotation and SANS," *Physica B*, vol. 326, pp. 342–345, Feb. 2003.

[77] J. R. Hoberg and R. Prozorov, "Current-driven transformations of the intermediate-state patterns in type-I superconductors," *Phys. Rev. B*, vol. 78, p. 104511, Sep 2008.

[78] M. Nikolo, "Superconductivity: A guide to alternating current susceptibility measurements and alternating current susceptometer design," *Am. J. Phys*, vol. 63, no. 1, pp. 57–65, 1995.

[79] C. V. Topping and S. J. Blundell, "A.C. susceptibility as a probe of low-frequency magnetic dynamics," *J. Phys.: Condens. Matter*, vol. 31, p. 013001, nov 2019.

[80] T. Ishida and R. B. Goldfarb, "Fundamental and harmonic susceptibilities of $YBa_2Cu_3O_{7-\delta}$," *Phys. Rev. B*, vol. 41, pp. 8937–8948, May 1990.

[81] M. Nikolo and R. B. Goldfarb, "Flux creep and activation energies at the grain boundaries of Y-Ba-Cu-O superconductors," *Phys. Rev. B*, vol. 39, pp. 6615–6618, Apr. 1989.

[82] T. Matsushita, *Flux Pinning in Superconductors*. Springer Berlin, Heidelberg, 2014.

[83] R. Gross and A. Marx, *Festkörperphysik*. Berlin, Boston: De Gruyter Oldenbourg, 2022.

[84] J. Bardeen and M. J. Stephen, "Theory of the motion of vortices in superconductors," *Phys. Rev.*, vol. 140, pp. A1197–A1207, Nov 1965.

[85] M. Buchacek, Z. L. Xiao, S. Dutta, E. Y. Andrei, P. Raychaudhuri, V. B. Geshkenbein, and G. Blatter, "Experimental test of strong pinning and creep in current-voltage characteristics of type-II superconductors," *Phys. Rev. B*, vol. 100, p. 224502, Dec 2019.

[86] T. Reimann, *Vortex matter beyond SANS*. phdthesis, Technische Universität München, 2017.

[87] A. Backs, *Vortex Matter of the Intertype Superconductor Niobium*. PhD thesis, Technische Universität München, 2021.

[88] D. S. Sivia, *Elementary scattering theory for X-ray and neutron users*. Oxford Univ. Press, 2011.

[89] G. L. Squires, *Introduction to the Theory of Thermal Neutron Scattering*. Cambridge University Press, 3 ed., 2012.

[90] H. Schober, "An introduction to the theory of nuclear neutron scattering in condensed matter," *J. Neutron Res.*, vol. 17, pp. 109–357, 2014.

[91] H. Furukawa, "Dynamics-scaling theory for phase-separating unmixing mixtures: Growth rates of droplets and scaling properties of autocorrelation functions," *Physica A*, vol. 123, no. 2, pp. 497–515, 1984.

[92] G. Porod, *Small angle X-ray scattering*, pp. 15–51. Academic Press, 1982.

[93] A. Yaouanc, P. Dalmas de Réotier, and E. H. Brandt, "Effect of the vortex core on the magnetic field in hard superconductors," *Phys. Rev. B*, vol. 55, pp. 11107–11110, May 1997.

[94] C. D. Dewhurst, I. Grillo, D. Honecker, M. Bonnaud, M. Jacques, C. Amrouni, A. Perillo-Marcone, G. Manzin, and R. Cubitt, "The small-angle neutron scattering instrument D33 at the Institut Laue–Langevin," *J. Appl. Crystallogr.*, vol. 49, no. 1, pp. 1–14, 2016.

[95] S. V. Grigoriev, A. V. Syromyatnikov, A. P. Chumakov, N. A. Grigoryeva, K. S. Napolskii, I. V. Roslyakov, A. A. Eliseev, A. V. Petukhov, and H. Eckerlebe, "Nanostructures: Scattering beyond the Born approximation," *Phys. Rev. B*, vol. 81, p. 125405, Mar 2010.

[96] T. Adams, S. Mühlbauer, C. Pfleiderer, F. Jonietz, A. Bauer, A. Neubauer, R. Georgii, P. Böni, U. Keiderling, K. Everschor, M. Garst, and A. Rosch, "Long-range crystalline nature of the skyrmion lattice in MnSi," *Phys. Rev. Lett.*, vol. 107, p. 217206, Nov 2011.

[97] S. Mühlbauer, B. Binz, F. Jonietz, C. Pfleiderer, A. Rosch, A. Neubauer, R. Georgii, and P. Böni, "Skyrmion lattice in a chiral magnet," *Science*, vol. 323, p. 915, Feb. 2009.

[98] E. Campillo, M. Bartkowiak, O. Prokhnenko, P. Smeibidl, E. M. Forgan, and E. Blackburn, "Analysis of time-of-flight small-angle neutron scattering data on mesoscopic crystals such as magnetic vortex lattices," *J. Appl. Crystallogr.*, vol. 55, no. 5, pp. 1314–1323, 2022.

[99] R. Cubitt, E. Forgan, D. Paul, S. Lee, J. Abell, H. Mook, and P. Timmins, "Neutron diffraction by the flux lattice in high-T_c superconductors," *Physica B*, vol. 180-181, pp. 377 – 379, 1992.

[100] X. S. Brems, S. Mühlbauer, and R. Cubitt, "Pushing the limits of accessible length scales via a modified Porod analysis in small-angle neutron scattering on ordered systems," *J. Appl. Crystallogr.*, vol. 57, pp. 1358–1372, Aug. 2024.

[101] P. Scherrer *et al.*, "Nachrichten von der Gesellschaft der Wissenschaften zu Göttingen," *Mathematisch-Physikalische Klasse*, vol. 2, pp. 98–100, 1918.

[102] J. Felber, R. Gähler, R. Golub, and K. Prechtel, "Coherence volumes and neutron scattering," *Physica B*, vol. 252, no. 1, pp. 34–43, 1998.

[103] T. F. Stromberg, *The superconducting properties of high purity niobium.* PhD thesis, Iowa State University, 1965.

[104] A. Aharoni, "Demagnetizing factors for rectangular ferromagnetic prisms," *J. Appl. Phys.*, vol. 83, pp. 3432–3434, 03 1998.

[105] X. Brems, R. Cubitt, and S. Mühlbauer, "Stop-and-go kinetic neutron scattering of current-driven vortex clusters." 10.5291/ILL-DATA.5-42-579, 2023.

[106] C. M. Jeffries, J. Ilavsky, A. Martel, S. Hinrichs, A. Meyer, J. S. Pedersen, A. V. Sokolova, and D. I. Svergun, "Small-angle x-ray and neutron scattering," *Nature Reviews Methods Primers*, vol. 1, p. 70, Oct. 2021.

[107] Y. B. Melnichenko and G. D. Wignall, "Small-angle neutron scattering in materials science: Recent practical applications," *J. Appl. Phys.*, vol. 102, p. 021101, 07 2007.

[108] S. Mühlbauer, D. Honecker, E. A. Périgo, F. Bergner, S. Disch, A. Heinemann, S. Erokhin, D. Berkov, C. Leighton, M. R. Eskildsen, and A. Michels, "Magnetic small-angle neutron scattering," *Rev. Mod. Phys.*, vol. 91, p. 015004, Mar 2019.

[109] L. A. Feigin and D. I. Svergun, *Structure Analysis by Small-Angle X-Ray and Neutron Scattering.* Plenum Press, New York, 1987.

[110] J.-M. Schneider, S. Ciccariello, B. Schönfeld, and G. Kostorz, "The asymptotic leading term of anisotropic small-angle scattering intensities. ii. non-convex particles," *Acta Crystallographica Section A*, vol. 58, no. 3, pp. 221–231, 2002.

[111] S. Ciccariello, J.-M. Schneider, B. Schönfeld, and G. Kostorz, "Generalization of Porod's law of small-angle scattering to anisotropic samples," *Europhys. Lett.*, vol. 50, p. 601, jun 2000.

[112] A. Onuki, "Scattering from interfaces and its finite curvature corrections," *Phys. Rev. A*, vol. 45, pp. R3384–R3386, Mar 1992.

[113] E. H. Brandt and U. Essmann, "The flux-line lattice in type-II superconductors," *physica status solidi (b)*, vol. 144, no. 1, pp. 13–38, 1987.

[114] A. T. Dorsey and R. E. Goldstein, "Shapes of flux domains in the intermediate state of type-I superconductors," *Phys. Rev. B*, vol. 57, pp. 3058–3072, Feb 1998.

[115] D. Garisto, "Superconductivity scandal: the inside story of deception in a rising star's physics lab," *Nature*, Mar. 2024.

[116] W. Wang, R. Díaz-Méndez, M. Wallin, J. Lidmar, and E. Babaev, "Pinning effects in a two-dimensional cluster glass," *Phys. Rev. B*, vol. 104, p. 144206, Oct 2021.

[117] A. Czarnecki, "Current distribution in an infinite plate," *Can. J. Phys.*, vol. 92, no. 11, pp. 1297–1300, 2014. a freely accessible version is retrievable from https://arxiv.org/abs/1403.3468.

[118] X. Brems, R. Cubitt, and S. Mühlbauer, "Continuation: Self organisation of the IMS under the application of a current." 10.5291/ILL-DATA.5-31-2911, 2021.

[119] X. Brems, R. Cubitt, and S. Mühlbauer, "Ultra high resolution sans study of the IMS domain morphology with transport current." 10.5291/ILL-DATA.5-31-2951, 2023.

[120] X. Brems, R. Cubitt, and S. Mühlbauer, "Unveiling the self-organisation mechanism of the intermediate mixed state." 10.5291/ILL-DATA.5-42-573, 2023.

[121] S. Mühlbauer, C. Pfleiderer, P. Böni, E. M. Forgan, E. H. Brandt, A. Wiedenmann, U. Keiderling, and G. Behr, "Time-resolved stroboscopic neutron scattering of vortex lattice dynamics in superconducting niobium," *Phys. Rev. B*, vol. 83, p. 184502, May 2011.

[122] N. Mangan, C. Reichhardt, and C. J. O. Reichhardt, "Reversible to irreversible flow transition in periodically driven vortices," *Phys. Rev. Lett.*, vol. 100, p. 187002, May 2008.

[123] S. Okuma, Y. Tsugawa, and A. Motohashi, "Transition from reversible to irreversible flow: Absorbing and depinning transitions in a sheared-vortex system," *Phys. Rev. B*, vol. 83, p. 012503, Jan 2011.

[124] S. Maegochi, K. Ienaga, and S. Okuma, "Critical behavior of density-driven and shear-driven reversible-irreversible transitions in cyclically sheared vortices," *Sci. Rep.*, vol. 11, p. 19280, Sept. 2021.

[125] S. Maegochi, K. Ienaga, S. Kaneko, and S. Okuma, "Critical behavior near the reversible-irreversible transition in periodically driven vortices under random local shear," *Sci. Rep.*, vol. 9, p. 16447, Nov. 2019.

[126] C. Reichhardt, I. Regev, K. Dahmen, S. Okuma, and C. J. O. Reichhardt, "Reversible to irreversible transitions in periodic driven many-body systems and future directions for classical and quantum systems," *Phys. Rev. Res.*, vol. 5, p. 021001, May 2023.

[127] C. Reichhardt and C. J. O. Reichhardt, "Jamming, fragility and pinning phenomena in superconducting vortex systems," *Sci. Rep.*, vol. 10, p. 11625, July 2020.

[128] S. Maegochi, K. Ienaga, and S. Okuma, "Moving smectic phase and transverse mode locking in driven vortex matter," *Phys. Rev. Res.*, vol. 4, p. 033085, Jul 2022.